Soft and stretchable sensors for soft data gloves

by

Yiqi Zhang

A thesis
presented to the University of Waterloo
in fulfillment of the
thesis requirement for the degree of
Doctor of Philosophy
in
Mechanical and Mechatronics Engineering

Waterloo, Ontario, Canada, 2026

© Yiqi Zhang 2026

Examining Committee Membership

The following served on the Examining Committee for this thesis. The decision of the Examining Committee is by majority vote.

External Examiner:	**Dr. Xinyu Liu** Mechanical and Industrial Engineering University of Toronto
Supervisor(s):	**Dr. Carolyn Ren** Mechanical and Mechatronics Engineering University of Waterloo **Dr. John Wen** Mechanical and Mechatronics Engineering University of Waterloo
Internal Member:	**Dr. Michael A. Mayer** Mechanical and Mechatronics Engineering University of Waterloo
Internal Member:	**Dr. Mustafa Yavuz** Mechanical and Mechatronics Engineering University of Waterloo
Internal-External Member:	**Dr. John Yeow** Systems Design Engineering University of Waterloo

Author's Declaration

This thesis consists of material all of which I authored or co-authored: see Statement of Contributions included in the thesis. This is a true copy of the thesis, including any required final revisions, as accepted by my examiners.

I understand that my thesis may be made electronically available to the public.

Statement of Contributions

This thesis incorporates material adapted from the following previously published, co-authored article:

> Y. Zhang, M. Shafiei, J. Z. Wen, Z. Abbasi, and C. L. Ren, "Simultaneous Detection of Pressure and Bending Using a Microwave Sensor With Tag and Reader Structure," *IEEE Transactions on Instrumentation and Measurement*, vol. 72, Art. no. 9511311, pp. 1–11, 2023. https://doi.org/10.1109/TIM.2023.3288253

Section 3.3, including Figures 3.3–3.8 and the accompanying microwave sensor architecture, equivalent-circuit interpretation, simulation trends, and pressure and bending results, incorporates material adapted and expanded from this previously published article. Yiqi Zhang was the first author and led the experimental study, data analysis, and preparation of the publication. Maziar Shafiei and Zahra Abbasi contributed microwave and radio-frequency expertise, technical interpretation, and manuscript review. John Z. Wen and Carolyn L. Ren supervised the research, contributed to the development and interpretation of the study, and reviewed the manuscript. For inclusion in this thesis, Yiqi Zhang reorganized and expanded the material, placed the microwave study within the broader comparison of pressure-sensing approaches, and developed the thesis-specific analysis explaining its role in the subsequent transition to local capacitive readout.

All other material in this thesis was written by Yiqi Zhang. The supervisors and examining committee provided guidance and feedback on the research and thesis revisions.

IEEE reuse notice. In reference to IEEE copyrighted material which is used with permission in this thesis, IEEE does not endorse any of the University of Waterloo's products or services. Internal or personal use of this material is permitted. For information about reprinting or republishing IEEE copyrighted material for advertising or promotional purposes, or creating new collective works for resale or redistribution, see https://www.ieee.org/publications/rights/rights-link.html to obtain a license through RightsLink. If applicable, University Microfilms, ProQuest Library, or the Archives of Canada may supply single copies of this thesis.

Abstract

Data gloves are wearable electronic devices equipped with multiple sensors to quantify hand kinematics and contact forces with high fidelity, enabling applications in rehabilitation monitoring, assistive technology, and human-machine interaction. Despite substantial progress, existing off-the-shelf solutions face critical barriers to clinical translation. Rigid or bulky sensing architectures compromise wearability and user comfort, while standardized one-size-fits-all designs lead to sensor misalignment across diverse hand geometries, degrading measurement accuracy. Furthermore, calibration procedures are often time-consuming and impractical for routine or unsupervised use. These limitations are especially pronounced in ambulatory monitoring scenarios, where devices must function reliably across repeated donning and doffing cycles, and accommodate significant inter-user variability in hand size, shape and biomechanics.

This thesis addresses the key limitations of existing wearable data gloves through three interrelated technical contributions spanning sensing, modeling, and system-level personalization.

First, soft pressure-sensing approaches for palmar contact measurement are developed with a focus on seamless integration into wearable glove platforms. Three sensing modalities are systematically investigated including microwave-resonant sensing, capacitive sensing, and iontronic electric-double-layer sensing. These approaches are comparatively evaluated in terms of sensitivity, mechanical compliance, integration complexity, and suitability for ambulatory use. Based on this analysis, a microstructured soft-stack capacitive architecture is selected for further development. To enable rational design of the microstructure, where performance is governed by nonlinear deformation and evolving contact mechanics, a mechanics-informed finite element modeling framework (FEniCSx/DOLFINx) is established. This is coupled with surrogate modeling to efficiently explore a high-dimensional geometric design space, significantly reducing reliance on empirical, trial-and-error prototyping. Beyond higher sensitivity, this design strategy also enables a more linear response that could help reduce calibration burden by simplifying the mapping between sensor output and applied load.

Second, a flexible, thin pillar-structured capacitive bending sensor is proposed for wide-range joint angle measurement. The sensor operates by transducing bending-induced deformation into capacitance change through controlled volumetric redistribution of air gaps within a microstructured dielectric layer, producing an angle-dominant response that is intrinsically less sensitive to placement variability and therefore requires less calibration than conventional strain-dominant bending sensors, whose outputs vary with fit, pretension,

and placement. An analytical capacitance model, supported by finite element parametric studies, informs the optimization of pillar geometry and material properties. The sensing performance is validated through multi-participant gesture recognition experiments using an instrumented data glove with multiple integrated bending sensors, as well as through knee joint angle tracking benchmarked against a motion capture reference.

Third, an anatomy-to-layout personalization pipeline is proposed to bridge the gap between sensor-level performance and glove-level usability. The pipeline utilizes user-specific hand measurements, obtained via calibrated imaging or manual landmark identification, to generate parametric glove patterns that align sensing elements with anatomically referenced locations. By anchoring sensor placement to joint axes and contact centroids rather than fixed garment coordinates, the approach reduces misalignment arising from donning variability and inter-user anatomical differences, thereby improving measurement consistency across sessions without imposing extensive recalibration.

Collectively, these contributions establish a cohesive design framework for personalized, sensing-integrated data gloves, advancing the state of the art toward practical, reliable, and scalable solutions for on-the-go hand function monitoring.

Acknowledgements

First, I am especially grateful to my supervisor, Dr. Carolyn Ren, for her guidance, encouragement, and constant support over the years. Her insight, patience, and high standards have shaped not only this thesis, but also the way I have grown as a researcher. I am also very thankful to my co-supervisor, Dr. John Wen, for his support and thoughtful feedback throughout this work.

I would also like to thank my thesis committee members, Dr. Michael A. Mayer, Dr. Mustafa Yavuz, and Dr. John Yeow, for their time, expertise, and valuable questions and comments, which helped strengthen this thesis.

I am very grateful to my labmates for their kindness, generosity, and companionship. They made the lab a supportive and enjoyable place to work, and their help, whether in research or in everyday moments, meant a great deal to me.

During the preparation and revision of this thesis, I selectively used ChatGPT for grammar correction, stylistic refinement, and academic rephrasing of selected passages. All research ideas, technical content, analyses, interpretations, and conclusions presented in this thesis are my own. I reviewed and revised all AI-assisted text and take full responsibility for the final content of the thesis.

On a personal note, I want to thank my boyfriend, Steven, for always being there for me throughout this journey. His encouragement kept me grounded during difficult times, and his way of pushing me to think more carefully and pursue what is theoretically sound has influenced me more than he probably knows.

Finally, I would like to thank my parents and my family for their unconditional love, patience, and support. They have been my greatest source of strength through every stage of this journey, and I would not have made it here without them.

Table of Contents

Examining Committee ii

Author's Declaration iii

Statement of Contributions iv

Abstract v

Acknowledgements vii

List of Figures xiii

List of Tables xix

1 Introduction 1

1.1 Background 1

1.2 Motivation 2

1.3 Gaps and challenges 2

1.4 Research objectives 4

1.5 Thesis contributions 7

1.6 Thesis outline 8

2 Methodology **10**
2.1 Motivation for Simulation-Driven Sensor Design 10
2.1.1 Finite element modeling of soft sensors 11
2.1.2 Surrogate modeling and automated design 12
2.1.3 Personalized integration and anatomy-to-layout mapping 12
2.2 Material Characterization for Hyperelastic Modeling 13
2.2.1 Mechanical Testing Setup 13
2.2.2 Constitutive Modeling and Model Selection 13
2.3 Experimental Instrumentation and Evaluation Protocols 19
2.3.1 Readout Electronics 19
2.3.2 Calibration and Characterization Fixtures 19
2.3.3 Data Acquisition and Synchronization 20
2.3.4 Testing Protocols 20
2.3.5 Iontronic Material Selection 21
2.4 Finite Element Workflows 23
2.4.1 Early Exploratory Modeling in COMSOL 23
2.4.2 DolfinX-Based Parameter Sweeps 24
2.4.3 Surrogate Modeling and Optimizer Implementation 28
2.5 Computational Model Verification 29
2.5.1 Mesh Convergence Study 30
2.6 Summary 32

3 Design of Flexible Pressure Sensors **33**
3.1 Pressure Sensing Technologies 34
3.1.1 Rationale for Selecting Capacitive Sensing 36
3.1.2 Role of Microstructure in Sensor Performance 37
3.2 Sensor Design Requirements 39
3.2.1 Operating Range and Sensitivity 39

3.2.2 Linearity and Calibration Burden . . . 39
3.2.3 Mechanical and Integration Constraints . . . 41
3.2.4 Summary of Design Requirements . . . 41
3.3 Microwave Resonator Pressure Sensor . . . 43
3.3.1 Operating Principle . . . 43
3.3.2 Prototype Fabrication and RF Characterization Protocol . . . 44
3.3.3 Tag–Reader Structure and Equivalent Circuit . . . 45
3.3.4 Fabrication and Experimental Results . . . 45
3.3.5 Limitations and Transition to Local-Readout Architectures . . . 46
3.4 Simulation-Driven Design Framework . . . 54
3.4.1 Limitations of Prior Modeling Approaches . . . 54
3.4.2 Framework Overview . . . 55
3.4.3 Nonlinear FEM as the Mechanics Backbone . . . 55
3.4.4 Surrogate Modeling and Array-Level Optimization . . . 57
3.4.5 Mechanism-Specific Transduction Models . . . 58
3.4.6 Range-Tunable Array Optimization . . . 59
3.5 Iontronic EDL Pressure Sensor . . . 64
3.6 Capacitive Pressure Sensor with Solid Silicone Dielectric . . . 75
3.6.1 Design Rationale . . . 75
3.6.2 Sensing Principle and Linearity Constraints . . . 76
3.6.3 Geometry Expansion: Frustums to B-Spline Profiles . . . 77
3.6.4 Active Learning and Surrogate Modeling . . . 81
3.6.5 Range-Tunable Optimization Results . . . 83
3.6.6 Fabrication and Experimental Validation Protocol . . . 88
3.6.7 Interactive Web-Based Design Tool . . . 91

4 Pillar-Structured Capacitive Bending Sensor for Wide-Range Joint-Angle Sensing **94**

4.1 Background and Motivation . . . 94

4.1.1 Bending and joint-angle sensing technologies . . . 95

4.1.2 Design requirements for bending sensing . . . 97

4.2 Sensor Architecture and Fabrication . . . 99

4.2.1 Multilayer structure and design concept . . . 99

4.2.2 Fabrication . . . 100

4.3 Sensing Mechanism and Analytical Model . . . 101

4.3.1 Effective-medium capacitance model . . . 101

4.3.2 Electrode sag correction . . . 101

4.4 FEM-Guided Geometry Optimization . . . 103

4.4.1 Geometry parameter space . . . 103

4.4.2 DolfinX parameter sweep . . . 103

4.4.3 Stability criteria and design window . . . 105

4.5 Experimental Characterization . . . 105

4.5.1 Angle–capacitance calibration . . . 105

4.5.2 Geometric and material parameter validation . . . 105

4.5.3 High-permittivity dielectric strategy . . . 107

4.5.4 Angle-centricity of the pillar/air architecture . . . 107

4.6 Experimental Validation Across Anatomical Sites . . . 107

4.6.1 Anatomical generalisability: large-joint validation at the knee . . . 107

4.6.2 Placement tolerance and cyclic stability under controlled actuation 109

4.7 Summary . . . 110

5 Personalized Data Glove Design **112**

5.1 Existing gloves: focused landscape . . . 113

5.1.1 Assistive soft robotic gloves for grasp support . . . 113

5.1.2 Smart data gloves for sensing and gesture recognition 114
5.1.3 Clinical assessment and rehabilitation monitoring gloves 115
5.2 Glove design goals and constraints for this thesis 117
5.3 Anatomy-to-layout mapping pipeline 119
5.3.1 Hand landmark capture 119
5.3.2 Parametric pattern and sensor layout 121
5.3.3 Gesture-aware skin-strain analysis 121
5.3.4 Sensor placement and trace routing 123
5.3.5 Interactive review of generated glove layouts 125
5.3.6 Manufacturing outputs and assembly notes 125
5.4 Prototype realization and system integration 131
5.4.1 Sensor embedding and mechanical stack-up 131
5.4.2 Electronics integration, readout, and communication 133
5.4.3 System calibration and standardized outputs 133
5.4.4 Validation status of photo-based sensor placement 134
5.5 Glove Prototype Validation 139
5.5.1 Glove configuration and participant study 139
5.5.2 Machine learning pipeline for gesture classification 139
5.5.3 Results 140
5.5.4 Benchmarking against representative data gloves 141
5.6 Summary 141

6 Conclusions **143**
6.1 What the Thesis Establishes 143
6.2 Reflective Assessment 144
6.3 Remaining Open Questions 145

References **146**

List of Figures

1.1 Structural overview of the thesis. A shared methodology backbone provides nonlinear material modeling and FEM; the pressure-sensor chapter develops a range-tunable optimization framework; the bending-sensor study addresses angle-centric sensing; these feed the personalized glove-integration pipeline. 6

2.1 Experimental stress–strain response alongside constitutive model fits. The Yeoh and Mooney–Rivlin fits capture the high-strain nonlinear stiffening most closely. The 3rd-order Yeoh model was adopted as the best compromise between fit quality and parameter count. 18

2.2 Schematic of the DolfinX workflow. Material calibration, parametric meshing, and nonlinear FE solves produce mechanical response histories. These feed either the pressure-sensor branch (3D compression/contact) or the bending branch (cavity collapse and sag correction). 26

2.3 Numerical sensitivity checks for the DolfinX pressure-sensor contact simulations. (a–b) Mesh size effect on force and contact area. (c–d) Sensitivity to contact-penalty scaling. Force converges quickly under refinement; contact area is more sensitive to discretization. Moderate-to-large penalty factors produce nearly identical trends. 31

3.1 Visual taxonomy of the primary flexible pressure-sensing mechanisms: piezoresistive, capacitive, iontronic, and triboelectric/piezoelectric. 35

3.2 Comparison of common microstructure geometries under compressive load. Domes exhibit high nonlinearity; interlocking ridges require complex fabrication; porous lattices offer narrow-range sensitivity. The frustum array provides tunable, progressive engagement for both high sensitivity and extended linear range. 38

3.3 Microwave sensor concept and operating modes. 44
3.4 Microwave sensor geometry and interpretation model. 49
3.5 Simulation-guided interpretation of the microwave sensor. 50
3.6 Measured pressure response for four dielectric configurations. 51
3.7 Measured bending response. 52
3.8 Portable nano-VNA validation. 53
3.9 Representative nonlinear FEM outputs used as the mechanics anchor. (a) Large-deformation solutions for a frustum under compression. (b) Reaction force versus strain for several frustum heights. (c) Normalized contact area versus strain for several top radii. These histories are reused by both iontronic and capacitive transduction models. 61
3.10 Why nonlinear material response and evolving contact are retained in the framework. (a) Representative multi-feature sensor geometry and scanned fabricated heights used for comparison. (b) Predicted force growth under compression for hyperelastic, linear-elastic-with-contact, and linear-elastic-with-prescribed-contact models, showing that linearized mechanics underestimates the strong stiffening at larger strain. (c) Predicted contact-area evolution, showing that evolving contact must also be modeled explicitly rather than prescribed as fixed. (d) Absolute capacitance–pressure comparison between representative simulations and experiment. (e) Corresponding normalized response comparison, showing that material and contact modeling both affect the predicted gain. (f) Excess normalized capacitance contribution attributed to the material model, contact model, and their combined effect. Together, these comparisons show why a hyperelastic-contact formulation is used as the common mechanics engine of the design framework. . 62
3.11 Surrogate-assisted range-tunable design workflow. (a) Differential evolution decodes tiered candidate arrays, predicts their responses, screens infeasible configurations, and iteratively minimizes a weighted performance objective. (b) The surrogate-plus-transduction model aggregates tier mechanics, maps the target pressure to displacement, and computes the sliced-capacitance response and associated performance metrics. 63

3.12 Experimental characterization of the selected iontronic frustum design. (a) Exploded schematic of the multilayer stack. (b) Fabricated device and 3D surface-scan confirming printed frustum array preservation. (c) Cyclic capacitance response over 240 min. (d, upper) Hysteresis showing closely tracked curves. (d, lower) Sensitivity–range comparison against literature; present work in red. (e) Normalized capacitance responses of three frustum variants, showing gain–linearity trade-off. 68

3.13 Design rationale for the iontronic EDL pressure sensor. (a) Stack schematic: silver-coated frustum, hydrogel, silver fabric, and packaging. (b) EDL transduction and equivalent circuit. (c) 3D surface scan confirming frustum topography preservation after coating. (d) Normalized capacitance responses of frustum candidates, illustrating gain–linearity trade-off. 70

3.14 Geometry family versus target range. (a) Best linearity within frustum and B-spline families across several pressure ranges. For narrow ranges, frustums achieve high linearity; for wider ranges, B-spline freedom sustains linearity by reshaping deformation and delaying saturation. (b) Sensitivity of best-linearity designs. 79

3.15 Representative feasible 3D wireframes from the B-spline geometry family, spanning near-frustum to strongly reshaped profiles while preserving manufacturable footprints and smooth transitions. 80

3.16 Representative infeasibility screening results during B-spline active learning. Candidates are rejected before FEM if they violate printable bounds: minimum feature size, overhang limits, base-area containment, continuity, or smoothness. Here, 16 of 35 candidates were filtered, with overhang and self-intersection violations dominant. Screening preserves FEM budget for manufacturable designs. 82

3.17 Representative optimizer comparison for range-tunable design. (a) Final linearity achieved by differential evolution (DE) and Bayesian optimization (BO). (b) Final solution quality versus wall-clock time. DE consistently reached better solutions and exceeded $R^2 = 0.99$ threshold, motivating its use as the default optimizer. 84

3.18 B-spline array optimization pipeline. Differential-evolution search operates on B-spline shape parameters, tier heights, and fractional assignments. Variables are decoded into a discrete array, evaluated by surrogate-plus-sliced-capacitance model, checked against infeasibility criteria, and scored with a weighted objective and structural penalty. 85

3.19 Range-specific optimized B-spline arrays from the same surrogate and framework. (a) Baseline capacitance for three designs: 0–10 kPa (linearity-optimized), 0–10 kPa (weighted linearity–sensitivity), and 0–230 kPa. (b) Low-range response (0–10 kPa). (c) Full-range response (0–230 kPa). (d–f) Optimized tier heights, cell counts, and summary metrics showing how target range and weighting lead to different arrays. 86

3.20 Design progression from single-cell baseline to optimized 12-tier array targeting 0–200 kPa. (a) Linearity improves from $R^2 = 0.876$ to 0.999. (b) Sensitivity curves: single-tier saturates below 50 kPa; optimized array remains linear across full range. (c) Non-uniform tier heights with cell counts. (d) Absolute capacitance: optimized design nearly linear. (e) Residual from linear fit: baseline deviates up to 20%, optimized design within $\pm 1\%$. (f) Progressive-engagement map showing tier engagement sequence. 87

3.21 Simulation and experiment for selected B-spline-derived designs. (a) Absolute capacitance–pressure curves. (b) Normalized $\Delta C/C_0$ responses with linearity values. (c) Normalized responses. Experiments show larger gains than model but preserve monotonic response and variant ordering. 91

3.22 Interactive pressure-sensor design tool. The interface accepts a target pressure range, pad size, linearity–sensitivity weighting, and tier count; it returns an optimized array, predicted $C(P)$ response, and tier-level geometry summary. Example: 0–10 kPa on a 20×20 mm pad with 9 tiers, $R^2 = 0.9958$. 93

4.1 Sensor concept and system overview. (a) Fabricated sensor and readout board. (b) Exploded schematic of multilayer stack: conductive fabric electrodes, PDMS pillar/cavity dielectric, TPU bonding layer. (c) Sensing mechanism: bending drives upper electrode into cavities, increasing effective permittivity. (d–f) Angle-centric response comparison, system signal path, and robotic-finger application. 99

4.2 Comparison of ideal and sag-corrected bending models. Left: flat versus pre-deformed initial state. Center: predicted sensitivity at 100° without sag correction. Right: sensitivity with sag included. Sag correction reduces benefit of widest spans and shifts preferred design toward moderate spacing. 103

4.3 Model-experiment comparison across geometric and material variations. (a) Custom 3D-printed rotary characterization fixture. (b) Sensing mechanism: cavity collapse increases effective permittivity. (c–f) DolfinX predictions of C/C_0 versus bending angle. (g–j) Experimental measurements under matched conditions. (c,g) Pillar spacing fixed at 2 mm, cavity width varied. (d,h) Cavity width fixed at 2 mm, pillar spacing varied. (e,i) Cavity width varied with graphene-loaded dielectric. (f,j) Dielectric constant and graphene loading showing material-driven amplification. 106

4.4 Knee joint angle tracking. (a) Mounting configuration with sensor spanning joint axis. (b) Time-series comparison of sensor output and motion-capture reference during squat cycles, showing 95.20% accuracy. (c) Scatter plot showing linear correlation of $R^2 = 0.9815$ over 0°–90° range. 108

4.5 Validation of placement tolerance and cyclic stability under robotic-finger actuation. (a) Pneumatic soft–rigid hybrid finger with sliding sensor mount. (b) Normalized C/C_0–angle curves at five pivot locations showing closely grouped traces, confirming moderate shifts do not dominate output. (c) Cyclic loading at discrete angles, producing distinct plateaus. (d) Transient response (32 ms) and recovery (45 ms). (e) Power spectral density showing 99.0% below 3 Hz; RMS noise 0.0019 pF. (f–g) Twenty-five-minute continuous recording with no drift; frequency spectrum showing dominant content below 3 Hz. 109

5.1 System-level architecture of the personalized data glove. *Centre:* 3D render with dorsal bending modules and palmar pressure modules, plus wrist electronics. *Left:* CAD output and fabric prototype. *Right:* dorsal and palmar circuit layers with routing. 112

5.2 MediaPipe hand-keypoint detection applied to a dorsal hand photograph. *Left:* 21-landmark skeleton overlaid on the source image. *Right:* landmark index reference with anatomical labels and derived inter-landmark bone lengths. 120

5.3 Gesture-aware skin-strain analysis using the MANO parametric hand model. Area-change ratios $A_{\text{posed}}/A_{\text{flat}}$ are shown for flat, cylindrical grasp, and pinch poses. Largest changes concentrate in fingertips and palmar regions during grasp, while dorsal regions remain closer to neutral, supporting pressure placement palmarly and bending modules dorsally. 122

5.4 Palmar layout engine algorithm. Design-language specification and landmark-derived coordinates enter a dual-layer routing pipeline. Column and row traces are generated with clearance checking and moat routing, producing glove boundary and fabrication outputs. 128

5.5 Interactive interface for reviewing and adjusting the anatomy-to-layout pipeline. The example shows calibrated landmark extraction together with the generated sensor-placement and routing overlays. 129

5.6 End-to-end fabrication pipeline from photograph to manufacturable artefacts. Image capture and landmark extraction feed the layout engine, which produces a JSON manifest. Downstream scripts generate 3D geometry (STL/OBJ) and 2D fabrication files (DXF, Gerber). 130

5.7 Spatial response of the 8×8 capacitive pressure sensor array under single-taxel loading at Row 3, Col 3. The colour map shows the capacitance-derived pressure across all 64 taxels. The pressed pixel reaches 12.0 kPa; the largest neighbouring response is 1.7 kPa (crosstalk). Baseline capacitance: 5.20 pF. 132

5.8 Integrated palmar and dorsal glove measurement layout 135

5.9 Geometric validation of photo-based sensor placement 138

5.10 Data-glove gesture recognition with the integrated bending-sensor glove. (a) Three-sensor glove during recording. (b) Representative capacitance traces from three channels across repeated gesture trials. (c) Confusion matrix for ten-gesture classification (ANN, three-channel), showing reliable separation across gesture classes. 140

List of Tables

2.1 Measured dimensions of representative uniaxial tensile specimens for the printable silicone resin. 14

2.2 Measured dimensions of representative cylindrical compression specimens for the printable silicone resin. 14

2.3 Representative hyperelastic material parameters for the 3D-printed silicone resin obtained from our in-house fitting workflow applied to the tensile and compression test datasets. All parameters are reported in Pa. 17

2.4 Coefficient of determination (R^2) for the hyperelastic model fits to the tensile and compression tests of the 3D-printed silicone resin. 18

2.5 Practical comparison of iontronic material classes for the present design problem. The key selection criterion was compatibility with a fast geometry-design-to-fabrication loop, rather than maximizing material novelty. 22

2.6 Main software libraries used in the computational workflow of this thesis. . 25

3.1 Design requirements used to evaluate the pressure-sensing approaches in this chapter. 42

3.2 Microwave resonator route: prototype and RF characterization summary. . 48

3.3 Implementation summary of the Chapter 3 design framework for the two local-readout pressure-sensor routes. 56

3.4 Shared mechanics, different transduction models. The same FEM backbone feeds both mechanisms, but the electrical interpretation and therefore the useful geometry family differ. 58

3.5 Iontronic EDL pressure sensor: fabrication and characterization summary. 73

3.6 Solid capacitive route: design, fabrication, and validation settings. 88

4.1 Representative bending-sensor architectures and their relation to the pillar/air capacitive design proposed in this work. 98

4.2 Geometry and simulation parameters used in the pillar-based bending sensor sweep. Units: mm unless otherwise stated. 104

5.1 Literature-informed design targets and constraints for the personalized OTG data glove. 118

5.2 Layout generation and placement accuracy across six participants 136

5.3 Placement reproducibility of the photo-based pipeline 137

5.4 Gesture-recognition accuracy for the three-channel and five-channel bending-sensor glove configurations. 140

5.5 Comparison of the bending-sensor glove against representative gesture-recognition gloves. 141

Chapter 1

Introduction

1.1 Background

The human hand supports tasks ranging from precision pinch to power grasp through coordinated motion across more than twenty joints and through distributed tactile interaction with objects. Quantitative assessment of hand function is therefore important in rehabilitation, assistive technology, and human-machine interaction, where both joint motion and hand-object contact must be captured in a continuous and interpretable way. The clinical demand is substantial: stroke affects approximately 12.2 million people annually worldwide [1], and upper-limb motor impairment — including reduced dexterity and grip — is present in around 80% of acute stroke survivors, making recovery of hand function a major rehabilitation target [2]. Hand and finger injuries from occupational and daily-life trauma add a further burden, accounting for roughly one-third of work-related injuries and a disproportionate share of long-term disability [3].

Despite decades of instrumentation research, measuring hand function outside the laboratory remains difficult. The hand combines large joint excursions with intermittent, spatially localized contact on curved, compliant surfaces. Under ambulatory conditions, wearable sensors are also affected by soft-tissue motion, fit, and environmental variation in ways that are usually absent from benchtop tests. Laboratory-grade systems such as motion capture and instrumented rigs still provide the cleanest reference measurements, but they are not practical for on-the-go (OTG) deployment in clinical, workplace, or daily-use settings (here OTG denotes ambulatory, outside-the-laboratory use, not to be confused with other common uses of the acronym, such as USB On-The-Go).

Soft wearable sensors offer a plausible route to ambulatory hand monitoring because they can conform to curved surfaces and tolerate repeated deformation. The harder problem is not demonstrating an isolated sensor coupon, but turning such sensors into a glove that can be worn repeatedly and still produce useful data. In this thesis, the glove is treated as the system-level test bed for that problem. Fit, sensor placement, wearability, and interconnect routing are therefore not secondary packaging details; they are part of the sensing problem itself and directly affect measurement fidelity during use.

1.2 Motivation

For hand-function assessment, neither kinematics nor contact is sufficient alone. Reduced object contact after stroke may result from inadequate joint motion or from an inability to generate stable grip force; distinguishing these cases requires bending and pressure measurements together [4]. The measurements must also remain interpretable across repeated use. Reviews of wearable hand goniometry and instrumented gloves identify donning variability, calibration burden, and cross-session repeatability as practical barriers to longitudinal use [5, 6, 7].

Accordingly, this thesis treats the glove as part of the sensing system rather than as a passive carrier. Fit, comfort, sensor placement, and manufacturability influence whether a sensor can be positioned consistently and worn for long enough to provide useful data. Since these factors are also associated with sustained adoption of assistive technologies [8, 9, 10, 11, 12], the work combines pressure and bending sensing with anatomy-aware glove personalization. A parametric pattern and sensor layout derived from hand measurements provide one route to reducing fit-driven misalignment [13, 14].

1.3 Gaps and challenges

Against the ambulatory-use background established above, four technical gaps in existing approaches motivate this thesis.

Gap 1: No reusable framework for simulation-driven pressure sensor design. Microstructure geometry is the dominant design lever for flexible pressure sensors: features such as pyramids, domes, frustums, and porous lattices control effective stiffness, contact-area growth, and electric-field evolution under compression, governing sensitivity, linear

range, and hysteresis [15, 16]. Because the relevant deformation and contact mechanics are strongly nonlinear, the geometry-to-performance mapping is not accessible by intuition or by small-scale empirical screening alone. The field has made meaningful progress toward model-guided design: Ruth *et al.* developed predictive equations linking pyramidal microstructure geometry to capacitive sensor performance [17, 18], and FEM-based comparison studies have reduced unguided fabrication for specific geometry families [19, 20]. However, the reviewed approaches address single repeating cells or pre-selected geometries, are typically tied to one transduction mechanism, and do not search an array-level design space for a user-specified pressure window [17, 21, 22]. To the author's knowledge, the reviewed literature does not describe a framework that combines separable nonlinear contact mechanics and transduction physics with array-level optimization against an explicit target pressure window. This gap motivates the simulation- and surrogate-assisted design framework developed in Chapter 2 and applied in Chapter 3.

Gap 2: Pressure sensor research prioritizes sensitivity; linearity receives insufficient design attention. The vast majority of flexible pressure sensor studies optimize for sensitivity and report linearity only as a secondary metric, if at all [23, 24, 25, 26]. For isolated benchtop demonstration, peak sensitivity is the natural headline figure. In wearable deployment, however, linearity is also important: a nonlinear sensor mounted on a glove substrate operates at a resting pressure that varies with fit, donning depth, and wrist cuff tension, so a shift in baseline can change both offset and effective gain [27, 6]. A more linear response can simplify recalibration, although it does not remove the need to manage drift, hysteresis, and other sources of measurement variability. Although recent work has produced sensors with broadened linear ranges through gradient microstructures, hierarchical architectures, and wave electrodes [21, 22, 28, 29], the reviewed designs are optimized for specific declared pressure windows rather than through a retargetable design loop. The unmet need is therefore a requirements-driven approach that can target a specified pressure window while balancing sensitivity and linearity. Chapter 3 addresses this need through systematic design optimization.

Gap 3: Flexible bending sensors transduce local surface strain and are inherently placement-sensitive. Most glove-based bending sensors report strong benchtop sensitivity, but their output reflects local surface strain at the sensor–substrate interface rather than the anatomical joint angle directly. In a wearable glove, local strain depends not only on joint rotation but also on substrate pre-tension, soft-tissue distribution, skin sliding, and the offset between the sensor midplane and the joint axis. The consequence is that the calibration curve is placement-specific and donning-specific: cross-session repeatability

is poor, and re-calibration is required after every donning event [7, 6]. Placement-induced signal variability of 15–30% has been quantified in glove evaluations even when subjects are retrained on the same sensor [6, 27]; for distal interphalangeal joints specifically, fit-dependent offsets have been found severe enough to question the viability of strain-gauge gloves without multi-size hardware [27]. Attempts to decouple bending from stretching at the sensor design level have reduced but not eliminated the problem, since post-hoc calibration or model correction is still required to recover consistent joint-angle estimates across users [30, 31, 32]. This gap motivates an angle-centric transduction architecture; the mechanism-level analysis and design response are developed in Chapter 4.

Gap 4: No automated pipeline connects hand anatomy to electronics-ready glove fabrication outputs. Personalizing glove dimensions to individual hand measurements has been studied in the ergonomics literature [13, 33], and measurement-based glove pattern methods have been proposed for smart wearables [14]. The approaches identified in the reviewed literature rely on physical measurement, manual pattern drafting, or separate layout decisions for sensing elements and electrical routing. The review did not identify a photo-based workflow that produces both electronics-ready fabrication outputs (DXF cut patterns and Gerber routing files) and a constraint-checked dual-layer routing layout from hand landmarks. This gap motivates the anatomy-to-layout pipeline and modular electronics architecture developed in Chapter 5.

1.4 Research objectives

In response to the four gaps identified above, the objectives of this thesis are threefold. Objective 1 addresses the two linked pressure-sensing gaps (Gaps 1 and 2), while Objectives 2 and 3 address the bending-sensing and personalized-integration gaps, respectively:

- **Objective 1: Pressure/contact sensing.** To develop soft, wearable-compatible pressure sensing approaches for palmar contact measurement, with linearity treated as a primary design requirement alongside sensitivity, and to establish a simulation-driven design framework that replaces trial-and-error geometry selection with a reusable, requirements-driven optimization pipeline.
- **Objective 2: Bending/joint-angle sensing.** To develop an angle-centric capacitive bending sensor for finger joint-angle monitoring across the 0°–90° range relevant to hand use, and to reduce sensitivity to placement variability through analytical

modeling and finite-element-guided design constraints. A large-joint study is used to assess the transferability of the sensing principle, rather than as the primary application.

- **Objective 3: Personalized integration.** To develop an automated photo-based pipeline that converts hand landmark measurements into anatomy-referenced sensor placements and electronics-ready fabrication outputs (DXF, Gerber), enabling glove-based deployment that reduces inter-user placement variability and lowers the calibration burden associated with anatomy-mismatched sensor positioning.

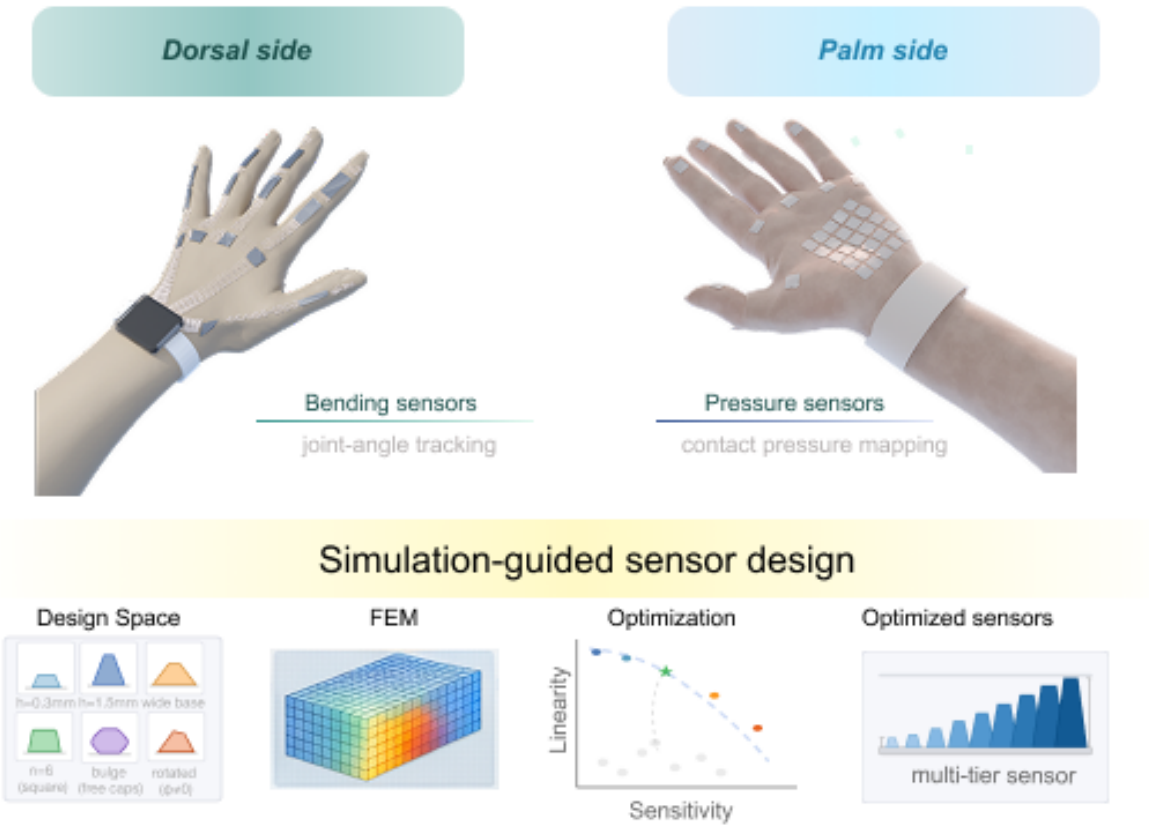


Figure 1.1: Structural overview of the thesis. A shared methodology backbone provides nonlinear material modeling and FEM; the pressure-sensor chapter develops a range-tunable optimization framework; the bending-sensor study addresses angle-centric sensing; these feed the personalized glove-integration pipeline.

1.5 Thesis contributions

The four contributions below correspond directly to the four gaps identified above. Each closes one gap; together they establish a sensor-first, modeling-guided approach to practical ambulatory hand sensing.

- **A simulation-driven design framework for soft capacitive pressure sensors (Chapters 2–3).** The framework separates nonlinear contact mechanics from transduction-specific physics, allowing the same DOLFINx FEM backbone and surrogate-model infrastructure to be applied across different sensing mechanisms without rebuilding the mechanics layer. It operates at the multi-tier array level rather than the single cell, and treats the target pressure window as an explicit optimization input rather than a fixed property of a pre-selected geometry — three properties absent from prior modeling work. The shared Yeoh-calibrated constitutive model and instrumentation protocols developed in Chapter 2 underpin both pressure and bending sensor studies, making cross-mechanism comparisons valid on common footing.
- **Iontronic and capacitive pressure sensor arrays with linearity as a primary design objective (Chapter 3).** The multi-tier frustum array architecture is designed to mitigate the sensitivity–linearity trade-off of single-cell designs: staggered engagement thresholds distribute the operating range across tiers, supporting high low-load sensitivity from the first tier and a more nearly constant slope across the target window. Linearity is treated as a first-class design target driven by wearable-deployment constraints, and the design principle is examined across two transduction mechanisms (iontronic EDL and conventional capacitive). Under the tested conditions, the results indicate that the approach is not limited to one material system. A microwave resonator route was also explored and is retained in Chapter 3 as the design study that motivated the pivot to soft local-readout architectures.
- **An angle-centric pillar-structured capacitive bending sensor (Chapters 2 and 4).** The sensor is designed to make transduction depend on integrated bending curvature across a joint rather than solely on local surface strain, thereby reducing sensitivity to moderate mounting shifts and skin-stretch contamination. The principle is implemented through an air-cavity pillar architecture with an analytical model that accounts for electrode sag and provides a direct design handle on sensitivity and operating range. Robotic-finger testing (32 ms response and stable placement-tolerance curves) evaluates the intended hand-use case. A separate large-knee-joint validation (95.20 % accuracy, $R^2 = 0.9815$ against motion capture) assesses transferability of the sensing principle across anatomical scales.

- **A photo-based anatomy-to-layout pipeline producing electronics-ready glove fabrication outputs (Chapter 5).** A single dorsal hand photograph drives the full pipeline: MediaPipe landmark detection extracts 21 anatomical keypoints; a parametric layout engine converts them to anatomy-referenced sensor placements and a constraint-checked dual-layer routing design; and parallel downstream scripts produce 3D geometry (STL/OBJ) and 2D fabrication files (DXF/Gerber) from a shared JSON manifest — without manual CAD intervention. A MANO-based skin-strain analysis justifies the placement zone assignments, and an initial six-participant gesture study demonstrates 98.7 % classification accuracy with three bending channels and no per-user hardware refitting.

1.6 Thesis outline

The remainder of this thesis is organized as follows.

Chapter 2 establishes the shared methodological backbone used throughout the thesis, including material characterization, instrumentation protocols, nonlinear FEM simulation workflows, and verification and validation considerations. These tools are shared across the pressure and bending sensor chapters and provide the foundation on which the later design-automation workflow is built.

Chapter 3 develops the pressure sensors. It opens with a review of relevant sensing technologies and design requirements, motivating the microstructure-focused design strategy adopted in this work. The chapter then presents a microwave resonator approach, introduces the reusable FEM-, surrogate-, and optimization-based design framework, and applies that framework to iontronic and conventional capacitive sensors. The iontronic prototype is selected as the primary design and characterized in detail, while the capacitive route demonstrates the framework's range-tunable generality.

Chapter 4 presents the angle-centric capacitive bending sensor. It begins with a targeted review of bending sensing approaches and the requirements specific to joint-angle monitoring under OTG constraints, then develops the analytical capacitance model, FEM-guided design study, and experimental validation through benchtop calibration and robotic-finger testing. A large-joint knee study provides a separate assessment of transferability of the sensing principle.

Chapter 5 translates the sensor-level results into a wearable deployment platform. It introduces the anatomy-to-layout pipeline, including landmark capture, parametric glove pattern generation, sensor placement mapping, and prototype realization. The chapter

reviews relevant glove design literature in context, describes the integrated wired glove prototype, and reports glove-level studies including gesture-recognition results with the embedded bending-sensor system.

Chapter 6 provides a concise thesis-level synthesis, reflects on what the work does and does not establish, and identifies the remaining validation, integration, and material-stability questions that must be resolved before clinical translation.

Chapter 2

Methodology

This chapter outlines the experimental and computational foundations for the subsequent sensor designs. First, mechanical testing establishes the hyperelastic parameters for the core 3D-printable silicone. Next, standardized capacitive readout and calibration protocols provide consistent evaluation metrics. Finally, an open-source FEM workflow is verified against mesh and penalty sensitivities, establishing the simulation pipeline needed to conduct the parametric geometry sweeps in Chapters 3 and 4. The design automation layer that builds on these tools—surrogate modeling, transduction models, and array-level optimization—is presented in Chapter 3.

2.1 Motivation for Simulation-Driven Sensor Design

The performance of glove-integrable soft sensors is governed by coupled geometry-material-contact effects that make purely empirical, trial-and-error design slow, expensive, and difficult to generalize. In microstructured pressure sensing, geometry can dominate sensitivity, linear range, and hysteresis through nonlinear contact evolution [15, 16]. In kinematic sensing, placement and substrate mechanics can alter the mapping between local deformation and joint angle. These dependencies make exhaustive fabrication-based exploration impractical and motivate the adoption of predictive modeling, efficient design-space exploration strategies, and automated pipelines.

2.1.1 Finite element modeling of soft sensors

Finite element methods (FEM) are widely used in soft-sensor design because they can capture large deformation, nonlinear material behavior, and evolving contact conditions that are difficult to treat analytically. This geometry-first emphasis is consistent with recent reviews, which organize flexible pressure sensors largely in terms of morphology families and show that microstructure engineering remains one of the main routes for tuning sensitivity, linear range, hysteresis, and durability [34, 35, 36, 37]. Within that landscape, FEM is typically used to connect a chosen geometry to stress concentration, contact evolution, effective stiffness, and a mechanism-specific electrical response before fabrication [38, 26, 39, 15].

The majority of existing FEM-based design studies are geometry-family-specific: they derive predictive rules within one morphology family at a time — triboelectric contact morphologies, cylindrical ladders, micro-cones, micro-pyramids — and mechanism-locked, because the governing coupling is written for one transduction physics only [15, 26, 39, 20]. The current literature is therefore rich in predictive studies but thinner in reusable frameworks that span multiple geometry families and multiple transduction mechanisms with the same computational pipeline. A related limitation is that optimization is usually posed for one target pressure window; an important counterexample is the positive-design strategy of Xu *et al.*, which uses a hyperelastic/contact model to pre-calculate microstructure distributions for a desired linear region [40].

Predictive simulation also depends on appropriate constitutive descriptions for elastomers and gels, including Yeoh, Ogden, and Mooney–Rivlin models, as well as attention to mesh convergence, contact treatment, and viscoelasticity when hysteresis and rate effects are relevant [41, 42, 43, 44]. Reviews of flexible pressure sensors have argued that theoretical modeling is important for optimizing microstructured designs and for reducing the cost of repeated design iteration [35, 37]. A practical consequence is that simulation-based sensor design cannot be approached with linear elasticity: microstructure deformation under contact involves strains large enough that a linear constitutive model predicts qualitatively wrong stiffness evolution and contact-area growth, which are the two quantities that govern sensitivity and linear range [17, 19, 41, 42]. Because most existing FEM studies treat simulation as a forward characterization tool for a fixed geometry rather than as an invertible model suitable for optimization, this modeling gap is a direct reason why geometry-space search and inverse design remain difficult in the soft-sensor literature. This perspective underlies the modeling setup in this chapter and the modeling-guided design studies in Chapters 3 and 4.

2.1.2 Surrogate modeling and automated design

Although FEM can be predictive, repeated simulation over large parameter spaces is computationally expensive, especially when multiple geometric variables are varied or when mechanical and electrical analyses are coupled. For multi-tier pressure sensor arrays, even a modest design with N tiers and k geometry descriptors per tier creates an $N \times k$-dimensional continuous search space; once tier multiplicities and ordering are included, the search becomes mixed discrete–continuous and effectively combinatorial.

Surrogate modeling addresses the per-query cost of this problem by learning an inexpensive approximation to the simulation response surface, enabling rapid sensitivity analysis, inverse design, and optimization [45, 20, 46]. However, surrogates do not remove the cost of generating training data. More general engineering reviews make this explicit: surrogate models emulate expensive high-fidelity FEM computations, but the training labels must still be computed from those simulations, so data acquisition becomes the dominant bottleneck in high-dimensional design spaces [47].

Active learning and Bayesian optimization have therefore become established strategies for expensive design problems, in which each new simulation or experiment is selected for maximum information gain [48, 49]. Rather than relying on one-shot grids or random samples, these approaches update the surrogate sequentially, balancing exploration of poorly sampled regions against exploitation near promising optima. The design automation layer built on these tools is described fully in Chapter 3: a structured grid-based sweep is sufficient for the lower-dimensional frustum geometry family, whereas the higher-dimensional B-spline family requires active-learning-guided sampling.

2.1.3 Personalized integration and anatomy-to-layout mapping

Even with an optimized sensor element, OTG performance depends strongly on how the sensor is deployed on the body. Personalized integration is important because anatomy, joint location, and placement variability affect both signal generation and signal interpretation. Additive manufacturing and digital fabrication have lowered the barrier to producing user-specific geometries in biomedical devices and wearables, making customized form factors increasingly practical [50, 51, 52, 53, 54].

For glove-integrated sensing, a particularly important personalization problem is layout. A one-size-fits-all glove pattern places sensors at nominal anatomical locations that may not coincide with an individual user's joint axes. Because bending signals are placement-sensitive, such misalignment can introduce systematic error that is difficult to remove

through calibration alone. This motivates anatomy-to-layout pipelines that map a compact set of hand measurements to a parametric glove pattern and sensor placement plan [55, 56], which is the subject of Chapter 5.

2.2 Material Characterization for Hyperelastic Modeling

2.2.1 Mechanical Testing Setup

For the materials used in this work, we carried out a combination of uniaxial tensile and compression tests to obtain stress–strain data suitable for constitutive modeling and simulation. The primary material characterized in detail was the 3D-printed silicone resin that forms the bulk of the pressure- and bending-sensor structures. This resin was selected because additive manufacturing enables rapid iteration of cavities, thin walls, and other geometry features that directly influence sensor mechanics.

For the printable silicone resin, uniaxial tensile tests were performed on dogbone-style specimens at a crosshead speed of 50 mm/min. Force and crosshead displacement were recorded throughout the test, and engineering strain was obtained from the machine displacement with a compliance correction; digital image correlation was not used. Representative measured specimen dimensions are listed in Table 2.1. The tensile specimens had gauge widths in the range 5.0–6.0 mm, thicknesses of 2.0–2.5 mm, and gauge lengths of 70–74 mm.

In addition to the tensile tests, we performed cylindrical compression tests on the same silicone resin to calibrate the constitutive law used in the finite-element simulations. Representative specimen dimensions are summarized in Table 2.2. These compression tests form the basis for the Yeoh-model fits later used in the DolfinX pressure-sensor simulations.

2.2.2 Constitutive Modeling and Model Selection

To accurately simulate the mechanical response of the 3D-printed silicone elastomer used in both the pressure and bending sensors, we fitted the experimental stress–strain data to several standard hyperelastic constitutive models using a custom Python workflow. The same fitting procedure was applied independently to both the uniaxial tensile data (dogbone specimens, Section 2.2.1) and the cylindrical compression data, producing the

Table 2.1: Measured dimensions of representative uniaxial tensile specimens for the printable silicone resin.

Specimen	Width w (mm)	Thickness t (mm)	Gauge length GL (mm)
1	6.0	2.5	74
2	5.0	2.0	70
3	5.2	2.4	72

Table 2.2: Measured dimensions of representative cylindrical compression specimens for the printable silicone resin.

Specimen	Radius r (mm)	Thickness t (mm)
1	14.0	12.5
2	14.4	12.4
3	14.2	12.6

two parameter columns shown in Table 2.3. Because the dominant loading mode in the pressure-sensor microstructures is uniaxial compression, the compression-derived Yeoh parameters were used as the nominal material law in all DolfinX simulations; the tensile fits are reported alongside them for completeness and as a check on parameter consistency across deformation modes. The compression workflow is described first because it drives the simulation results. Compression tests on cylindrical samples (representative radius $r \approx 14.2$ mm, Section 2.2.1) were processed into engineering strain and stress,

$$\varepsilon_{\text{eng}} = -\frac{\Delta L}{L_0}, \qquad \sigma_{\text{eng}} = -\frac{F}{\pi r^2}, \tag{2.1}$$

where L_0 is the original specimen height

$$\varepsilon_{\text{true}} = \ln(1 - \varepsilon_{\text{eng}}), \qquad \sigma_{\text{true}} = \frac{\sigma_{\text{eng}}}{1 - \varepsilon_{\text{eng}}}, \tag{2.2}$$

and used as inputs to the constitutive fits.

We evaluated multiple incompressible hyperelastic forms implemented in the `Hyperelastic` class: Neo–Hookean, Mooney–Rivlin (2-, 3-, and 5-parameter variants), Yeoh (up to 3rd order), and Ogden (not ultimately used for the silicone fits, but available for completeness). The fitting scripts rely on SciPy's non-linear solvers: a Levenberg–Marquardt least-squares routine (`method = 'lm'`) for Neo–Hookean, Yeoh, Gent, Veronda–Westmann, and

Humphrey models, and a trust-region constrained optimizer (`method = 'trust-constr'`) with linear or non-linear constraints for Mooney–Rivlin and Ogden. In particular, Mooney–Rivlin parameters were constrained to be strictly positive via a linear inequality constraint, while Ogden parameters used a product constraint to avoid non-physical parameter combinations.

These constitutive models were written in terms of the invariants of the right Cauchy–Green tensor $C = F^{\mathrm{T}}F$:

$$I_1 = \mathrm{tr}(C), \qquad I_2 = \frac{1}{2}\left[(\mathrm{tr}(C))^2 - \mathrm{tr}(C^2)\right], \qquad I_3 = \det(C).$$

Here, I_1 represents the sum of the principal stretch contributions, I_2 reflects the pairwise products of the principal stretches, and $I_3 = J^2$ characterizes the volumetric change through $J = \det(F)$. To separate deviatoric deformation from volumetric deformation, we used the modified invariants

$$\bar{I}_1 = J^{-2/3}I_1 = I_1 I_3^{-1/3}, \qquad \bar{I}_2 = J^{-4/3}I_2 = I_2 I_3^{-2/3}.$$

Using this notation, the strain-energy density functions fitted in our workflow were as follows. In each expression, D_1 is the compressibility parameter used to penalize volumetric change.

Neo–Hookean (1 parameter). The simplest invariant-based model, with a single deviatoric coefficient:

$$W_{\mathrm{NH}} = C_{10}(\bar{I}_1 - 3) + \frac{1}{D_1}(J-1)^2.$$

Mooney–Rivlin, 2-parameter. Adds a $\bar{I}_2$ term to capture the influence of the second invariant on the stress response:

$$W_{\mathrm{MR,2}} = C_{10}(\bar{I}_1 - 3) + C_{01}(\bar{I}_2 - 3) + \frac{1}{D_1}(J-1)^2.$$

Mooney–Rivlin, 3-parameter. Introduces a coupling term between the two invariants:

$$W_{\mathrm{MR,3}} = C_{10}(\bar{I}_1 - 3) + C_{01}(\bar{I}_2 - 3) + C_{11}(\bar{I}_1 - 3)(\bar{I}_2 - 3) + \frac{1}{D_1}(J-1)^2.$$

Mooney–Rivlin, 5-parameter. The most general Mooney–Rivlin form fitted here, adding second-order terms in both invariants:

$$W_{\mathrm{MR},5} = C_{10}(\bar{I}_1 - 3) + C_{01}(\bar{I}_2 - 3) + C_{11}(\bar{I}_1 - 3)(\bar{I}_2 - 3) + C_{20}(\bar{I}_1 - 3)^2 + C_{02}(\bar{I}_2 - 3)^2 + \frac{1}{D_1}(J-1)^2.$$

Yeoh, 3rd order. Depends only on $\bar{I}_1$, using successive powers to capture stiffening at large strains:

$$W_{\mathrm{Yeoh}} = C_{10}(\bar{I}_1 - 3) + C_{20}(\bar{I}_1 - 3)^2 + C_{30}(\bar{I}_1 - 3)^3 + \frac{1}{D_1}(J-1)^2.$$

An Ogden 2nd-order model was also benchmarked in the fitting script and is included in the R^2 comparison in Table 2.4; however, because the downstream thesis workflow and the later finite-element implementation relied primarily on the invariant-based Mooney–Rivlin and Yeoh forms, those are the constitutive equations written explicitly here.

For the silicone compression data, we fitted the cylindrical specimens summarized above, with tested specimen heights ranging from approximately 12.0–12.6 mm. Each sample was processed to remove pre-contact drift (distance and load re-zeroed at the last zero-load point) and truncated at the maximum displacement, after which only the loading branch with positive load was retained. For each sample, we compared the following models using the true-stress representation as the reference:

- Neo–Hookean (1 parameter),
- Mooney–Rivlin with 2, 3, and 5 parameters,
- Yeoh, 3rd order,
- Ogden, 2nd order.

Model quality was assessed using the coefficient of determination (R^2) between experimental and modeled engineering stress across the fitted strain range. For the silicone compression samples, the 5-parameter Mooney–Rivlin and 3rd-order Yeoh models consistently achieved the best fits, with R^2 values typically in the range 0.997–0.998, while simpler Neo–Hookean and lower-order alternatives under-fit the strain-stiffening regime. Representative parameter sets obtained from our in-house fitting workflow for both tensile

Table 2.3: Representative hyperelastic material parameters for the 3D-printed silicone resin obtained from our in-house fitting workflow applied to the tensile and compression test datasets. All parameters are reported in Pa.

Model	Tensile fit	Compressive fit
Neo–Hookean	$\mu = 7.22 \times 10^4$	$\mu = 3.06 \times 10^5$
Mooney–Rivlin	$C_{10} = 1207.4$	$C_{10} = 1.0079225$
(3 parameter)	$C_{01} = 14043.7$	$C_{01} = 38981.286$
	$C_{11} = 1$	$C_{11} = 3638021.71$
Mooney–Rivlin	$C_{10} = 2.15 \times 10^5$	$C_{10} = 688.56916$
(5 parameter)	$C_{01} = 2.15 \times 10^5$	$C_{01} = 1.0691542$
	$C_{11} = 1.23 \times 10^5$	$C_{11} = 2.23049481$
	$C_{20} = 1.004$	$C_{20} = 1.892382$
	$C_{02} = 2.29 \times 10^5$	$C_{02} = 840075.407$
Yeoh	$C_{10} = 3.89 \times 10^4$	$C_{10} = 9525.64679$
(3rd order)	$C_{20} = -286.07655$	$C_{20} = 6464859.19$
	$C_{30} = 1.48407376$	$C_{30} = 65598253.9$

and compression tests are summarized in Table 2.3, and the corresponding R^2 values are listed in Table 2.4. We also include a 2nd-order Ogden fit in the R^2 comparison as an additional benchmark, even though the later finite-element workflow was based on the Yeoh parameterization.

For the FEM simulations used in the pressure-sensor design and bending-sensor analysis, we ultimately adopted the 3rd-order Yeoh model as the material law in both COMSOL and DolfinX. As shown in Figure 2.1, the higher-order C_{20} and C_{30} terms allow the Yeoh model to capture the nonlinear strain-stiffening behavior observed in the silicone resin without requiring the full 5-parameter Mooney–Rivlin form. For the compression data used as the nominal material law, Yeoh-3 ($R^2 = 0.9995$) matched or slightly exceeded the 5-parameter Mooney–Rivlin fit ($R^2 = 0.9983$; Table 2.4) while using two fewer parameters, making it the preferred choice on both accuracy and parsimony grounds. Yeoh-3 also keeps the number of parameters small enough to be robustly identified from the available compression data and straightforwardly implemented in UFL, while still matching the experimental curves to within measurement uncertainty.

In the results chapters (Chapters 3 and 4), we therefore use the Yeoh parameterization as the nominal material law in DolfinX and COMSOL, with Table 2.3 serving as the summary of the experimentally fitted tensile and compressive parameter sets for the printable silicone resin. Sensitivity studies confirm that modest perturbations of these parameters

Table 2.4: Coefficient of determination (R^2) for the hyperelastic model fits to the tensile and compression tests of the 3D-printed silicone resin.

Hyperelastic model	Tensile	Compressive
Neo–Hookean	0.897909	0.803007
Mooney–Rivlin (3 parameter)	0.992440	0.994243
Mooney–Rivlin (5 parameter)	0.998213	0.998349
Yeoh (3rd order)	0.997490	0.999460
Ogden (2nd order)	0.996985	0.926925

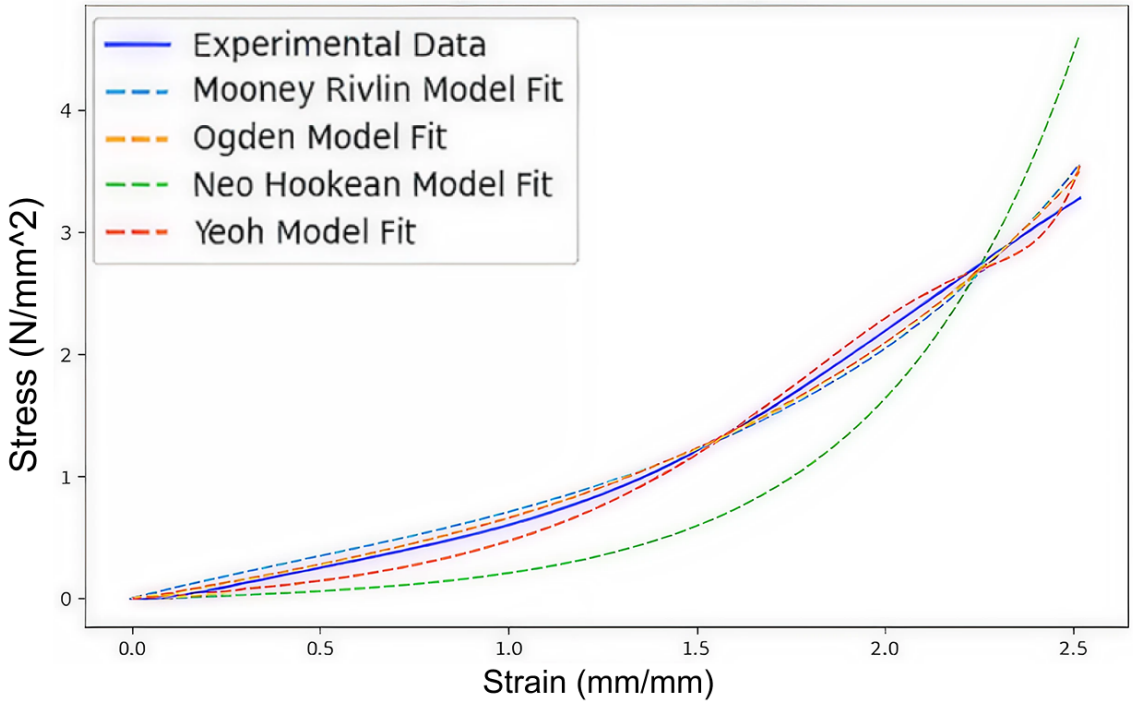


Figure 2.1: Experimental stress–strain response alongside constitutive model fits. The Yeoh and Mooney–Rivlin fits capture the high-strain nonlinear stiffening most closely. The 3rd-order Yeoh model was adopted as the best compromise between fit quality and parameter count.

do not qualitatively change the simulated sensor response, so the Yeoh model provides

a stable and computationally efficient basis for the subsequent pressure-sensor surrogate modeling and bending-sensor strain analysis. The finite-element models assume idealized quasi-static hyperelasticity to isolate the effect of geometric design variables; the cyclic hysteresis of soft elastomers is evaluated experimentally during the sensor characterization reported in Chapters 3 and 4.

2.3 Experimental Instrumentation and Evaluation Protocols

2.3.1 Readout Electronics

Both the pressure and bending sensors in this thesis rely on capacitive readout. Capacitance measurements were performed using a precision LCR meter (Keysight E4980AL/032, 20 Hz–300 kHz with DCR capability). Unless otherwise stated, capacitance was recorded at a 1 kHz test frequency with 0 V DC bias. The AC excitation amplitude was set to 1 V for all fully solid-state capacitive characterizations, and lowered to 0.5 V for all iontronic characterizations to minimize electrochemical degradation of the ionic gel. For the LCR equivalent-circuit setting, fully solid-state capacitive sensors were measured in Cp/Rp (parallel) mode, which is appropriate when the dielectric loss is low and the measured impedance is predominantly capacitive. Iontronic sensors were measured in Cs/Rs (series) mode because the ionic medium introduces a significant series resistance from bulk ionic transport; the series model separates this resistance from the interfacial capacitance more accurately than the parallel equivalent at the 1 kHz measurement frequency. For rapid-prototyping experiments, we also evaluated a capacitance-to-digital converter (CDC) prototype (PCap04).

2.3.2 Calibration and Characterization Fixtures

Controlled normal loading was applied using a Mark-10 force test stand (F305 frame) with a 100 N load cell. For the pressure-sensor experiments, the applied load was converted to nominal pressure using the indenter geometry and contact area adopted in the corresponding experiment, so the calibration variable reported in the pressure-sensor chapter is pressure rather than force. The indenter geometry and contact conditions used for each sensor are specified in the corresponding chapter.

For bending-sensor characterization, a custom stepper-driven rotary fixture was used to apply controlled joint-angle increments. One end of the sensor is clamped to a fixed mount while the other is attached to a motorized rotating arm that steps through prescribed angle increments; capacitance was recorded with the same LCR meter setup described above. The full fixture design, photograph, and the specific protocol used for the geometry parameter sweeps are described in Section 4.5.1.

2.3.3 Data Acquisition and Synchronization

Accurate synchronization between the applied mechanical load and the electrical response is critical to avoid introducing artificial hysteresis into sensor characterization. Data from both the Keysight LCR meter and the Mark-10 force stand were acquired simultaneously over a serial interface using a custom polling script. Because the precision LCR measurement acted as the bottleneck—operating at an effective sampling rate of approximately 1 to 2 Hz—the synchronization protocol was driven by the LCR meter's clock. Immediately after a capacitance reading was successfully queried and received, the script queried the corresponding real-time force and displacement values from the much faster Mark-10 load cell. To ensure this 1–2 Hz sampling rate provided sufficient temporal resolution without latency-induced measurement artifacts, the motorized test stand was programmed to execute all loading profiles at low, quasi-static speeds.

2.3.4 Testing Protocols

Unless otherwise specified in the individual experimental studies, all reported sensor output values denote the mean across physically tested prototypes or repeated trials, with shaded regions or error bars corresponding to one standard deviation.

- **Repeatability, hysteresis, and drift:** Repeatability, hysteresis, and drift were evaluated using cyclic loading and constant-hold tests. The detailed loading schedules, pressure or angle ranges, and quantitative results are reported in the corresponding sensor chapters.
- **Rate effects:** Where relevant, we considered the dependence of sensor output on loading rate and hold time, particularly in the presence of viscoelastic creep or relaxation [57].

- **Task segmentation ("bouts"):** For dynamic experiments, signals were analyzed within task windows (e.g., repeated grasp cycles) rather than over undifferentiated continuous recordings, following bout-style segmentation commonly used for real-world wearable datasets [58].
- **Signal processing and validity criteria:** Raw signals were filtered when needed to suppress high-frequency noise while preserving the dominant task dynamics. Filter type, parameters, and any trial-exclusion criteria are reported for the individual experiments [58].
- **Agreement against ground truth:** For each sensor, the measured capacitance response was compared against the corresponding reference variable, namely applied pressure for the pressure sensor and reference angle for the bending sensor. The detailed error metrics and performance summaries are reported in the corresponding sensor chapters rather than fixed globally in this methodology chapter [59].

2.3.5 Iontronic Material Selection

The iontronic pressure sensor developed in Chapter 3 requires a soft ionic conductor to form the electrical double layer (EDL) interfaces that provide the dominant capacitive signal. Because the material choice constrains the fabrication loop and directly affects measurement stability, the selection rationale is recorded here alongside the other methodology decisions that are shared across chapters.

Iontronic sensors can be implemented using several classes of soft ionic media, including water-based hydrogels, ionic-liquid-based ionogels, and ionically conductive elastomers. The ionic medium used in this thesis is best classified as a water-based ionically conductive hydrogel rather than an ionogel: the devices use a PVA/H_3PO_4/PVP gel in which water is the continuous solvent phase, whereas ionogels conventionally immobilize ionic liquids within a polymer or inorganic network. These material classes offer different trade-offs for iontronic sensing. Hydrogels are soft, inexpensive, and readily processed from aqueous formulations; ionogels usually improve solvent retention and environmental stability by replacing water with ionic-liquid-based media; and ionically conductive elastomers can further reduce leakage concerns but typically require more specialized chemistries and fabrication workflows [60, 61, 62, 63, 64].

For the present thesis, a PVA/H_3PO_4-based hydrogel was selected as the demonstrator ionic medium because the core PVA/H_3PO_4 system is already well established in iontronic pressure-sensor literature and has repeatedly been used in geometry-controlled devices in

Material class	Advantages	Limitations	Fit for this thesis
Hydrogels	Soft, high ionic conductivity, water-based processing, low material cost	Dehydration, leakage, environmental drift unless sealed	Strong fit for rapid prototyping and framework testing
Ionogels	Better humidity tolerance, high stability, printable in some systems	Ionic-liquid cost, more complex synthesis and processing	Useful, but higher process overhead than needed here
Ion-conducting elastomers	Better mechanical robustness and packaging stability	More specialized chemistry and slower iteration	Attractive long-term, but not the fastest route for this study

Table 2.5: Practical comparison of iontronic material classes for the present design problem. The key selection criterion was compatibility with a fast geometry-design-to-fabrication loop, rather than maximizing material novelty.

which pressure response is governed by changes in interfacial contact area [65, 66]. The same gel-electrolyte family has also been described as readily available and inexpensive for pressure-sensing applications [67]. These features made it well matched to the objective of this work: to study a reusable geometry-design framework using a material system that could be fabricated repeatedly and economically during rapid design iteration. The small PVP addition used here was introduced to improve rheology and film handling during fabrication; the literature precedent claimed in this thesis is the core PVA/H_3PO_4 iontronic system rather than the exact three-component formulation.

This choice was a practical one rather than a claim that hydrogels are universally superior iontronic materials. The main limitation of the selected hydrogel is environmental sensitivity: water loss can alter stiffness, ionic transport, and baseline response unless the device is well encapsulated. Ionogels can reduce evaporation-related limitations, and high-performance iontronic pressure sensors have been demonstrated using alternative ionic-liquid-based systems such as PVDF-HFP/[EMI][TFSI] or more elaborate multicomponent ionogel formulations [68, 69]. However, these routes introduce different raw materials, ionic-liquid cost, and additional synthesis complexity; broader ionic-gel literature has likewise identified cost and toxicity as recurring limitations of conventional ionogel systems [70]. Ionically conductive elastomers are also attractive for improved long-term stability, but recent demonstrations rely on distinct chemistries and manufacturing routes rather than a direct substitution into a water-based gel process [64]. Because the main contribution of this thesis is geometry-driven sensor design rather than ionic-material invention, the

lower-cost PVA/H_3PO_4 hydrogel provided the most appropriate material choice for the present framework study.

Three H_3PO_4 concentrations were screened using comparative dielectric/frequency characterization together with practical handling observations, and the intermediate concentration was selected for the main devices. The lowest concentration produced a weaker device-level response, while the highest concentration was less convenient to handle during assembly; the middle formulation provided the best practical balance for the subsequent framework-driven design iterations. The device-specific stack architecture that builds on this material choice — including electrode coatings, conductive fabric, and TPU encapsulation — is described in Chapter 3 (Section 3.5).

2.4 Finite Element Workflows

To ensure the reproducibility of the computational studies mapped in later chapters, all finite-element simulations were executed in a fixed software and hardware environment (Table 2.6). All DolfinX finite-element simulations were executed on an Apple MacBook Pro with an M4 Pro chip (14-core CPU, 20-core GPU, 24 GB unified memory) running macOS. All bespoke scripting, surrogate modeling, geometry generation, and post-processing were implemented in Python together with a small set of standard scientific-computing libraries. The main software components used in the computational workflow are summarized in Table 2.6.

2.4.1 Early Exploratory Modeling in COMSOL

For the bending sensor, we used COMSOL Multiphysics (Solid Mechanics module). COMSOL was initially selected for its ease of setting up multiphysics couplings (if needed) and its built-in support for large-deformation hyperelasticity and contact.

The basic simulation setup involves:

- **Geometry:** Import of the 3D CAD model of the bending sensor.
- **Material:** Assignment of the hyperelastic parameters fitted in Section 2.2.
- **Physics:** Application of a prescribed displacement or rotation to one end of the sensor while the other is fixed, mimicking finger-joint flexion.

- **Outputs:** Extraction of the reaction force and the distribution of Green–Lagrange strain to correlate with the expected capacitance change of the bending sensor.

COMSOL was used primarily in the early stage of this work for exploratory modeling and qualitative inspection of the deformation patterns in the soft sensor geometries. However, the pressure-sensor study quickly developed into a large-deformation contact problem requiring repeated simulations across many geometry variants. In that setting, it became more important to inspect the formulation, contact terms, and solver behavior directly and to trace the source of numerical differences between runs.

During preliminary compression simulations of the silicone structures—for example, the cylindrical compression cases associated with the Yeoh fits in Section 2.2—we observed contact-instability behavior and mesh-penetration artefacts at higher compressive strains, even after mesh refinement and contact-setting adjustments. Because the pressure-sensor and bending-sensor studies needed direct control over the weak form, contact treatment, and numerical settings, we migrated those quantitative studies to an open-source FEniCSx/DolfinX implementation (Section 2.4.2). In the final thesis workflow, COMSOL therefore serves mainly as an exploratory and qualitative tool for early prototyping, while DolfinX is the primary platform for the production pressure-sensor simulations and for targeted bending studies that benefit from the same scripted pipeline.

2.4.2 DolfinX-Based Parameter Sweeps

FEniCSx (DolfinX) became the scripted finite-element environment used in this thesis whenever the sensing problem required transparent control over geometry generation, weak forms, load stepping, and batch data export. While COMSOL remained useful for early exploratory bending-sensor modeling, the later design studies relied on DolfinX for two related tasks: (i) 3D compression/contact simulations for the pressure-sensor microstructures, and (ii) 2D/3D rotation-driven analyses of pillar-based bending and capacitive structures, including gravity-sag correction. In both branches, the goal was to produce consistent, scriptable mechanical response data that could be reused across the design studies in Chapters 3 and 4.

Shared computational backbone

Across both pressure and bending studies, geometry was generated parametrically in Python and meshed through Gmsh/`pygmsh`, then exported to XDMF/HDF5 for use in

Table 2.6: Main software libraries used in the computational workflow of this thesis.

Component	**Version**	**Role in this thesis**
Python	3.10.19	Interpreter for all modeling, optimization, post-processing, and plotting scripts.
DolfinX / UFL / Basix	0.10.0 / 2025.2.0 / 0.10.0	Finite-element assembly and solution of the hyperelastic/contact models, including weak forms and mixed finite-element spaces.
PETSc4py / mpi4py	3.24.1 / 4.1.1	Nonlinear solve infrastructure, sparse linear algebra, and parallel reduction of global quantities.
Gmsh / meshio / h5py	4.15.0 / 5.3.5 / 3.14.0	Parametric mesh generation and mesh/result-file I/O for DolfinX-compatible workflows.
NumPy / SciPy / pandas	2.2.6 / 1.15.3 / 2.3.3	Numerical processing, interpolation, smoothing, and assembly of simulation datasets.
scikit-learn / scikit-optimize / pymoo / joblib	1.7.2 / 0.10.2 / 0.6.1.5 / 1.5.2	Surrogate-model training, optimization baselines, and serialization of trained models.
Matplotlib / PyVista	3.10.8 / 0.46.4	Figure generation and 3D visualization of deformed meshes and simulation outputs.
Blender	4.3	Headless export of optimized layouts to STL files for DLP 3D printing.

DolfinX. The constituent silicone was represented using the Yeoh hyperelastic law fitted from the compression data in Section 2.2, with region-wise material assignment when softer electrode layers had to be represented explicitly. Nonlinear equilibrium was solved incrementally with Newton iterations, and each run wrote compact CSV summaries containing the deformation history and derived quantities needed for later post-processing. This scriptable workflow was essential because the downstream task was not simply "run FEM," but "sweep many geometries and compare them consistently," producing the mechanical response data on which the later design studies are built.

The common backbone shown in Figure 2.2 is therefore best understood as a data pipeline. The FE model provides force, deformation, contact, gap, or cavity-collapse histories at each load step; those histories are then reused differently in the two sensor branches. For the pressure sensor, they provide the mechanical response data on which the design framework of Chapter 3 is built. For the bending studies, they become cavity-area or

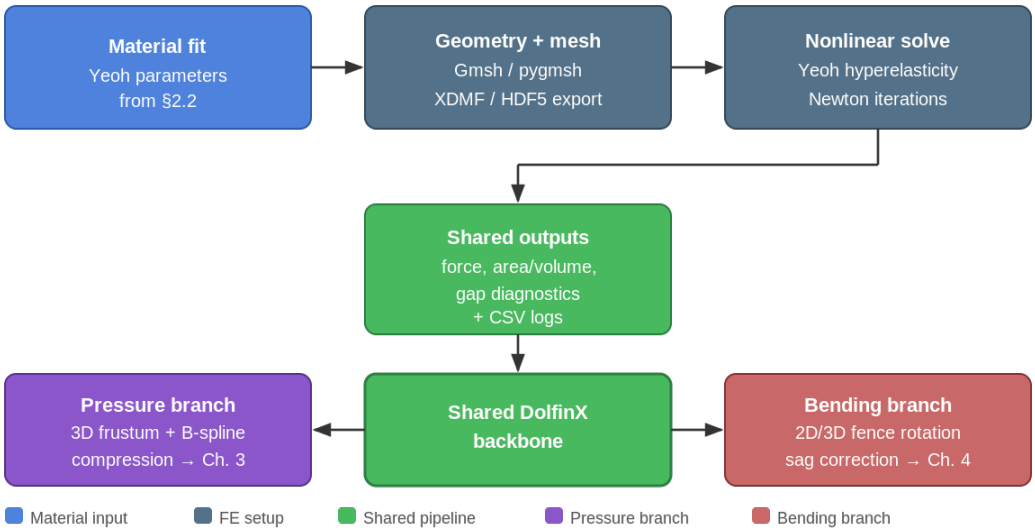


Figure 2.2: Schematic of the DolfinX workflow. Material calibration, parametric meshing, and nonlinear FE solves produce mechanical response histories. These feed either the pressure-sensor branch (3D compression/contact) or the bending branch (cavity collapse and sag correction).

cavity-volume histories that are translated into capacitance-angle trends and sag-corrected design comparisons. Detailed verification and validation are deferred to Section 2.5; the present section focuses on how the DolfinX models were structured.

Pressure-sensor branch: 3D frustum and B-spline microstructures

The initial DolfinX pressure-sensor model used a truncated-cone (frustum) microstructure parameterized by bottom radius r_b, top radius r_t, and height h. Although this geometry is simple, we treated it as a full 3D solid rather than an axisymmetric reduction, discretizing the domain with quadratic tetrahedral elements. This full 3D treatment was selected because the later extension to B-spline/superellipse microstructures was explicitly non-axisymmetric and we wanted one consistent meshing and solver infrastructure across the pressure-sensor design family. Each candidate geometry was bonded to a rigid base and compressed by a rigid platen, with local mesh refinement concentrated near the top contact region and other high-strain zones. The early frustum sweeps varied height and top radius while keeping the bottom footprint matched to the printable base pattern.

The hyperelastic response was solved in a total-Lagrangian setting using the Yeoh strain-energy density

$$W(I_1) = C_{10}(I_1 - 3) + C_{20}(I_1 - 3)^2 + C_{30}(I_1 - 3)^3, \tag{2.3}$$

with near-incompressibility enforced through a mixed displacement–pressure formulation, so that the displacement and pressure fields were solved simultaneously. For the pressure-sensor compression studies, frictionless contact with the rigid platen was imposed in a total-Lagrangian weak form using a Nitsche-type penalty stabilization [71, 72]. A frictionless interface was assumed to simplify the contact formulation during automated geometry sweeps, as the simulated structural response is governed primarily by vertical buckling and cavity volume change rather than lateral slip gradients. The effective contact stiffness scaled with γ/h, where h is the local mesh size, so that non-penetration could be enforced while maintaining numerical stability across different meshes and geometries. This adaptive penalty scaling was used for contact stabilization only; it was not the mechanism used to enforce incompressibility. At each prescribed displacement step δ, the solver recorded reaction force $F(\delta)$, contact area $A(\delta)$, convergence flags, and gap diagnostics. These run-level outputs were then aggregated into summary tables and exported as CSV files for downstream analysis.

The pressure-sensor branch was applied to two geometry families: frustum microstructures (parameterized by height and top radius) and B-spline/superellipse lofts (parameterized by an 8-dimensional shape vector plus height). Both families were evaluated under 3D indentation using the same solver infrastructure and contact formulation described above. The frustum family used a full (non-quarter) model, while the B-spline family used a quarter-symmetry model to manage computational cost at higher mesh resolution. In both cases, the solver produced per-step force, contact-area, and gap histories. The design automation layer built on these mechanical outputs—including surrogate modeling, mechanism-specific transduction models, and array-level optimization—is presented in Chapter 3.

Bending branch: pillar models, sag correction, and 2D/3D hierarchy

DolfinX was also used for targeted bending-sensor studies built around a pillar-based cross-section with alternating silicone pillars and air cavities between compliant electrode layers. Here the main goal was different from the pressure branch: instead of optimizing contact area under normal indentation, we wanted to understand how bending-driven cavity collapse and electrode sag reshape the capacitance-angle response. To keep broad geometry sweeps affordable, the primary model was a 2D plane-strain cross-section with

spatially varying material regions for the bulk silicone and softened electrode layers. Near-incompressibility was again represented using a mixed displacement–pressure formulation, implemented in the bending branch as a Taylor–Hood P_2/P_1 element pair.

In these bending simulations, the rotating edge was driven using a rigid-connector kinematic relation of the form

$$u(X) = c + \big(R(\theta) - I\big)(X - X_c), \tag{2.4}$$

where X_c is the centroid of the driven edge, $R(\theta)$ is the prescribed rotation, and c is a small set of global translation degrees of freedom introduced through a `Real` element. This construction was used in both 2D and selected 3D pillar models because it reproduces a prescribed rotation while allowing the boundary to translate consistently under large deformation. Parameter sweeps were then carried out over cavity width d and core height h, with outputs written as cavity-area or cavity-volume histories over rotation angle.

A key output of the bending branch was the sag-correction model, which accounts for gravity-induced electrode deflection into the cavities before any applied bending. The derivation, schematic, and design implications of this correction are presented in full in Chapter 4 (Section 4.3.2).

The bending branch was organized as a model hierarchy rather than a single monolithic sweep. Broad design exploration and sag sensitivity analysis were carried out in 2D, because that format made it practical to scan many (d, h) combinations and to perform mesh studies on representative cases. Selected 3D runs were then used as cross-checks on representative geometries and to study the influence of electrode thickness and soft-electrode behavior on cavity-volume evolution. In this sense, the 2D models were the main design workhorse, while the 3D models acted as confirmation that the dominant trends were not artifacts of the plane-strain simplification. The resulting cavity-collapse histories were finally translated into capacitance-angle predictions using analytical post-processing, allowing the bending-sensor simulations to inform Chapter 4 without requiring a prohibitively expensive full 3D sweep for every candidate design.

2.4.3 Surrogate Modeling and Optimizer Implementation

Section 2.1 motivates surrogate-assisted design for expensive FEM-driven search spaces; this subsection records the implementation choices that underpin the design automation layer. Although the surrogate and optimizer infrastructure described here was developed as a shared capability, its primary application in this thesis is in the pressure-sensor design framework of Chapter 3, where it enables array-level optimization across frustum

and B-spline geometry families. The bending-sensor study of Chapter 4 uses the same DolfinX mechanics backbone for parametric sweeps but does not require surrogate-based optimization because its design space is low-dimensional enough for direct exploration. The detailed sensor-specific surrogate results and comparisons are presented in Chapter 3 (Section 3.4.4).

FEM outputs (force, contact area, gap, and cavity-volume histories) were assembled into tabular datasets with one row per geometry–load-step combination. Surrogate models were trained on these datasets to approximate the mapping from geometry descriptors and compressive displacement to the mechanics quantities of interest. For the frustum-family pressure sensor, where the parameter space is low-dimensional and well-covered by structured sweeps, a Gaussian process (GP) regressor was used; GP uncertainty estimates were also used to guide targeted re-sampling in poorly covered regions. For the B-spline family, where the design space is higher-dimensional, a random forest (RF) regressor was used instead, as RF generalizes more reliably without the $\mathcal{O}(n^3)$ training cost that makes GP inference expensive in larger datasets. Both GP and RF models were implemented using `scikit-learn` (version 1.7.2; Table 2.6).

Array-level optimization was performed using differential evolution (DE) as the default search algorithm. DE was selected over Bayesian optimization because the decoded array design introduces discontinuities, flat linearity plateaus, and hard infeasibility penalties that make the objective landscape ill-suited to the smooth response-surface assumptions underlying standard GP-based acquisition functions. DE population size was set to $15 \times d$ where d is the number of continuous design variables, with mutation factor $F = 0.8$ and crossover probability $C_r = 0.9$; convergence was declared when the relative change in the population's best objective fell below 10^{-5} over 100 consecutive generations. Justification for preferring DE over Bayesian optimization on these specific landscapes, including representative convergence comparisons, is given in Section 3.6.5.

2.5 Computational Model Verification

Computational models were verified via mesh convergence studies tracking key quantities of interest. Because the pressure-sensor simulations involve large-deformation hyperelasticity together with contact, we did not treat small-strain analytical contact solutions as a quantitative reference. Instead, the verification emphasis was placed on demonstrating that the numerical discretization error remained acceptably small for the production meshes used in the design study. Experimental validation — comparing model-predicted sensor response against measured capacitance data — is performed in the context of each sensor

design and reported in Chapters 3 and 4, where measured and simulated C/C_0 curves are compared directly under matched loading conditions.

2.5.1 Mesh Convergence Study

A systematic mesh convergence study was conducted for each representative geometry used in the DolfinX pressure-sensor simulations. Starting from a coarse baseline mesh, we applied successive global refinements by halving the characteristic element size h_e in each iteration, producing a sequence of meshes with approximately $1\times$, $4\times$, $16\times$, and $64\times$ as many elements as the baseline. For each mesh, we monitored three quantities of interest (QoIs) at a fixed indentation depth corresponding to $\varepsilon = 0.3$:

1. **Reaction force** F on the rigid platen, the primary mechanical output for calibration.
2. **Contact area** A, computed by integrating the contact indicator over the top surface.
3. **Peak von Mises equivalent strain** in the frustum sidewall, a diagnostic for local stress concentration.

Convergence was assessed using the Richardson extrapolation procedure. Denoting the QoI computed on mesh i as Q_i, we estimated the asymptotic value Q_∞ by fitting the relation $Q_i = Q_\infty + Ch_e^p$, where p is the observed order of convergence and C is a constant. The mesh was deemed sufficiently refined when the relative discretization error $|Q_i - Q_\infty|/|Q_\infty|$ fell below a prescribed threshold τ for all three QoIs. In this work we adopted $\tau = 2\%$ as an acceptable error level for simulation-based design. The final production meshes satisfy this criterion while remaining computationally tractable for the parametric sweeps described in Section 2.4.2. For the representative production mesh used in the final design study, the Richardson-estimated discretization error was below this threshold, confirming that the selected mesh density was adequate for the reported force, contact-area, and strain trends.

Figure 2.3 summarizes the two main numerical checks used for the pressure-sensor contact formulation. The mesh study in panels (a)–(b) shows that force is comparatively insensitive to refinement once the mesh is sufficiently resolved, while contact area requires finer surface discretization because it depends directly on the evolving contact boundary. The penalty study in panels (c)–(d) complements this by showing that the adaptive contact stabilization must be large enough to prevent artificial compliance at the interface, but that the solution becomes effectively insensitive to further increases once the penalty enters a stable regime. Together, these checks support the use of the selected production meshes and adaptive penalty settings in the later surrogate-generation and design studies.

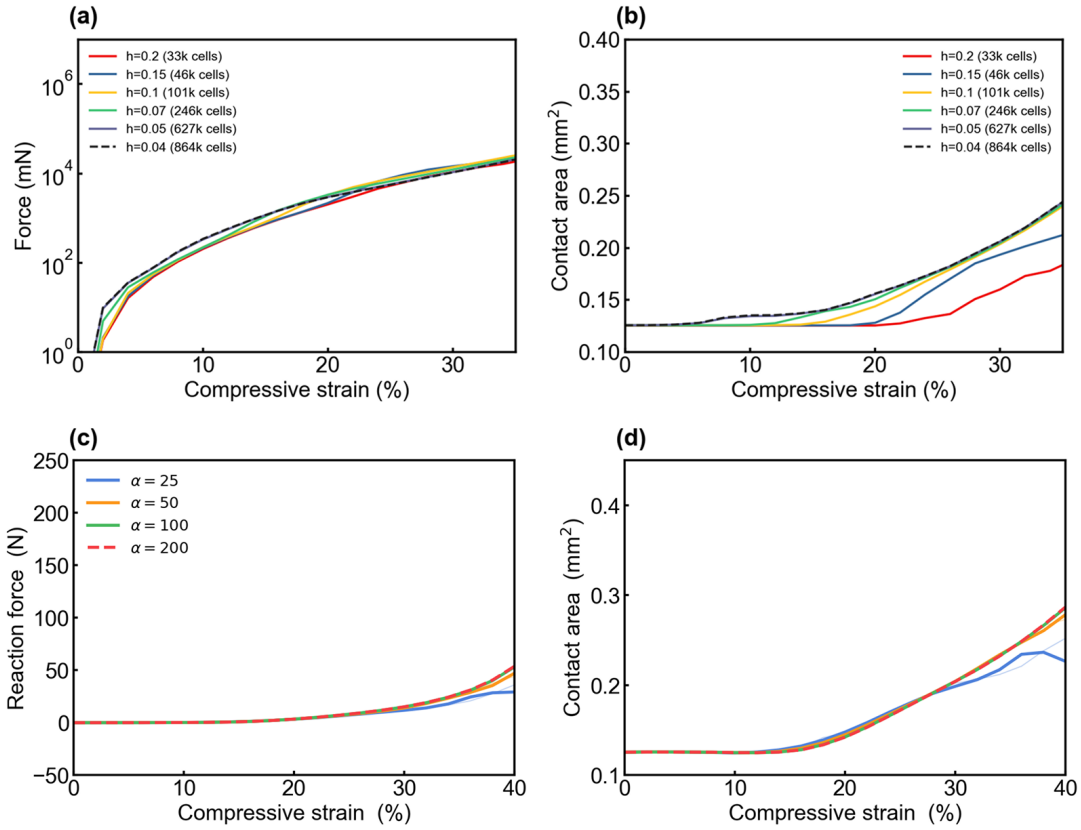


Figure 2.3: Numerical sensitivity checks for the DolfinX pressure-sensor contact simulations. (a–b) Mesh size effect on force and contact area. (c–d) Sensitivity to contact-penalty scaling. Force converges quickly under refinement; contact area is more sensitive to discretization. Moderate-to-large penalty factors produce nearly identical trends.

An analogous mesh convergence study was performed for the bending-branch 2D plane-strain models, monitoring cavity-area history and reaction moment as quantities of interest at $\theta = 100°$. The Richardson-estimated discretization error for the production bending mesh fell below the same 2% threshold adopted for the pressure branch, confirming that the selected mesh density is adequate for the cavity-collapse trends reported in Chapter 4.

2.6 Summary

This chapter has established the shared tools and protocols that underpin the rest of the thesis. Hyperelastic testing and fitting provided the material basis for the 3D-printable silicone, while the DolfinX framework provided a scriptable, numerically verified solver infrastructure capable of handling large-deformation contact and cavity collapse. Mesh convergence and penalty-sensitivity studies confirm that the production meshes produce discretization errors below 2% for the key quantities of interest. Likewise, the generalized capacitive measurement setups ensure a consistent basis for prototype evaluation. With the material properties characterized, solver infrastructure established, and evaluation requirements defined, the subsequent chapters apply this framework to the design, optimization, and experimental characterization of the microstructured pressure sensors (Chapter 3) and angle-centric bending sensors (Chapter 4).

Chapter 3

Design of Flexible Pressure Sensors

Building on Gaps 1 and 2 identified in Chapter 1 (Section 1.3), this chapter develops a reusable, range-aware design framework for multi-tier pressure-sensor arrays and applies it to iontronic and conventional capacitive mechanisms. The framework separates nonlinear contact mechanics from mechanism-specific transduction physics and treats linearity as an explicit design objective alongside sensitivity.

Three sensing routes are explored in a deliberate sequence that reflects the design trade-offs encountered during the project. The microwave resonator (Section 3.3) was investigated first as a deliberate exploration of passive wireless sensing rather than as an unrelated side study. Flexible RFID sensing tags, passive wireless pressure sensors for pressure-garment monitoring, and wearable or soft wireless sensing elements had already shown that remote interrogation could reduce wiring burdens in deformable systems [73, 74, 75, 76]. This made it reasonable to ask whether a coupled microwave tag–reader architecture could provide useful pressure sensing for the intended glove while relocating readout electronics away from continuously deforming regions. However, the final glove required many distributed sensing nodes rather than one isolated element. Scaling the RF route to that architecture would have required a dedicated multichannel RF interrogation and readout-system effort, while the prototype also exposed alignment-sensitive cross-sensitivity under bending: the resonant response depends on tag–reader spacing and orientation, so natural hand motion generates electromagnetic artefacts that are difficult to separate from the intended pressure signal, and the overall RF stack is bulkier and more packaging-sensitive than a local transducer embedded directly in the glove. Those limitations motivated the pivot to soft, local-readout capacitive architectures.

Within the capacitive family, two routes are developed for complementary reasons. The

iontronic EDL sensor (Section 3.5) is the primary high-performance route: charge separation at ionic conductor–electrode interfaces over a nanometre-scale Debye layer yields interfacial capacitances orders of magnitude larger than bulk dielectrics [60], enabling high sensitivity across the sub-kPa to tens-of-kPa range relevant to glove contact monitoring and strong linearity when interface geometry is designed appropriately [65, 68, 77]. However, iontronic materials require controlled synthesis, humidity management, and encapsulation protocols that are not universally accessible to all research groups [78, 62, 61]. The conventional capacitive sensor (Section 3.6) addresses this limitation directly: it uses a commodity 3D-printable silicone dielectric and off-the-shelf conductive fabric, both available from standard suppliers with no specialized chemistry or processing. The purpose of this second route is not to match iontronic sensitivity, but to demonstrate that the same design framework extracts the best achievable linearity and range from accessible materials, making the pipeline transferable beyond the specific ionic material system used here.

Section 3.1 reviews pressure sensing technologies and microstructure strategies, situating the chapter's design choices within the broader flexible-sensor literature and placing the three routes in the context of existing approaches. Section 3.2 establishes the design requirements, arguing that linearity deserves equal weight to sensitivity in wearable contexts where baseline variability and calibration burden are first-order concerns. Section 3.3 presents the first sensing route explored—a microwave resonator—and the lessons that motivated a shift to soft capacitive architectures with local readout. Section 3.4 presents the central methodological contribution: a reusable design framework that separates nonlinear mechanics from mechanism-specific transduction and enables range-tunable, multi-tier array optimization. Sections 3.5 and 3.6 apply this framework to two soft capacitive mechanisms—iontronic EDL and conventional capacitive—demonstrating that the same pipeline produces useful, manufacturable sensors across different materials and performance envelopes.

3.1 Pressure Sensing Technologies

Pressure (tactile) sensing is essential for OTG hand monitoring because contact events encode grasp intent, interaction forces, and functional task execution. Flexible pressure sensors can be broadly categorized by transduction mechanism, including piezoresistive, capacitive, piezoelectric/triboelectric, and iontronic approaches [79, 80, 81, 82]. These mechanisms offer different trade-offs in sensitivity, dynamic range, stability, manufacturability, and readout complexity for glove-scale integration [83]. Figure 3.1 summarizes these primary transduction physics and provides the basis for the mechanism selection developed

in this chapter.

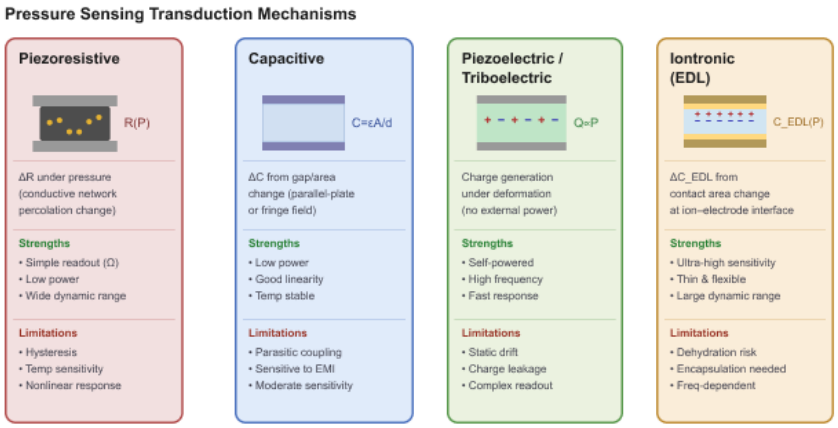


Figure 3.1: Visual taxonomy of the primary flexible pressure-sensing mechanisms: piezoresistive, capacitive, iontronic, and triboelectric/piezoelectric.

Piezoresistive sensors exploit the change in electrical resistance under compression of a conductive network. Their main advantages are simple readout electronics and relatively straightforward fabrication using printed conductors or conductive composites. However, their performance in OTG use is limited by hysteresis in viscoelastic matrices, drift under repeated cycling, and sensitivity to microcrack evolution or network rearrangement during wear [84]. These instabilities are difficult to manage in a glove context where cyclic loading and donning variability are unavoidable, which motivates looking beyond piezoresistive solutions for the primary sensing modality.

Piezoelectric and triboelectric sensors generate electrical output from dynamic mechanical input rather than from quasi-static deformation. They are attractive for self-powered sensing and transient contact detection, but are fundamentally unsuited to sustained static pressure measurement [83], which is required for monitoring grasp forces held over several seconds or minutes. These mechanisms are therefore not pursued further here.

Capacitive pressure sensors measure capacitance changes produced by compression of a dielectric layer between electrodes. Compared with piezoresistive designs, capacitive sensors offer better repeatability and lower steady-state power consumption, making them especially attractive for wearable systems. Their performance is governed by dielectric compressibility, electrode geometry, and array interconnect architecture, and critically, all of these are accessible to model-guided optimization [85, 86]. These characteristics,

together with the compatibility of solid silicone dielectrics with 3D-printable fabrication, make capacitive architectures well suited to the design framework developed in this chapter.

Iontronic sensors exploit the electrical double layer (EDL) formed at ionic conductor–electrode interfaces, where charge separation occurs over a nanometre-scale Debye layer rather than across a bulk dielectric. The resulting interfacial areal capacitance can be orders of magnitude larger than that of a conventional dielectric of the same footprint, enabling reported sensitivities in the range of 10^2–10^4 kPa^{-1} in recent studies [65, 68, 77]. For a glove application where detecting sub-kPa incipient contact is as important as monitoring grasp forces in the tens-of-kPa range, that intrinsic gain advantage is the primary reason for pursuing iontronic sensing alongside the conventional capacitive route. The main engineering challenge is packaging: iontronic performance can be affected by hysteresis, ionic migration, interfacial drift, and hydrogel dehydration under extended wear [78, 62], and these effects must be managed through geometry design and encapsulation rather than by relying on the ionic medium alone.

3.1.1 Rationale for Selecting Capacitive Sensing

The intended glove application requires measurement of both transient contact and sustained grasp pressure, which makes quasi-static sensing essential. Piezoelectric and triboelectric approaches are attractive for dynamic events and self-powered operation, but sustained quasi-static measurement is difficult because piezoelectric readout is affected by charge leakage under long-duration loading [87, 88]. Piezoresistive sensors are widely used in wearable systems because of their simple readout and high sensitivity, but their response is more vulnerable to time-dependent hysteresis, creep-related drift, and temperature-dependent output variation [89, 90]. Capacitive sensing therefore offered a more suitable starting point for the present application because it supports sustained pressure measurement while being associated with lower drift, better temperature behavior, and low steady-state power consumption than common piezoresistive alternatives [91, 92].

As the work progressed, capacitive sensing revealed a second advantage that was not the original basis for its selection but became important methodologically: its electrical response is strongly governed by mechanically interpretable quantities such as effective contact area, dielectric separation, and the progression of structural engagement under load. These quantities can be obtained from nonlinear finite-element simulations and then passed into reduced-order transduction models. The simulation-driven framework developed in this thesis therefore emerged from the need to design capacitive sensors more systematically, rather than capacitive sensing being chosen merely to fit a pre-existing framework.

Iontronic sensing was subsequently introduced as a related high-sensitivity capacitance-based route, preserving the same central dependence on geometry-driven contact evolution while extending attainable signal gain through electric-double-layer transduction.

3.1.2 Role of Microstructure in Sensor Performance

Across the capacitive and iontronic mechanisms selected above, microstructure geometry is the dominant design lever. Features such as pyramids, domes, cones, and porous lattices modify effective stiffness, contact-area growth, and electric-field evolution under compression, governing sensitivity, linear range, hysteresis, and noise floor [15, 16]. Figure 3.2 illustrates how common prior-art geometries deform under load. In much of the existing literature, microstructure selection is treated empirically: a small number of candidate shapes are compared by fabrication and test, making it difficult to target task-specific performance envelopes or to retarget a design when the operating range changes [17, 19].

This chapter adopts a *frustum array* as the primary geometry family for both the iontronic and capacitive sensors. A frustum — a truncated cone — offers a flat contact surface that engages the opposing electrode progressively as pressure increases, producing a controlled monotonic area trajectory that is amenable to FEM-based analysis and surrogate-assisted optimization. Compared with sharp pyramids, which can maximize low-load sensitivity but saturate abruptly and are harder to print reliably, frustums offer a better balance between tunable contact mechanics, fabrication repeatability, and compatibility with direct 3D printing in silicone. The frustum family is also low-dimensional enough for structured parameter sweeps, yet rich enough — through height, top radius, and base radius — to cover a wide range of stiffness and contact-onset behaviors.

A closely related limitation in the literature is the gap between single-cell performance and array-level deployability. Much of the literature reports sensitivity and hysteresis for isolated test cells under idealized loading, whereas glove integration requires multiple taxels operating on curved, deforming surfaces with stable, cross-talk-free interpretation [93, 85, 86]. Broad-range, approximately linear response requires *progressive engagement*: graded or hierarchical microstructures that bring additional contact area or stiffness modes into play as load increases, so that the composite array response remains useful across the full operating window [28, 65, 20].

Across both iontronic and conventional capacitive mechanisms, this quickly becomes an array-level problem rather than a single-cell one. The resulting sensitivity–linearity trade-off and its implications for framework-based optimization are developed more explicitly in Section 3.2.

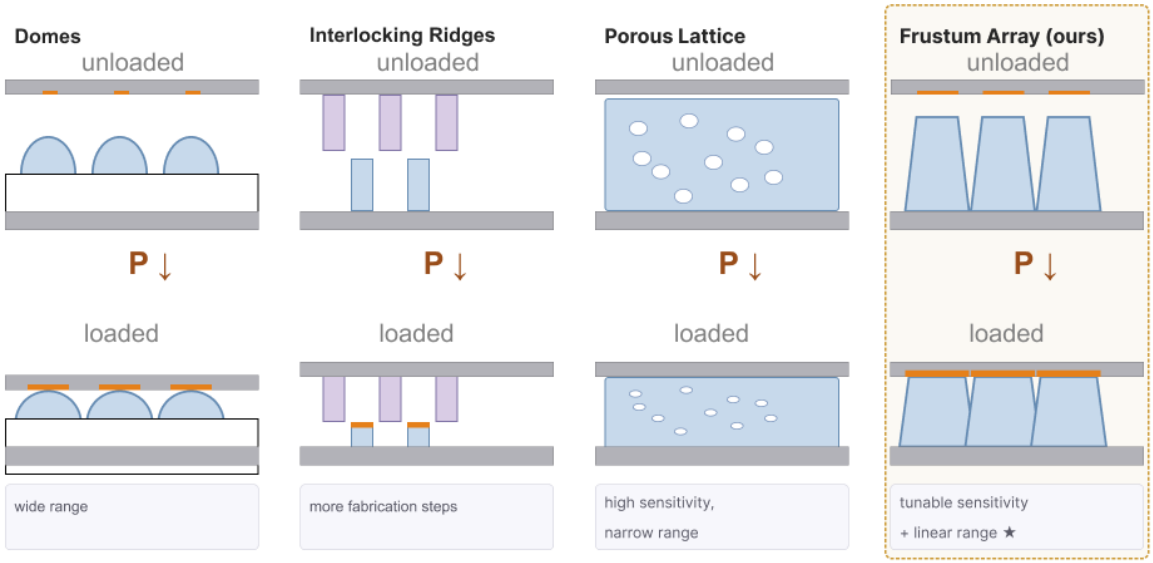


Figure 3.2: Comparison of common microstructure geometries under compressive load. Domes exhibit high nonlinearity; interlocking ridges require complex fabrication; porous lattices offer narrow-range sensitivity. The frustum array provides tunable, progressive engagement for both high sensitivity and extended linear range.

This chapter examines three sensing routes. The microwave resonator (Section 3.3) was pursued first, but its cross-sensitivity and benchtop-oriented interrogation made it unsuitable for glove deployment. The iontronic sensor (Section 3.5) became the primary pressure-sensing route because the EDL mechanism provides the largest signal gain under glove-relevant loads. The capacitive sensor (Section 3.6) is retained as a second application of the same framework, showing that the design workflow also produces near-linear sensors from simple solid-state materials.

3.2 Sensor Design Requirements

The pressure sensors developed in this chapter target wearable and soft-robotic applications where sensing elements must operate inside thin, curved, and repeatedly deforming substrates [23, 35, 37]. While many of the resulting requirements—mechanical compliance, low drift, manufacturability—apply broadly to any flexible pressure sensor, the data glove is adopted here as a particularly demanding integration case. Glove-mounted sensors must survive finger-scale curvature, cyclic bending at every joint, shear from object manipulation, and environmental exposure (sweat, humidity, abrasion), all within a stack thin enough not to impair tactile perception or restrict joint range of motion. Any sensor architecture that satisfies these constraints is also likely to be viable in less demanding wearable or soft-robotic settings.

3.2.1 Operating Range and Sensitivity

The primary operating envelope spans light touch (sub-kPa) through firm grasp (tens of kPa) [94, 35, 37]. Within this range, the sensor should produce a monotonic, sufficiently large capacitance change to be resolved by compact readout electronics. Sensitivity is the most commonly reported headline metric in the flexible-sensor literature, and high low-load sensitivity is indeed valuable for detecting incipient contact and fine manipulation forces [23, 36, 24].

However, sensitivity alone is an incomplete design target. A sensor that is extremely sensitive at low loads but saturates within a few kPa is of limited use for monitoring grasp forces that span a broader range. Conversely, a sensor with moderate but sustained sensitivity across the full operating window is far more useful in practice, even if its peak sensitivity figure is less impressive. The distinction between peak sensitivity and sustained, range-wide performance is central to the design philosophy of this chapter.

3.2.2 Linearity and Calibration Burden

Most flexible pressure sensor studies optimize for sensitivity and report linearity only as a secondary metric, if at all [23, 24, 25, 26]. In practice, linearity is at least as important as sensitivity for three reasons that become acute in wearable deployment.

Baseline variability under real wearing conditions. When a sensor is mounted on a conformable substrate such as a glove, the resting capacitance C_0 is not a fixed constant. It

depends on the local curvature, the fit tightness, how far the glove is pulled onto the finger, and the mechanical pre-load imposed by the textile. A tight fit pre-compresses the sensor slightly, raising C_0; a loose fit leaves it closer to the unloaded baseline. Different users, or even the same user on different donning sessions, will therefore start from a different C_0 [27, 95].

For a *nonlinear* sensor, the local slope (sensitivity) depends on where along the response curve the baseline sits. A shift in C_0 due to fit variability therefore changes not only the offset but also the effective gain, making the sensor's interpretation pressure-dependent in a way that couples to the wearing condition. For a *linear* sensor, the slope is constant regardless of baseline. A fit-induced shift in C_0 changes only the offset, which can be corrected by a simple re-zeroing without affecting the pressure-to-capacitance gain. In a wearable context where re-calibration should be minimal, this difference is significant.

Calibration burden. A nonlinear sensor requires a dense, multi-point calibration curve, and that curve may need to be re-acquired whenever the wearing condition changes. A linear sensor requires only two calibration parameters, and if the offset shifts due to donning variability, only a single-point re-zeroing is needed. For clinical or daily-use deployment where the glove is donned and doffed repeatedly, a low calibration burden is a practical requirement, not a convenience [32, 6].

Sensitivity–linearity trade-off and multi-tier design. A single microstructure cell faces a fundamental trade-off. High sensitivity at low loads requires a compliant, easily deformable feature—a sharp tip, a tall slender pillar, or a thin membrane—that exhausts its deformation range quickly and saturates. Wide linear range requires the response to remain approximately constant-slope across the full operating window, which demands a more gradual, progressive engagement that inherently reduces peak low-load sensitivity [28, 65, 68].

This trade-off cannot be resolved within a single repeating cell at the sensitivity levels required for touch and grasp sensing. The multi-tier array architecture adopted in the design framework of Section 3.4 is a direct response to this constraint: by distributing the operating range across tiers with staggered engagement thresholds, the array achieves both high low-load sensitivity (from the first tiers to engage) and approximate linearity over the full target range (from the sequential handoff between tiers). In this chapter, linearity is treated as a design objective rather than only a reported performance metric, and it is this requirement that drives the array-level optimization framework.

3.2.3 Mechanical and Integration Constraints

Beyond the electrical response, the sensor must satisfy mechanical and environmental constraints imposed by wearable deployment [23, 35, 37]. The mechanical constraints are the most immediately restrictive: the active stack must be thin enough to conform to finger-scale curvature without creating pressure points or restricting joint range of motion, and it must survive cyclic bending at finger joints and shear from object manipulation without fatigue failure or progressive drift. These two requirements—thinness and durability—are in tension, since increasing substrate thickness generally improves durability but at the cost of conformality and tactile transparency. The design choices made in this chapter (frustum arrays on thin silicone substrates, serpentine or kirigami interconnects) are all downstream responses to this tension.

Integration imposes a second cluster of constraints. Sensing elements must be compact and locally readable so that multiple taxels can be distributed across the glove without centimetre-scale hardware or cross-talk between channels [85]. Readout electronics must be wearable in scale; benchtop-only instrumentation is unsuitable for the final platform. Environmental robustness is also required: the sensor should remain calibratable under sweat, humidity, and extended wear, and if drift or dehydration is unavoidable (as in the iontronic case), it must be manageable through encapsulation or periodic re-zeroing rather than by reliance on perfect environmental stability. Finally, materials and processes must be compatible with rapid design iteration and repeatable assembly at glove scale, which ruled out multi-step molding processes and custom-synthesised ionic media in favour of direct 3D-printable silicone and commercially available ionic gels.

These constraints, taken together, are why the chapter does not identify a single optimal sensing configuration but instead develops a design *framework*: the correct trade-off between sensitivity, linearity, durability, and manufacturability is application- and material-dependent, and a reusable pipeline that makes those trade-offs explicit is more useful than a fixed recipe.

3.2.4 Summary of Design Requirements

Table 3.1 consolidates the design axes used to evaluate the three sensing approaches studied in this chapter: a microwave resonator sensor, an iontronic electric-double-layer sensor, and a capacitive sensor with a silicone dielectric.

These requirements recur throughout the chapter as the basis for comparing the three sensing routes and for motivating the framework-level design choices developed alongside

Requirement	Design implication
Sensitivity	Sufficient capacitance change per unit pressure to be resolved by compact electronics across the target range (sub-kPa to tens of kPa).
Linearity	Approximately constant slope over the operating range, so that baseline shifts from fit variability affect only the offset and not the gain.
Mechanical integration	Thin, soft, conformal stack tolerant of finger-scale curvature, repeated bending, shear, and abrasion.
Arrayability	Compact local elements that can be distributed as multi-taxel arrays without centimetre-scale hardware.
Environmental stability	Calibratable under cyclic loading, humidity, and extended wear; manageable drift and hysteresis.
Manufacturability	Compatible with silicone/textile fabrication, 3D printing, and repeatable glove-scale assembly.

Table 3.1: Design requirements used to evaluate the pressure-sensing approaches in this chapter.

them.

3.3 Microwave Resonator Pressure Sensor

Portions of this section, including Figures 3.3–3.8, were previously published in [96] and are reproduced here for inclusion in this thesis.

3.3.1 Operating Principle

Microwave sensing was the first pressure-sensor direction explored in this thesis because it offers an attractive system-level promise: the mechanically active element can remain passive while the readout electronics are displaced to a more convenient location. That choice was consistent with an existing passive-wireless sensing direction: prior work had demonstrated flexible RFID-enabled sensing tags, inductively coupled wireless pressure sensing for pressure garments, wearable RFID compression sensing, and soft wireless tactile elements intended to reduce wiring demands in deformable systems [73, 74, 76, 75]. For a glove platform, that raised the question of whether a coupled resonant architecture could simultaneously encode (i) normal pressure through a resonance-frequency shift and (ii) bending through a coupling-dependent transmission-amplitude change. This direction was motivated by prior microwave sensors for pressure and strain [97, 98, 99], but most reported devices rely on rigid substrates or packaged RF structures that are difficult to integrate into thin, highly curved glove regions. Full fabrication and characterization details are reported in [96]; this section summarizes the operating principle and the lessons that motivated the subsequent shift toward soft local-readout architectures.

The microwave sensor uses a coupled *tag-and-reader* structure. The reader is connected to the RF instrument, whereas the tag is the mechanically active element placed above it. At first order, the resonant response follows

$$f_0 \approx \frac{1}{2\pi\sqrt{LC_{\text{eff}}}}, \tag{3.1}$$

where C_{eff} is the effective capacitance seen by the resonant structure. When pressure compresses the soft dielectric above the tag, the effective permittivity increases and C_{eff} rises, shifting the resonance to lower frequency. Bending changes the relative alignment and spacing between the tag and reader, perturbing the electromagnetic coupling and therefore the measured S_{21} notch depth. In other words, pressure is most naturally encoded in frequency, whereas bending introduces a stronger amplitude modulation. Figure 3.3 summarizes this two-channel sensing idea.

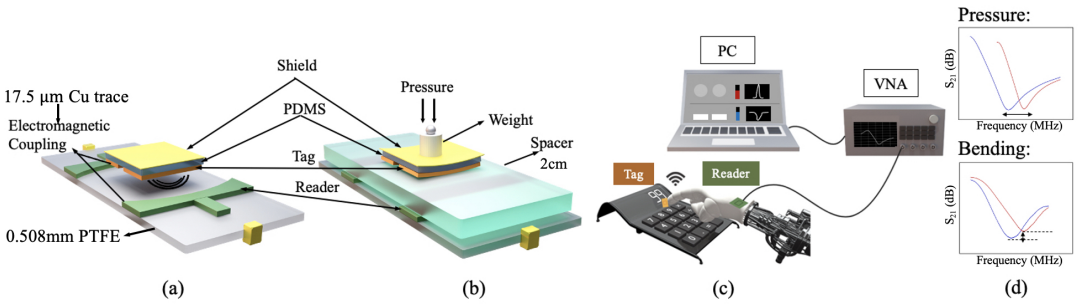


Figure 3.3: Microwave sensor concept and operating modes. (a) Exploded tag–reader architecture. (b) Pressure loading concept. (c) Example use scenario with passive tag and external reader/VNA. (d) Representative S_{21} response shifts. Reproduced from [96]. © 2023 IEEE.

3.3.2 Prototype Fabrication and RF Characterization Protocol

The microwave prototype was fabricated and tested as a proof-of-concept passive-wireless pressure-sensing route. The reader was patterned on a 0.508 mm PTFE substrate with 17.5 µm copper traces, while the passive tag was positioned above the reader and separated by the deformable PDMS dielectric layer. Four dielectric configurations were evaluated: 2, 4, and 6 mm solid PDMS layers, and a 6 mm porous PDMS layer fabricated using sugar-templated porosity. These variants allowed the RF response to be compared as a function of dielectric thickness and compressibility while keeping the tag–reader architecture fixed.

For pressure characterization, the tag–dielectric assembly was loaded in normal compression while the transmission response S_{21} was recorded across the resonant frequency band using a two-port vector network analyzer (S5065, Copper Mountain Technologies). The primary measured pressure observable was the resonant-frequency shift, extracted from the minimum of the S_{21} notch. Loading and unloading sweeps were used to assess repeatability and path dependence, with the same sensor measured for three repeats. For bending characterization, the relative curvature and alignment of the tag–reader pair were varied while monitoring both resonant frequency and notch amplitude, allowing pressure-dominant and bending-dominant response channels to be compared. The full fabrication details of the microwave prototype are reported in the associated publication [96]. This section documents the down-selection evidence that motivated the later shift to local capacitive readout.

Table 3.2 summarizes the microwave prototype method. The same two-column reporting template is used for all three sensing routes developed in this chapter (Tables 3.2, 3.5,

and 3.6) so that their fabrication and characterization parameters remain directly comparable. Lower-level RF sweep settings, detailed pressure-point scheduling, bending-fixture increments, and porous-PDMS recipe details are not expanded here because the microwave route serves as a down-selection prototype rather than the final pressure-sensor route.

3.3.3 Tag–Reader Structure and Equivalent Circuit

Figure 3.4 shows the physical layout and the equivalent-circuit representation used to interpret the response. The passive tag is a compact resonator placed above a planar reader; both were patterned in copper, with the reader realized on a 0.508 mm PTFE substrate using 17.5 μm copper traces. The tag footprint is approximately 45 $\times$ 20 mm, while the reader occupies approximately 95$\times$58 mm. To interpret the coupled response, we model the reader and tag as coupled resonant networks with lossy capacitive couplings, following prior microwave-resonator modeling approaches [100, 101, 102]. In this framework, pressure-induced changes in the dielectric layer modify an effective capacitance term in the tag network, shifting the resonance condition, whereas bending-induced changes in alignment and spacing modify the coupling terms and therefore the measured transmission amplitude.

3.3.4 Fabrication and Experimental Results

We selected polydimethylsiloxane (PDMS) as the deformable dielectric for this prototype because it is mechanically compliant, has a moderate dielectric constant, and is widely used in soft robotic and microfluidic fabrication. Both solid and porous PDMS layers were evaluated. The porous variant was fabricated using a sugar-template approach to introduce compressible air voids, thereby increasing the pressure-induced permittivity change [103, 104, 105]. This allowed us to compare two sensitivity-enhancement routes within the same RF platform: reducing the dielectric thickness (2, 4, and 6 mm solid PDMS) and increasing compressibility at fixed thickness (6 mm porous PDMS). The microwave tag was paired with a compact reader formed by gap-coupled microstrip lines, enabling a contactless measurement configuration without hard-wiring the deforming sensing layer.

The simulation trends in Figure 3.5 were borne out experimentally. Under controlled indentation, the resonance moved monotonically to lower frequency as pressure increased (Figure 3.6). Over the low-pressure range most relevant to glove contact ($\sim$ 0 to 14 kPa), the 2 mm solid PDMS sample produced the largest shift, reaching roughly 39 MHz at 14 kPa, while a 6 mm porous PDMS layer reached roughly 27 MHz and outperformed the corresponding 6 mm solid layer. This is consistent with the intended mechanism: thinner

or more compressible dielectric layers generate a larger pressure-induced change in effective capacitance. For the selected operating configuration, the reported pressure sensitivity was 3.39 $\mathrm{MHz\,kPa^{-1}}$ [96].

Separate loading and unloading sweeps showed only modest path separation over the measured range, indicating that the RF response was repeatable enough for proof-of-concept characterization [96]. Additional higher-load measurements showed partial saturation of the frequency shift and only a small pressure-induced amplitude change, which reinforced the design intuition that frequency should be treated as the primary pressure channel in this architecture.

Bending was evaluated by varying the curvature/alignment condition between the tag and reader and observing the corresponding transmission response (Figure 3.7). As the bending angle decreased from 180° to 160°, the S_{21} amplitude changed by about 2.5 dB, while the resonance frequency also shifted by roughly 40 MHz. This confirmed that the same coupled structure can detect bending, but it also exposed a practical challenge for glove use: frequency is not exclusively pressure-specific, so multimodal operation requires either controlled geometry or a calibration model that explicitly accounts for cross-sensitivity.

To assess feasibility for wearable deployment, we additionally demonstrated that a low-cost portable nano-VNA can resolve the pressure-induced frequency shifts, suggesting a practical path toward compact instrumentation [106].

3.3.5 Limitations and Transition to Local-Readout Architectures

Despite successful proof-of-concept demonstrations, the microwave sensor surfaced several limitations that made it a poor fit for the final glove platform. First, the resonator and reader structures remain centimetre-scale RF components with limited tolerance to curvature and alignment errors; this is fundamentally difficult to reconcile with the continuously changing geometry of a hand-worn textile. Second, the response depends not only on the local pressure state but also on the tag–reader spacing and orientation, so natural hand motion can generate electromagnetic artefacts that are difficult to distinguish from the intended signal. Third, the two observables are only partially decoupled: pressure is best read from frequency, and bending is best read from amplitude, but both quantities affect the full transmission curve. Finally, although the nano-VNA result demonstrates a path toward portable instrumentation, the overall RF stack is still bulkier and more packaging-sensitive than a local capacitive transducer embedded directly into the glove.

Just as importantly, a successful single-sensor demonstration did not by itself solve the final glove problem. The intended platform requires many distributed sensing nodes rather than one isolated pressure element. Extending the microwave route to that scale would have required a dedicated multichannel RF interrogation and readout-system effort, including robust sensor addressing, management of coupling variation, and compact reader electronics; prior passive-resonance and soft-skin work likewise show that readout and wiring become system-level problems as wearable or tactile systems scale [74, 75]. Because the central contribution of this thesis is sensor design, modeling, and personalized glove integration rather than RF-reader circuit development, the microwave route is retained here as an informative down-selection study and the main development shifts toward soft local-readout capacitive architectures.

Chronologically, these limitations mattered for more than down-selection. These limitations showed that trial-and-error alone could not reliably guide sensor design: geometry, materials, and readout physics were tightly coupled, and the same architecture could perform well on one axis while failing another. That observation motivates the central methodological step of this chapter, namely a reusable design framework that connects parameterized geometry, nonlinear mechanics, mechanism-specific transduction models, and fabrication down-selection.

Table 3.2: Microwave resonator route: prototype and RF characterization summary.

Parameter	Setting used in this thesis
Reader substrate	0.508 mm PTFE substrate with 17.5 µm copper traces
Tag footprint	Approximately 45 mm × 20 mm
Reader footprint	Approximately 95 mm × 58 mm
Dielectric variants	2, 4, and 6 mm solid PDMS; 6 mm porous PDMS prepared by sugar templating
Simulation conditions reported in the associated publication	Effective relative permittivity varied from 1 to 3 for the 2, 4, and 6 mm PDMS cases; simulated bending angle varied from 180° to 160°
RF instrument	Two-port vector network analyzer, S5065, Copper Mountain Technologies, for main characterization; portable nano-VNA used for feasibility check
Pressure protocol	Normal compression over approximately 0–14 kPa for the low-pressure glove-relevant comparison; loading and unloading sweeps were performed; each sensor was measured for three repeats
Pressure observable	Resonant-frequency shift extracted from S_{21} notch location
Pressure response used for down-selection	2 mm solid PDMS produced approximately 39 MHz shift at 14 kPa; 6 mm porous PDMS produced approximately 27 MHz shift and exceeded the corresponding 6 mm solid PDMS response; reported selected sensitivity was 3.39 MHz kPa^{-1}
Bending protocol	Tag–reader curvature / alignment varied from approximately 180° to 160°
Bending observable	S_{21} notch amplitude, with frequency shift monitored as a cross-sensitivity indicator; approximately 2.5 dB amplitude change and approximately 40 MHz frequency shift over 180°–160°
Sample count and repeats	Same sensor measured with three repeated measurements; independent-device statistics were not claimed for this down-selection prototype
Full protocol source	Associated microwave publication [96]

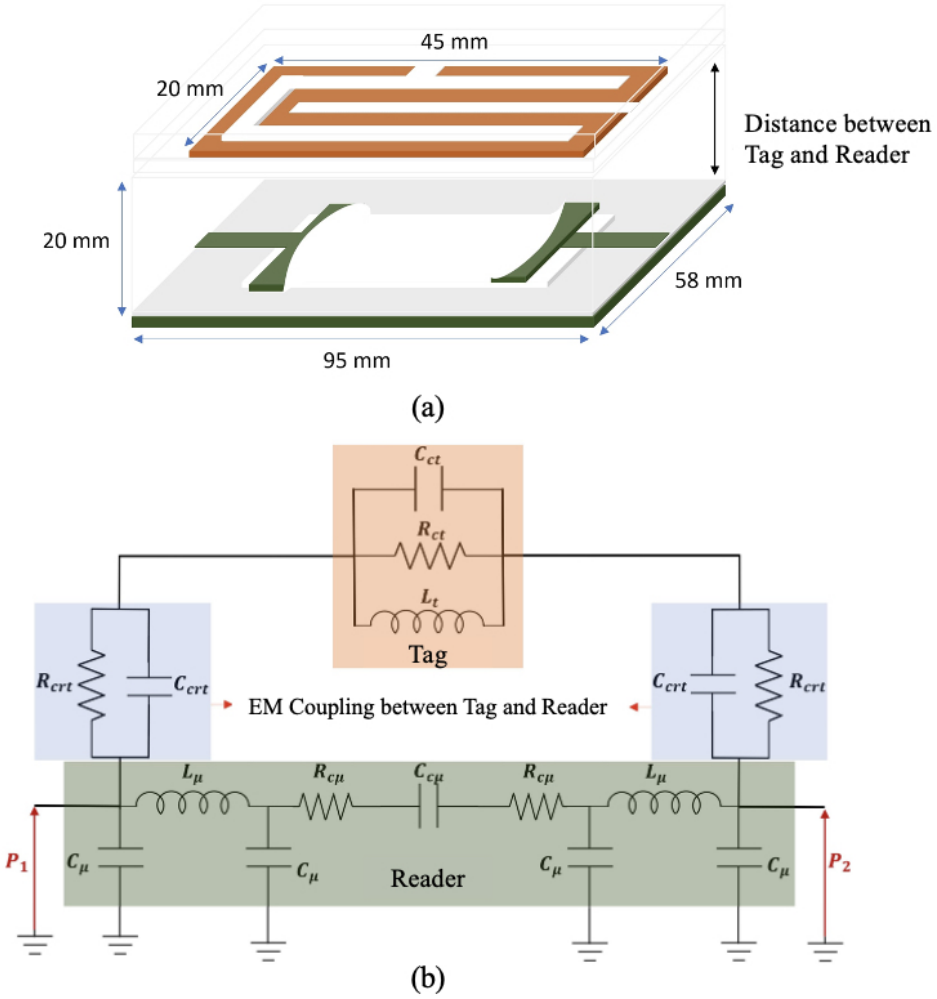


Figure 3.4: Microwave sensor geometry and interpretation model. (a) Physical dimensions of tag and reader. (b) Equivalent-circuit representation of coupled resonant response. Reproduced from [96]. © 2023 IEEE.

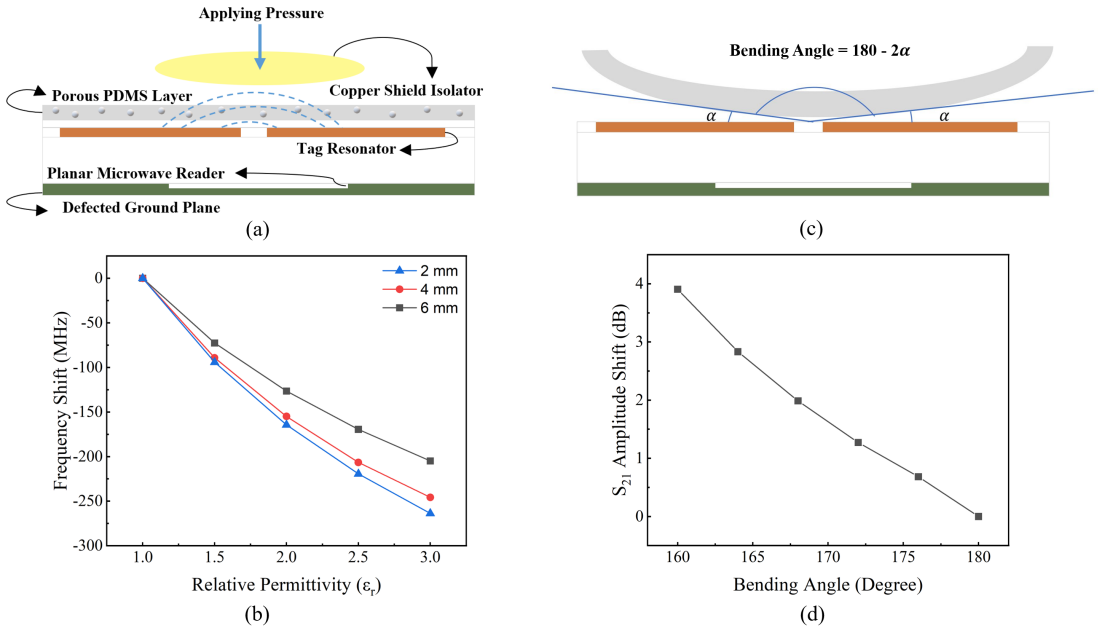


Figure 3.5: Simulation-guided interpretation of the microwave sensor. (a) Pressure increases permittivity and lowers resonant frequency. (b) Simulated frequency shift for 2, 4, 6 mm PDMS layers. (c) Bending changes tag geometry. (d) Simulated S_{21} amplitude shift under bending. Reproduced from [96]. © 2023 IEEE.

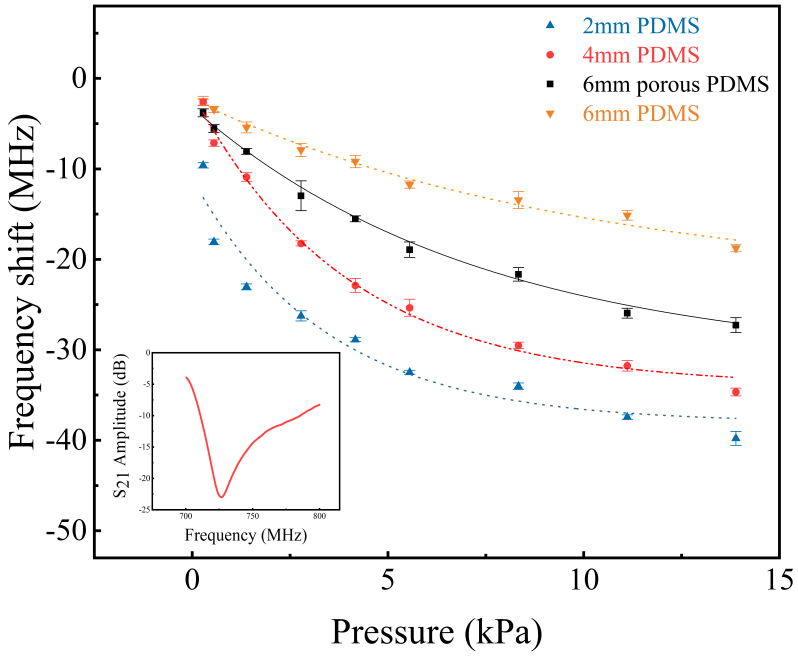


Figure 3.6: Measured pressure response for four dielectric configurations. Thinner layers produce larger frequency shifts; porosity improves thicker-sample response. Reproduced from [96]. © 2023 IEEE.

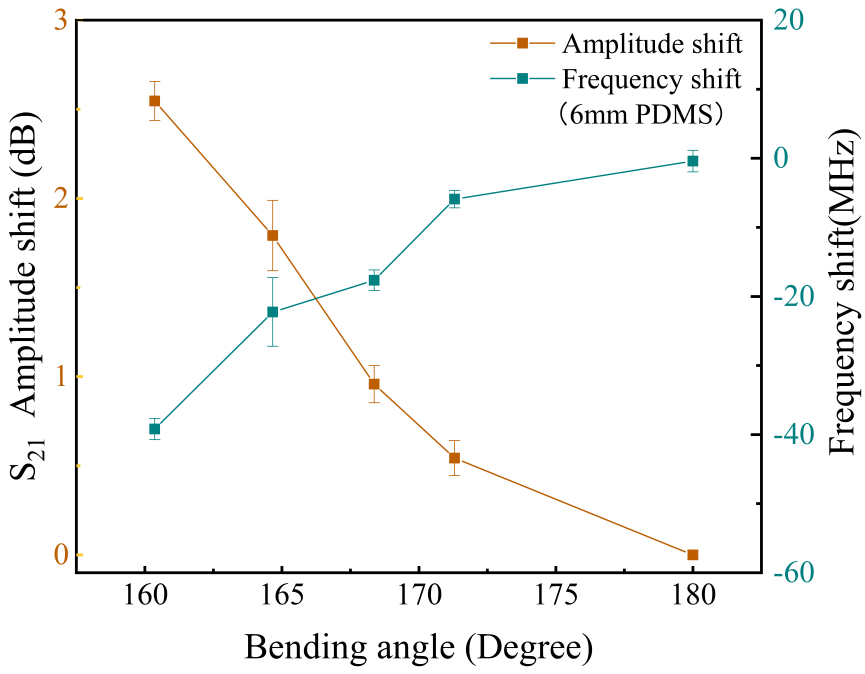


Figure 3.7: Measured bending response. As bending angle decreases from 180° to 160°, S_{21} amplitude shows monotonic change and resonance frequency shifts. Amplitude is more distinctive for bending; frequency remains cross-sensitive. Reproduced from [96]. © 2023 IEEE.

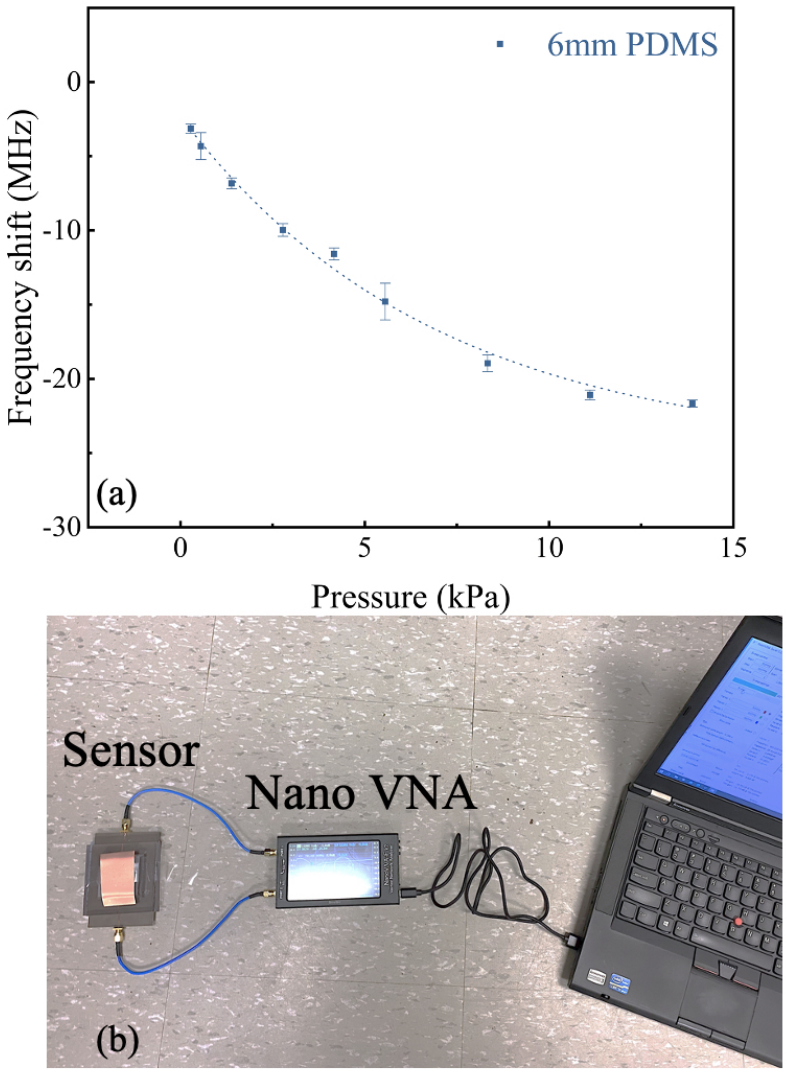


Figure 3.8: Portable nano-VNA validation. (a) Frequency shift measured with compact readout during pressure loading. (b) Benchtop test setup. Resonance shift is resolvable without full laboratory VNA. Reproduced from [96]. © 2023 IEEE.

3.4 Simulation-Driven Design Framework

The common methodological contribution of this chapter is not a single optimized pressure sensor, but a reusable workflow that converts a parameterized geometry family into fabricated sensor candidates. Chapter 2 provides the underlying mechanics tools, including material characterization and the DolfinX nonlinear contact solver.

3.4.1 Limitations of Prior Modeling Approaches

Section 3.1 established that microstructure geometry is the dominant design lever across capacitive and iontronic sensing mechanisms, and that progressive engagement across a multi-tier array is the primary route to broad-range linearity. The pressure-sensor literature has made meaningful progress in the direction of model-guided design: Ruth *et al.* developed predictive equations linking pyramidal microstructure geometry and dielectric material properties to sensor performance, enabling targeted design for specific applications without pure fabrication-by-trial [17, 18]. More broadly, FEM-based comparison studies and analytical models have reduced the reliance on unguided fabrication by making structure–property relationships more transparent [19, 20, 38].

These contributions represent an important shift in the field, but they address only part of the design problem. Even the most predictive forward-modeling approaches in the pressure-sensor literature remain constrained in three ways that are particularly important for the glove application of this thesis:

1. **Single-cell scope.** Predictive models and FEM comparison studies are built around one repeating unit cell. Glove-integrated sensors require multi-tier arrays whose composite response depends on sequential engagement across cells of different heights or compliances — a design problem that single-cell models cannot address directly [39, 26].

2. **Mechanism-locked modeling.** The mechanics and transduction models are typically coupled to one sensing mechanism, so the workflow must be rebuilt when the electrical physics changes — for example, from iontronic EDL scaling to conventional capacitive gap-and-area dependence [21, 29, 107, 22, 108].

3. **Fixed operating range.** Performance is characterized over a single declared pressure window, with no systematic route to re-derive an optimal array when the target range changes [65, 109, 68].

The framework developed here addresses these three limitations directly. It uses the same nonlinear mechanics backbone across sensing mechanisms, moves the design problem from the single cell to the array level, and treats the target pressure range as an explicit optimization input rather than as a fixed property of a preselected geometry.

3.4.2 Framework Overview

Across the iontronic and capacitive sensors, the same abstract workflow is used: begin from a parameterized geometry family, extract common mechanics histories with nonlinear FEM, compress those histories into surrogate models, convert them into electrical response through the appropriate transduction physics, and then search for a printable array that satisfies the target pressure window and application constraints.

The following subsections unpack the three layers that matter most for the present chapter: the shared mechanics backbone, the mechanism-specific transduction model, and the range-aware optimization step.

For reproducibility, Table 3.3 summarizes how the abstract workflow was instantiated for the two soft local-readout pressure-sensor routes developed in this chapter.

3.4.3 Nonlinear FEM as the Mechanics Backbone

The common mechanics engine of the framework is the nonlinear FEM pipeline developed in Chapter 2. Given a parameterized microstructure and a prescribed compression or indentation history, the solver produces three core histories that are reused throughout the chapter: reaction force, effective contact area, and effective separation or gap as functions of displacement. These are mechanism-independent quantities. They describe the evolving mechanical state of the structure under load, regardless of whether the later electrical interpretation is iontronic or conventional capacitive.

The FEM solver is not asked to predict capacitance directly. Instead, it supplies a shared intermediate mechanical description that can later be passed into different transduction models. For a representative frustum-like microstructure, for example, the solver typically returns an initially compliant response followed by hyperelastic stiffening, together with monotonic contact-area growth and diminishing effective gap under compression. Those histories are precisely the ingredients needed to reason about both sensitivity and saturation. Figure 3.9 makes this mechanics role explicit. Panel (a) shows representative large-deformation FEM states for a frustum-like cell, while panels (b) and (c) show

Table 3.3: Implementation summary of the Chapter 3 design framework for the two local-readout pressure-sensor routes.

Route	Geometry representation	FEM / surrogate dataset	Transduction model	Optimization objective
Iontronic EDL route	Low-dimensional frustum family parameterized by height, top radius, base radius, and array arrangement	Structured DolfinX compression sweeps; outputs include reaction force and effective contact area; surrogate predicts contact-area evolution over compression	Area-dominated EDL relation, $C_{\mathrm{int}}(P) \approx c_{\mathrm{EDL}} A_{\mathrm{eff}}(P)$, at the selected readout frequency	Select a manufacturable multi-frustum layout with high low-load gain and monotonic response over the glove-relevant pressure range
Solid capacitive route	B-spline/superellipse cross-section with 8 shape coefficients plus height, decoded into multi-tier arrays	Active-learning DolfinX dataset with exploratory and production mesh resolutions; outputs include force, contact area, and deformed gap histories	Sliced capacitive model that integrates local polymer/air fraction and effective separation through the deformed stack	Differential-evolution search over tier geometry and array assignment to maximize range-specific linearity and sensitivity under manufacturability constraints

the two most reusable outputs of the solver: reaction force and normalized contact area as functions of compressive strain.

Nonlinear mechanics are essential here because the performance metrics of interest are set in the large-deformation regime. Linear-elastic approximations can miss the contact-area acceleration and strain stiffening that determine where a pressure sensor begins to saturate. This is illustrated more directly in Figure 3.10, which compares hyperelastic and linearized mechanics assumptions against a representative printed microstructure and experiment. Panels (b) and (c) show that the hyperelastic material law and evolving contact model affect different parts of the mechanics prediction: the material law strongly changes the force growth at higher strain, while the contact treatment determines how

rapidly the active area expands once engagement begins. Panels (d)–(f) then show the consequence at the device level. Using either a better material model or a better contact model alone improves the capacitance prediction relative to a simpler prescribed-contact linear baseline, but the best agreement is obtained only when both effects are included together. The point of this comparison is not to claim that one reduced simulation exactly reproduces experiment in all details, but to justify why the framework carries forward a hyperelastic-contact mechanics backbone rather than a small-strain approximation with fixed contact assumptions.

For soft PDMS-based wearable structures, accurate FEM prediction in compression and related loading modes depends on an appropriate hyperelastic constitutive description rather than a small-strain approximation [110, 41]. The hyperelastic and contact formulations calibrated in Chapter 2 are therefore carried forward as the common mechanics backbone of the framework.

3.4.4 Surrogate Modeling and Array-Level Optimization

Although a single FEM simulation is tractable, direct brute-force optimization becomes impractical once array-level design is introduced. Even a modest frustum array with several tiers and two descriptors per tier already creates a multi-parameter search space, while a B-spline array with many tiers and many shape descriptors becomes far larger still. At that point, the bottleneck is no longer the mechanics formulation itself, but the number of times it would need to be evaluated during search.

Surrogate models resolve that bottleneck by approximating the mapping from geometry descriptors and compression state to the mechanics outputs of interest. In this framework, the surrogate is not used merely to accelerate one more single-cell sensitivity plot. Its more important role is to make array-level optimization feasible at all, because it allows the search to query candidate tier combinations at negligible cost compared with full FEM [45, 111, 112].

The sampling strategy used to build the surrogate depends on the geometry family. Low-dimensional families can often be covered by structured sweeps, whereas higher-dimensional families require a more selective active-learning strategy. That distinction is application-level rather than framework-level: Section 3.5 applies the first case to frustums, and Section 3.6 applies the second to B-splines.

Aspect	Iontronic route	Capacitive route
Dominant electrical lever	Effective interfacial area	Effective area and dielectric thickness
Core mechanics outputs used	$A_{\text{eff}}(P)$, force	$A_{\text{eff}}(P)$, $t_{\text{eff}}(P)$, force
Implication for geometry choice	Low-dimensional frustums are often sufficient	Richer profile families help delay saturation and improve linearity

Table 3.4: Shared mechanics, different transduction models. The same FEM backbone feeds both mechanisms, but the electrical interpretation and therefore the useful geometry family differ.

3.4.5 Mechanism-Specific Transduction Models

Once the shared mechanics histories are available, a mechanism-specific transduction model converts them into electrical response. This is the key separation in the framework: the mechanics solver remains reusable, while the electrical model changes with sensing mechanism.

For the iontronic case, the dominant electrical term is interfacial. To first order,

$$C_{\text{EDL}}(P) \approx c_{\text{EDL}} A_{\text{eff}}(P), \tag{3.2}$$

which reflects the electric-double-layer-dominated scaling between effective contact area and interfacial capacitance in iontronic sensors [60, 65], so the main design task is to shape a stable and monotonic contact-area trajectory. For the conventional capacitive case, the response is instead governed by a bulk dielectric relation,

$$C(P) \approx \varepsilon_0 \varepsilon_{\text{r}} \frac{A_{\text{eff}}(P)}{t_{\text{eff}}(P)}, \tag{3.3}$$

which is the standard parallel-plate approximation adapted to deformable microstructured dielectric layers in flexible capacitive pressure sensors [18, 19], which makes the balance between area growth and gap closure much more important. Because $t_{\text{eff}}(P)$ stiffens and saturates under compression, linearity becomes a harder geometry problem.

This separation is what makes the framework reusable. The geometry parameterization, nonlinear finite-element mechanics, surrogate modeling, and range-aware optimization layers operate on deformation histories such as force, contact area, and effective geometry

under load. These layers are not inherently restricted to capacitive sensing and could, in principle, be reused for other wearable sensor architectures whose electrical response is driven by mechanically predictable deformation.

However, extension to conventional conductive-network piezoresistive sensors would not be a direct substitution of capacitance with resistance. In graphene-, carbon-nanotube-, silver-nanowire-, or nanoparticle-based composites, resistance change depends not only on the macroscopic deformation of the elastomer but also on material-specific evolution of the conductive network, including percolation state, inter-particle contact formation and loss, tunneling distance, and hysteretic network rearrangement [113, 114]. A piezoresistive implementation would therefore require an additional electromechanical transduction model calibrated for the chosen conductive material system. A more direct resistive extension of the present workflow would be a geometry-dominated architecture such as a liquid-metal-filled channel embedded in silicone, where the conductor resistivity may be treated as approximately constant and the response estimated primarily from deformation-induced changes in channel length and cross-sectional area [115, 116]. Thus, the present thesis demonstrates direct transferability across capacitance-based mechanisms, while extension to ordinary piezoresistive composites remains plausible but would require a new transduction layer and is not experimentally validated here.

3.4.6 Range-Tunable Array Optimization

In this framework, the target pressure range is treated as an input to the optimization problem rather than as a property that is discovered only after fabrication. At a high level, the optimizer takes four pieces of information: the desired pressure window, the relative emphasis on linearity versus sensitivity, the available sensor footprint, and the number of tiers or cells allowed in the array. It then searches over the array configuration using the surrogate-plus-transduction model as the objective function.

The structure of this objective is important for optimizer selection. The array-decoding step maps continuous design variables into discrete tier counts, the linearity metric contains broad near-equivalent plateaus, the capacitance model relies on interpolation-based inversion between force and displacement, and infeasible candidates are rejected through large penalties when they violate structural or response constraints. These features make the search landscape piecewise, non-smooth, and interrupted by dead regions rather than a clean continuously varying surface. A population-based derivative-free search is therefore used here rather than gradient-based or Bayesian alternatives; the concrete optimizer choice and its justification against Bayesian optimization are presented alongside the capacitive application results in Section 3.6.5.

The practical meaning of this architecture is *range tunability*. The same trained mechanics backbone can be retargeted to a different application simply by changing the desired operating window and rerunning the search. A designer who needs a nearly linear response over one low-pressure regime will not generally arrive at the same optimal array as a designer targeting a broader grasp-level range. Much of the existing literature instead reports a geometry optimized for one declared sensing task or one achieved operating window, such as specialized biosignal monitoring, a fixed broad-linearity composite dielectric structure, or a targeted gradient micro-cone architecture for a specific pressure band [17, 21, 29, 108, 28]. That retargetability is one of the sharpest differences between the present framework and the more common pattern of reporting one optimized geometry for one fixed range.

The framework also embeds fabrication-awareness from the beginning of the search: candidate geometries are screened for manufacturability before full FEM evaluation, so that simulation budget is not spent on unprintable designs. The concrete screening criteria and their effect on the B-spline design space are described in Section 3.6.3. Finally, to make the pipeline accessible beyond the immediate thesis experiments, the optimization workflow was wrapped in an interactive web-based design tool; its interface and usage are presented alongside the capacitive results in Section 3.6.7.

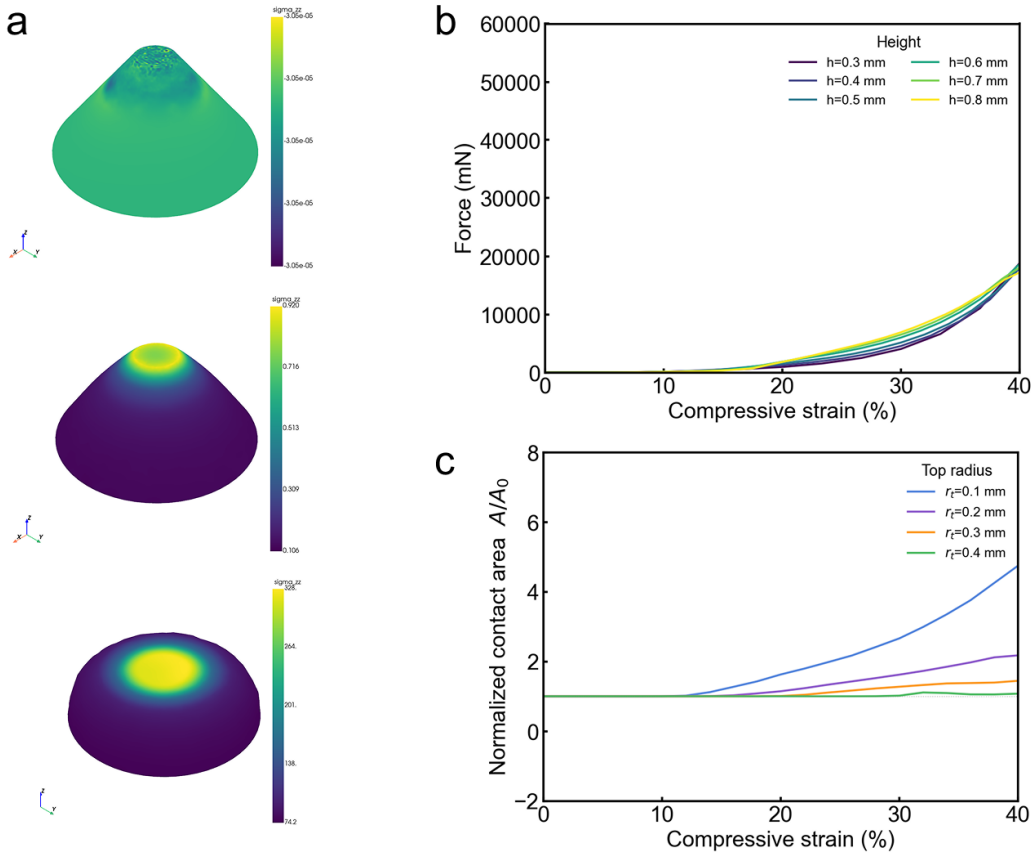


Figure 3.9: Representative nonlinear FEM outputs used as the mechanics anchor. (a) Large-deformation solutions for a frustum under compression. (b) Reaction force versus strain for several frustum heights. (c) Normalized contact area versus strain for several top radii. These histories are reused by both iontronic and capacitive transduction models.

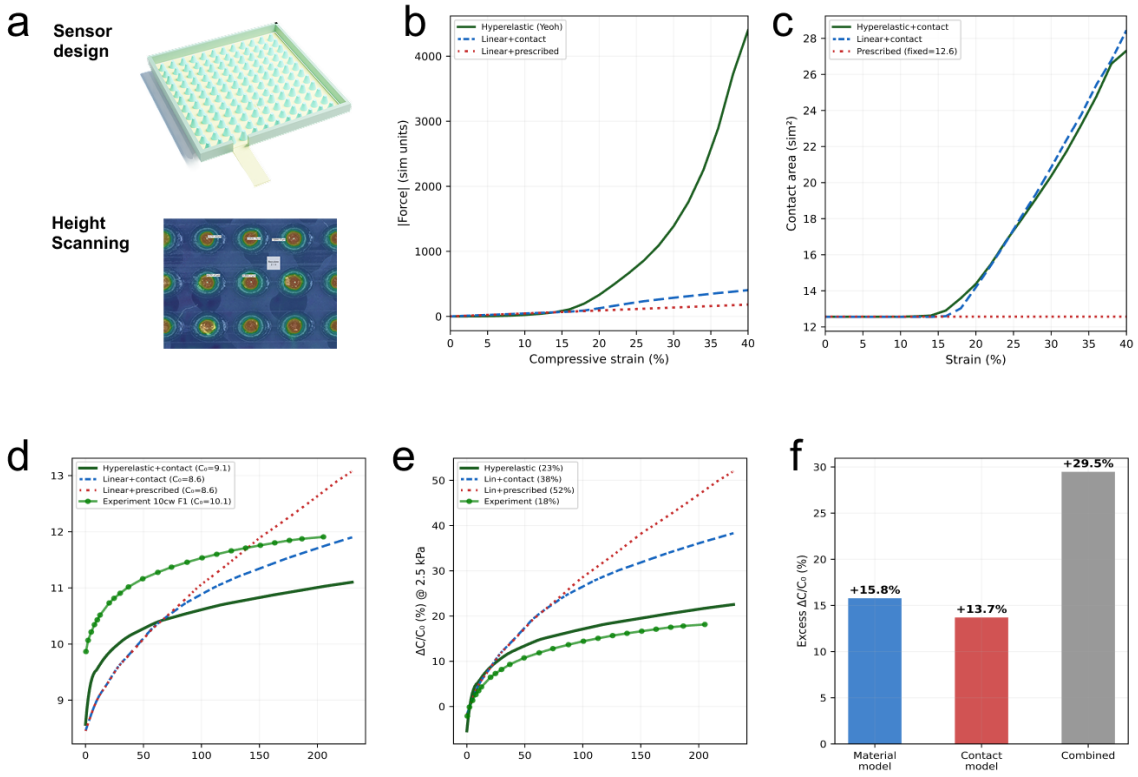


Figure 3.10: Why nonlinear material response and evolving contact are retained in the framework. (a) Representative multi-feature sensor geometry and scanned fabricated heights used for comparison. (b) Predicted force growth under compression for hyperelastic, linear-elastic-with-contact, and linear-elastic-with-prescribed-contact models, showing that linearized mechanics underestimates the strong stiffening at larger strain. (c) Predicted contact-area evolution, showing that evolving contact must also be modeled explicitly rather than prescribed as fixed. (d) Absolute capacitance–pressure comparison between representative simulations and experiment. (e) Corresponding normalized response comparison, showing that material and contact modeling both affect the predicted gain. (f) Excess normalized capacitance contribution attributed to the material model, contact model, and their combined effect. Together, these comparisons show why a hyperelastic-contact formulation is used as the common mechanics engine of the design framework.

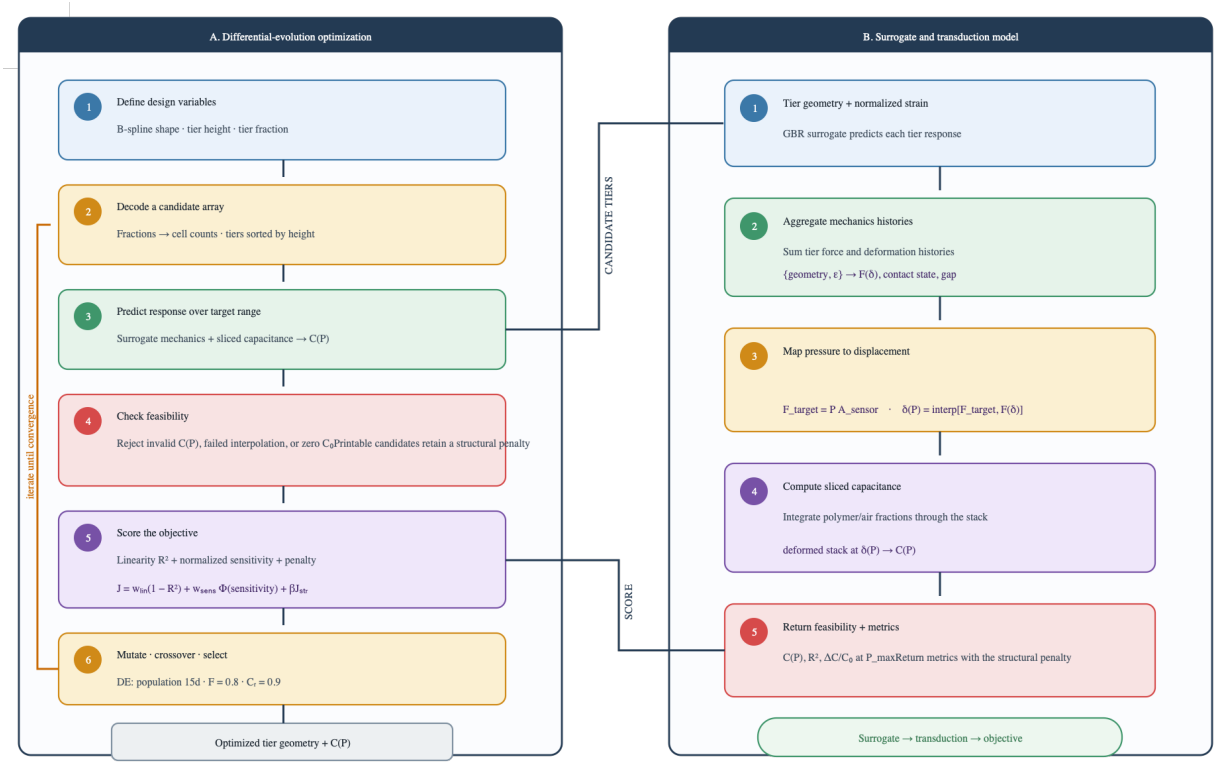


Figure 3.11: Surrogate-assisted range-tunable design workflow. (a) Differential evolution decodes tiered candidate arrays, predicts their responses, screens infeasible configurations, and iteratively minimizes a weighted performance objective. (b) The surrogate-plus-transduction model aggregates tier mechanics, maps the target pressure to displacement, and computes the sliced-capacitance response and associated performance metrics.

3.5 Iontronic EDL Pressure Sensor

Iontronic sensing is attractive for the primary glove-sensing route because it uses EDLs at soft electrode–electrolyte interfaces to generate interfacial capacitances far larger than those of conventional bulk dielectrics, enabling large measurable changes under modest normal loading in thin, flexible stacks [60, 65, 68, 77, 61].

Recent iontronic pressure sensors have shown that high sensitivity, broad range, and strong linearity depend strongly on interface geometry. Bai *et al.* used graded intrafillable microstructures to avoid premature saturation while retaining very high low-load gain [65]. Yang *et al.* showed that gradient micro-pyramids can extend linearity to much higher pressures [68]. Shi *et al.* further demonstrated that iontronic architectures can be packaged into mechanically robust, array-compatible skins for robotic use [77]. These studies define the design target adopted here: preserve the interfacial sensitivity of iontronics, but realize it in a stack that is compatible with glove-scale fabrication, repeated wear, and local capacitance readout.

The lower-left panel of Figure 3.12 places the present design in context by comparing representative literature reports using two summary axes: reported sensitivity and pressure range. This map is intended as a capability comparison rather than a perfectly uniform benchmark, because not every paper reports sensitivity in exactly the same way. Some studies provide an explicit linear-window slope, whereas others emphasize a particularly strong subrange within a broader operating regime. For the present work, the plotted point is based on the strongest loading-only local linear fit extracted from the averaged C/C_0 response, since the full iontronic response is strongly nonlinear rather than globally constant-slope. Even with that caveat, the comparison is useful: the framework-guided frustum route sits near the upper end of the iontronic sensitivity cluster while maintaining a substantially broader usable pressure range than ultralow-range demonstrations.

For this mechanism, frustums are a natural geometry family. Within the framework of Section 3.4, the dominant electrical lever is effective interfacial area $A_{\mathrm{eff}}(P)$, so the central mechanics problem is to shape a stable and monotonic contact-area trajectory under compression. That does not require the same geometric freedom as the conventional capacitive case discussed later. A low-dimensional, interpretable family is sufficient, provided it can be fabricated repeatably and searched systematically. Sharper pyramidal geometries are an obvious alternative and are often favored in the capacitive and iontronic sensor literature because sharp tips can amplify local deformation and improve low-load sensitivity [25, 20, 19]. Our own preliminary comparisons were consistent with that trend: molded pyramids produced higher initial sensitivity than the printed frustum structures. However,

they were not selected as the primary design family for this chapter because they fit the fabrication workflow less well. In our process, realizing high-quality pyramids required an additional molding step, while the material properties and final geometry of cast-cure PDMS structures are more sensitive to formulation and cure conditions than the direct 3D-printed silicone route used elsewhere in the chapter [110, 54]. For a framework intended to support repeated geometry iteration, direct fabrication, and glove-scale integration, that extra transfer step and materials variability were significant practical disadvantages. Frustums therefore offer the better balance for the iontronic route in this thesis: although they may not maximize peak sensitivity to the same extent as sharp molded pyramids, they are simple enough for structured sweeps, compatible with direct 3D printing and conductive coating, and rich enough to tune progressive contact engagement across a glove-relevant pressure range.

The iontronic transduction model used throughout this section is the area-dominated EDL scaling introduced in the framework (Section 3.4.5, Table 3.4): the pressure-dependent interfacial capacitance $C_{\text{int}}(P, \omega) \approx c_{\text{EDL}}(\omega)\, A_{\text{eff}}(P)$, where c_{EDL} is an effective areal interfacial capacitance at the chosen readout frequency and $A_{\text{eff}}(P)$ is the pressure-dependent interfacial area. Because charge separation occurs over a nanometre-scale Debye layer rather than across a bulk dielectric, the interfacial areal capacitance can be orders of magnitude larger than the geometric capacitance of the same footprint, which is the primary reason this mechanism was selected for the glove application [60, 65, 68]. The practical consequence for device design is twofold: the unloaded capacitance can remain in the few-picofarad range because the real electrochemically active contact area at zero load is much smaller than the nominal projected area (due to surface roughness, trapped air, and incomplete gel conformity), and the dominant geometry problem reduces to shaping a clean, monotonic modulation of $A_{\text{eff}}(P)$.

Figure 3.13 collects the design-level picture for the iontronic route. Panel (a) shows the layer stack in cross-section. Panel (b) makes the EDL transduction explicit: as the silver-coated frustum electrode is pressed into the hydrogel, the real interfacial contact area grows, driving $C_{\text{EDL}}(P)$ upward; the reduced equivalent circuit in the same panel shows how ionic resistance and leakage together shape the measured impedance response. Panel (c) is the 3D surface scan of the fabricated electrode, confirming that the printed frustum array preserves the intended topography after silver coating. Panel (d) compares the normalized capacitance responses of representative framework-guided frustum candidates, showing the gain–linearity trade-off that motivates the staged optimization described in Section 3.4.

For instrumentation and design purposes, the sensor is interpreted using a minimal lumped circuit rather than a unique electrochemical model. A useful reduced representation consists of an ionic resistance R_{ion}, an effective interfacial capacitance C_{int}, a leakage

path R_{leak}, and, when needed, a secondary geometric capacitance C_{geo} associated with residual bulk separation or sealing layers. If both the top and bottom interfaces contribute appreciably, then C_{int} can itself be viewed as the series combination of two EDL interfaces. One convenient impedance form for this reduced picture is

$$Z(\omega, P) \approx R_{\text{ion}} + \left[j\omega \left(C_{\text{int}}(P, \omega) + C_{\text{geo}} \right) + \frac{1}{R_{\text{leak}}} \right]^{-1}, \tag{3.4}$$

which reduces to the familiar series R_{ion}–C_{int} form when leakage and geometric contributions are small over the selected measurement window.

This equivalent-circuit view clarifies the main design choices in the remainder of the section. First, the apparent iontronic capacitance is frequency dependent because ion redistribution, interfacial polarization, and leakage all depend on the timescale of the electrical excitation [60, 61, 117]. This trend was also observed in the frequency sweeps of the three candidate gel formulations used in this work, where the apparent dielectric response varied strongly with readout frequency. Accordingly, $c_{\text{EDL}}(\omega)$ is treated in this thesis as an effective measurement-condition-dependent parameter rather than as a universal material constant. Second, once the readout frequency is fixed, the dominant geometry problem becomes the design of a clean, monotonic modulation of $A_{\text{eff}}(P)$, since that is the quantity most directly translated into $C_{\text{int}}(P, \omega)$ under the selected readout condition. In this sense, the lumped circuit is used here as a reduced model for design and readout interpretation: it captures the dominant dependencies needed to guide geometry optimization without claiming to identify the full electrochemical physics of the interface.

The iontronic medium used in this work is a PVA/H_3PO_4/PVP ionically conductive hydrogel selected from three candidate ionic-medium classes (hydrogels, ionogels, and ion-conducting elastomers) on the basis of workflow compatibility with the fast geometry-iteration loop required by the design framework. The material-class comparison, selection rationale, and concentration screening are documented in Chapter 2 (Section 2.3.5, Table 2.5). The key trade-off accepted here is environmental sensitivity: without encapsulation, the gel can lose water, stiffen, and drift over time, but this was acceptable because the goal was to provide a stable enough medium for comparing geometry-guided designs rather than to maximize standalone ionic-material performance.

In the present chapter, the selected hydrogel should therefore be understood as a deliberate demonstrator material rather than as the only viable ionic medium. Its role is to provide a low-cost, literature-established iontronic interface that can be fabricated repeatedly while the framework explores how geometry controls contact-area evolution, gain, and linearity. The use of a PVA/H_3PO_4-based system is consistent with prior iontronic

pressure sensors that also use this material family to study microstructure-controlled EDL response [65, 66], while the PVP addition in the present devices serves as a process aid for handling during fabrication.

The framework itself is not restricted to this hydrogel chemistry. Ionogels and ionically conductive elastomers remain compatible extensions when the dominant sensing mechanism is still governed by EDL formation and pressure-dependent interfacial contact area. In that case, the geometry parameterization, nonlinear mechanics, contact-area extraction, surrogate modeling, and optimization logic can be retained. What must be re-established for each new material class is the material-specific layer: the constitutive response of the ionic medium, the effective interfacial capacitance $c_{\mathrm{EDL}}(\omega)$, ionic resistance and leakage, interfacial conformity, and packaging stability. Thus, the present thesis experimentally demonstrates the framework with a PVA/H_3PO_4/PVP hydrogel, while transfer to ionogels or ionically conductive elastomers remains methodologically plausible but not yet experimentally validated here [68, 64].

The selected iontronic device uses an asymmetric multilayer stack tailored to glove integration. On the microstructured side, the electrode is formed by applying a stretchable silver-ink spray coating (PSPI-1000, NovaCentrix) onto the 3D-printed silicone substrate, allowing the electrode to conform to the frustum topography. On the opposing side, the counterelectrode is a silver-plated woven conductive fabric (Item 1167, Adafruit Industries) that preserves flexibility and improves compatibility with textile integration. Between these electrodes sits the PVA/PVP/H_3PO_4 hydrogel, which forms the iontronic interface under compression. The full stack is sealed using a 75 µm thermoplastic polyurethane (TPU) film (Bemis) to reduce dehydration and acid leakage.

This architecture is mechanically asymmetric by design. The printed elastomer side carries the microstructure and therefore determines the pressure-dependent contact mechanics, while the textile side acts as a compliant counterelectrode that can conform to glove curvature without imposing a rigid backing. At the same time, localizing the ionic medium within a thin sealed region reduces exposed gel area and makes the device more practical for daily wear than a fully exposed hydrogel sheet. The stack therefore couples materials, mechanics, and packaging into one integration problem rather than treating them as independent layers.

Within the design framework of Section 3.4, the iontronic geometry family is parameterized primarily by frustum height h, top radius r_{t}, base radius r_{b}, and the arrangement of features within the sensing pad. This parameterization keeps the design space low-dimensional enough for structured sweeps while still capturing the main geometric levers that influence contact onset, contact-area growth, and stiffness progression. For an

iontronic mechanism, this is the right level of complexity: the goal is to shape $A_{\text{eff}}(P)$ predictably, not to exhaustively search an arbitrarily rich profile basis.

Figure 3.12 consolidates the *experimental validation* of the selected iontronic route. It brings together the fabricated-device view, cyclic response, hysteresis, literature positioning, and comparison between the three framework-guided frustum variants, so the emphasis here is on repeatability, practical performance, and why the selected layout was carried forward.

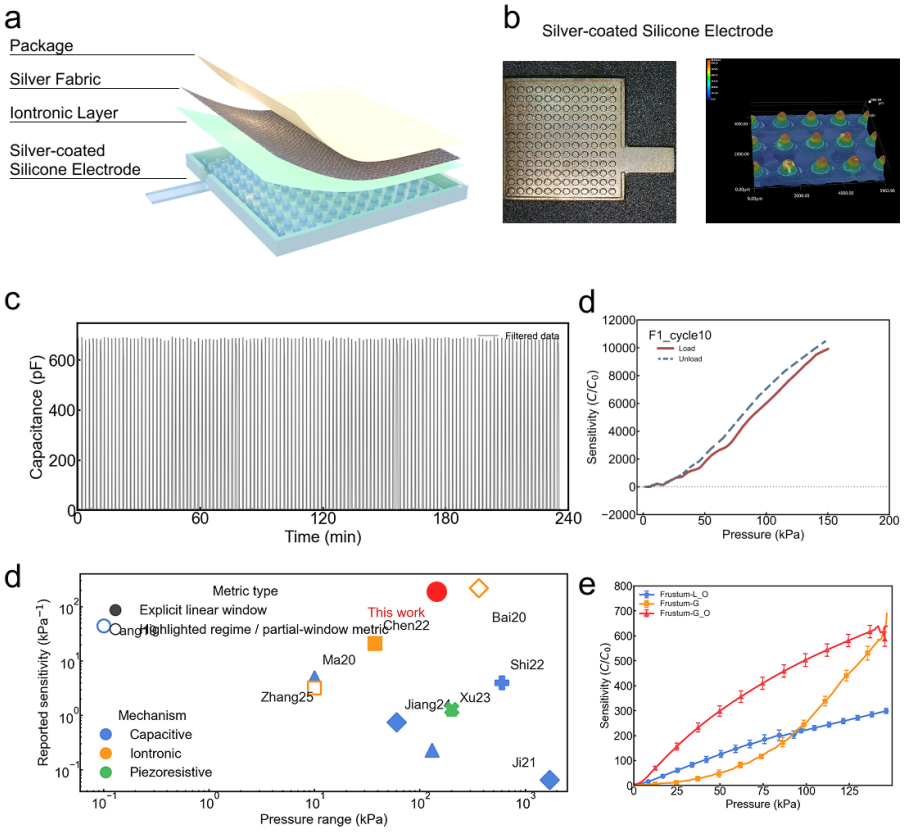


Figure 3.12: Experimental characterization of the selected iontronic frustum design. (a) Exploded schematic of the multilayer stack. (b) Fabricated device and 3D surface-scan confirming printed frustum array preservation. (c) Cyclic capacitance response over 240 min. (d, upper) Hysteresis showing closely tracked curves. (d, lower) Sensitivity–range comparison against literature; present work in red. (e) Normalized capacitance responses of three frustum variants, showing gain–linearity trade-off.

Candidate frustums were evaluated using the DolfinX mechanics pipeline described in Chapter 2. Each geometry was meshed automatically and compressed using the calibrated hyperelastic material model, yielding force–displacement and contact-area histories for use in later design stages. These outputs are especially valuable for iontronics because they separate the mechanics problem from the electrical model: once the evolution of contact area is known, the EDL relation can be applied without rerunning the full simulation for every circuit assumption.

Figure 3.13, by contrast, is included only as the *design-rationale* figure. Its role is to summarize the stack architecture, the reduced EDL/equivalent-circuit interpretation, and the within-family gain–linearity trade-off that motivated the frustum selection before moving into surrogate-guided array optimization.

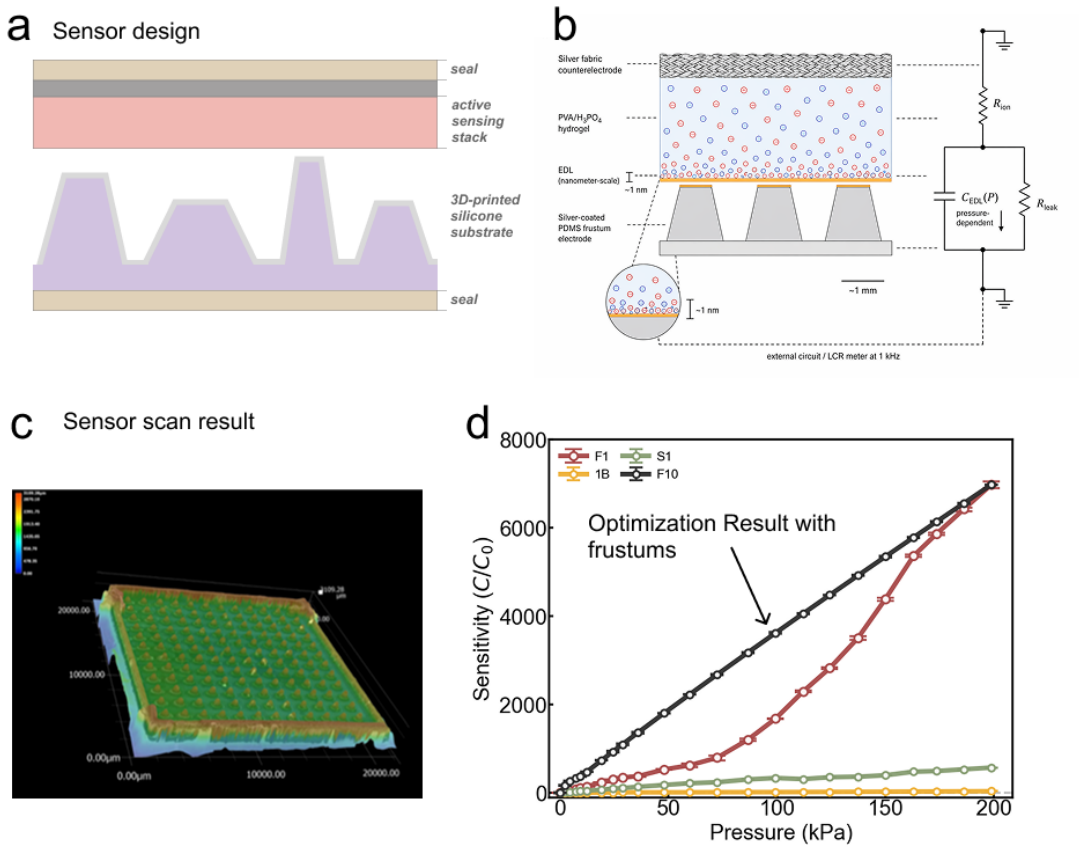


Figure 3.13: Design rationale for the iontronic EDL pressure sensor. (a) Stack schematic: silver-coated frustum, hydrogel, silver fabric, and packaging. (b) EDL transduction and equivalent circuit. (c) 3D surface scan confirming frustum topography preservation after coating. (d) Normalized capacitance responses of frustum candidates, illustrating gain–linearity trade-off.

The frustum sweep data were then used to train surrogate models that approximate the mapping from geometry and compression state to the mechanical outputs of interest. Because the family is low-dimensional, structured sampling was sufficient and active learning was not necessary at this stage. As summarized in Chapter 2, the resulting surrogates predicted contact area and stress with typical R^2 values of 0.95–0.99 and 0.92–0.97, respectively. The specific regressor implementation is less important here than what the surrogate enables: a transition from isolated single-feature analysis to tractable array-level

search.

Using the surrogate-plus-transduction model, multi-frustum arrays could then be optimized for glove-relevant performance objectives rather than selected by single-cell trial-and-error alone. This array-level step matters because the final pressure response depends on sequential engagement across multiple features, not just on the best-performing individual frustum. The selected iontronic layout is therefore best understood as a framework-guided frustum array rather than a hand-picked microstructure. In the present chapter, that selected route is represented by the optimized framework-guided frustum layout of Figure 3.12, which was carried forward because it preserved the desired monotonic, high-gain behavior while remaining compatible with the direct-printing workflow and the staged linearity-then-sensitivity optimization logic of the broader framework.

Device fabrication combined two tightly coupled tasks: preparation of the ionic medium and assembly of the multilayer stack. They are presented together here because, in practice, the final sensor response depends on the interaction between gel formulation, feature geometry, electrode alignment, and encapsulation rather than on any one step in isolation. We used a PVA-based hydrogel acidified with phosphoric acid as the iontronic medium, while keeping the base polymer composition constant across formulations:

- PVA: 4 g (Sigma-Aldrich, $M_w \approx$ 89,000–98,000, 99+% hydrolyzed)
- DI water: 36 g
- PVP: 0.2 g (Sigma-Aldrich, $M_w \approx$ 40,000; added to tune rheology and film handling)

To compare a low-, intermediate-, and high-acid formulation, three H_3PO_4 concentrations were prepared by varying the volume of phosphoric acid solution (85%, Sigma-Aldrich #612162) added:

Recipe	**[H_3PO_4] target**	**85% H_3PO_4 added**	**Notes**
A	1.2 M	3.3 mL	High-acid variant for screening
B	0.35 M	1.0 mL	Low-acid variant for screening
C	0.7 M	2.0 mL	Selected for main results after comparative screening

The gel was prepared using a staged heating/cooling protocol to ensure complete dissolution and to avoid thermal degradation during acid addition:

1. Combine 36 g DI water and 4 g PVA. Heat to 90–95 °C with magnetic stirring (∼700 rpm) in a covered beaker until the solution becomes clear (typically 1–2 h).

2. Cool to ∼60 °C, add PVP (0.2 g), and stir until fully dissolved (30–60 min).

3. Cool further to ∼40–50 °C. Add phosphoric acid solution (85%, Sigma-Aldrich #612162) *dropwise* to reach the target formulation (A/B/C) while stirring. Continue mixing for 15–30 min until uniform.

4. De-gas under vacuum to remove bubbles, then allow the solution to rest for ∼1 h prior to casting.

In the current chapter, the gel formulation is treated as a pragmatic materials choice validated by comparative dielectric/frequency characterization and successful device assembly, rather than as a standalone electrochemical study of ionic transport properties.

Once the gel was prepared, device fabrication proceeded in three stages. First, the microstructured elastomer substrate was fabricated using the same 3D-printable silicone platform characterized in Chapter 2, allowing rapid iteration of frustum geometry while keeping the base material model consistent with the simulations. Second, the active layers were assembled: the printed substrate was rendered conductive via the NovaCentrix PSPI-1000 silver coating on the structured side, the selected hydrogel was cast or laminated into the active region, and the Adafruit conductive fabric counterelectrode was aligned above it. Third, the stack was sealed using the 75 µm TPU film to reduce dehydration and acid leakage.

In practice, the most fabrication-sensitive steps are hydrogel handling and edge sealing. Small variations in trapped bubbles, gel thickness, or exposed edge area can alter the baseline capacitance and response repeatability. For that reason, the process is best understood as a repeatable assembly workflow rather than as a purely materials recipe: geometry selection, gel casting, electrode alignment, and encapsulation all contribute to the final response. Only the process details needed to reproduce the assembly are retained here; exhaustive electrical characterization of the gel itself is outside the scope of this chapter.

The fabricated device photograph and surface-scan verification are shown in Figure 3.12(b), confirming that the printed electrode preserves the intended frustum-array layout after the silver-coating and assembly steps.

Table 3.5 consolidates the fabrication and characterization parameters for the iontronic prototype.

Table 3.5: Iontronic EDL pressure sensor: fabrication and characterization summary.

Parameter	Setting used in this thesis
Geometry family	Direct-printed frustum array using the same pressure-sensor frustum design family used for the solid capacitive comparison; parameterized by frustum height h, top radius r_{t}, base radius r_{b}, and feature arrangement
Geometry values / bounds	Common base footprint 20 mm × 20 mm with 0.300 mm base thickness, 1.000 mm bottom diameter, and 0.400 mm top diameter. Tested variants included 3×3-in-4×4 arrays with nine heights from 0.300–0.500 mm or 0.300–1.000 mm, 2×2-in-6×6 arrays with four heights over the same ranges, and single-height controls at 0.300, 0.500, and 1.100 mm
Substrate / structured electrode	3D-printed silicone substrate rendered conductive using NovaCentrix PSPI-1000 stretchable silver-ink coating; two coating layers were applied and heat-cured at 100 °C for 10 min. Because coating thickness is difficult to measure on microstructured surfaces, the thickness was measured on flat coated samples only and was approximately 40 µm
Ionic medium	PVA/H_3PO_4/PVP hydrogel, Recipe C for the main device: 4 g PVA (Sigma-Aldrich, $M_w \approx$ 89,000–98,000, 99+% hydrolyzed), 36 g DI water, 0.2 g PVP (Sigma-Aldrich, $M_w \approx$ 40,000), and 2.0 mL of 85% H_3PO_4 solution (Sigma-Aldrich #612162)
Counterelectrode	Silver-plated woven conductive fabric, Adafruit Item 1167
Encapsulation	75 µm TPU film (Bemis) to reduce dehydration and acid leakage
Gel processing	PVA dissolved at 90–95 °C, PVP added after cooling to approximately 60 °C, H_3PO_4 added dropwise at approximately 40–50 °C, vacuum degassed for 30 min, then rested for approximately 1 h before casting
Degassing duration	30 min under vacuum
Gel thickness / casting gap	Approximately 400 µm, set using a film applicator
Readout	Keysight E4980AL/032 LCR meter, 1 kHz, 0.5 V AC excitation, Cs/Rs mode
Mechanical loading	Mark-10 F305 force stand with 100 N load cell and a 1.5 cm-diameter flat-ended indenter

Table 3.5: Iontronic EDL pressure sensor: fabrication and characterization summary (continued).

Parameter	Setting used in this thesis
Environmental condition	Room temperature, approximately 22–24 °C, ambient humidity, no environmental chamber control
Pressure range	Approximately 0–150 kPa for the main loading and hysteresis plots in Fig. 3.12(d,e), read from the plotted pressure axis
Loading protocol	Two loading modes were used: preset-point loading, where the Mark-10 stage stopped at individual target pressure points until force and capacitance readings stabilized, and continuous loading–unloading sweeps. Each condition was repeated three times. No fixed dwell duration beyond stabilization at the preset pressure points was recorded
Sample and repeat count	Each condition was repeated three times, following the same repeat convention as the solid capacitive pressure-sensor validation; cyclic repeatability was also recorded for the representative selected device over the duration shown in Fig. 3.12(c)
Main observables	$C(P)$, normalized C/C_0, loading–unloading hysteresis, and cyclic repeatability

The experimental characterization follows the general pressure-sensor protocol of Chapter 2. All measurements were performed at room temperature (approximately 22–24 °C) and ambient humidity without environmental chamber control. Capacitance is measured using the Keysight E4980AL/032 LCR meter at 1 kHz with 0.5 V AC excitation in Cs/Rs mode, and normal loading is applied with the Mark-10 F305 force stand and 100 N load cell. The characterization therefore focuses on (i) capacitance as a function of applied pressure over the glove-relevant low-load regime, (ii) hysteresis between loading and unloading, and (iii) repeatability across repeated cycles.

Figure 3.12 presents the characterization results. Panel (c) shows the cyclic capacitance response over an extended loading window, demonstrating that the device produces a large and repeatable output under sustained cycling. Panel (d, upper right) shows the loading–unloading hysteresis for the selected frustum device; the loading and unloading curves remain closely tracked, indicating that the hydrogel packaging and frustum geometry together produce a mechanically recoverable response. The emphasis here is on response quality rather than peak sensitivity: the more important question for glove integration

is whether the gain can be packaged into a monotonic, calibratable response, and these panels confirm that it can.

Relative to the requirements defined in Section 3.2, the iontronic route performs strongly on low-load gain, local-readout compatibility, and soft mechanical conformity. Its main limitation is environmental robustness: the hydrogel introduces dehydration and packaging constraints that are absent in the fully solid-state capacitive route. Nevertheless, the design rationale is clear. Compared with the microwave route, the iontronic architecture collapses the sensing mechanism into a local, glove-compatible interface. Compared with the conventional capacitive route, it delivers substantially larger signal change because the EDL mechanism amplifies the same contact-area evolution that the frustum geometry is designed to control. These advantages make the iontronic sensor the primary glove-facing pressure sensor in this thesis; its integration into the personalized glove platform is described in Chapter 5.

3.6 Capacitive Pressure Sensor with Solid Silicone Dielectric

3.6.1 Design Rationale

The material choices are conservative by design. The dielectric is Formlabs Silicone 40A resin (Shore 40A), a commodity 3D-printable elastomer with a relative permittivity of approximately $\varepsilon_r \approx 2.7$, which remained consistent across the tested frequencies. The electrodes are commercial conductive fabric, requiring no vapor deposition, sputtering, or chemical synthesis. These materials were chosen not for peak performance but for three properties that matter for generalization:

- **Accessibility.** Both materials are globally available from standard suppliers and require no specialized equipment beyond a desktop SLA printer.
- **Reproducibility.** The silicone resin is manufactured to industrial tolerances, and its mechanical properties are characterized in Chapter 2. Batch-to-batch variability is far lower than for hand-mixed composites or custom-synthesized ionic media.
- **Consistency with the simulation.** The same Yeoh constitutive model calibrated for this resin in Chapter 2 feeds the FEM backbone of the framework, so there is no modeling gap between the simulated and fabricated material.

The consequence of these choices is a lower sensitivity ceiling than the iontronic route. The signal gain available from bulk dielectric compression of a moderate-permittivity silicone is inherently smaller than the EDL-amplified response of an iontronic interface. That trade-off is accepted because the purpose of this section is not to compete with the iontronic sensor on peak sensitivity, but to show that the framework can extract the best achievable linearity and sensitivity from available materials. A researcher seeking higher sensitivity could substitute a higher-permittivity composite dielectric—for example, $BaTiO_3$/PDMS or CNT/silicone—and re-run the same pipeline. The geometry optimization, surrogates, and optimizer would remain valid because they operate on the mechanics, not on the material identity.

3.6.2 Sensing Principle and Linearity Constraints

As introduced in the framework (Section 3.4.5, Table 3.4), the capacitive transduction follows the parallel-plate relation $C(P) \approx \varepsilon_0 \varepsilon_r \, A_{\text{eff}}(P)/t_d(P)$, where the response depends on *both* the effective contact area and the inverse dielectric gap — unlike the iontronic case, which scales primarily with area alone. This dual dependence is what makes linearity the central design difficulty for this mechanism. Three effects conspire to produce early saturation:

1. **Hyperelastic stiffening.** As the microstructure compresses, the silicone strain-stiffens according to its nonlinear constitutive law. The incremental compliance decreases, so each additional unit of pressure produces less additional deformation—and therefore less additional capacitance change.

2. **Gap depletion.** As $t_d(P)$ shrinks, the $1/t_d$ term grows rapidly at first but then saturates as the gap approaches zero. The capacitance gains from further compression diminish.

3. **Simultaneous engagement.** If all microstructure features have similar heights and stiffnesses, they engage the platen at roughly the same pressure, producing a burst of capacitance change followed by saturation. There is no staged handoff to extend the response.

These three mechanisms are consistent with recent capacitive studies that explicitly link limited linear range to polymer hyperelasticity, premature contact saturation, and geometry-dependent contact evolution under load [21, 29, 107, 118].

Overcoming these effects requires geometry that produces *progressive engagement*: features of different heights or compliances that activate sequentially across the target pressure range, so that the composite response remains approximately linear even though each individual feature saturates within its own sub-range. Recent capacitive designs achieve this using gradient micro-domes, wave-like contact transitions, area-linearized cone electrodes, or gradient micro-cone dielectrics, but these strategies are usually demonstrated as one geometry recipe for one pressure window rather than as a retargetable design loop [22, 107, 118, 108]. This is the same sensitivity–linearity trade-off identified in the requirements of Section 3.2, and it is the reason multi-tier array optimization is essential for this mechanism.

3.6.3 Geometry Expansion: Frustums to B-Spline Profiles

The frustum geometry used for the iontronic sensor is not abandoned here; it is a special case within a broader family. A frustum is a B-spline profile with a straight sidewall—one specific point in a richer parameterization that also admits curved, concave, convex, and asymmetric cross-sections. The question is when the extra degrees of freedom matter.

Why frustums are sufficient for narrow ranges. For a narrow target pressure window, the optimizer needs only to match a small number of tier heights and stiffnesses to produce a monotonic, approximately linear response. In that regime, the frustum family—parameterized by height h, top radius r_{t}, and bottom radius r_{b}—is already rich enough: the optimizer finds good solutions without needing to reshape the sidewall profile. This is consistent with the iontronic results of Section 3.5, where the frustum sub-family produced effective multi-tier arrays because the contact-area-dominated transduction model is forgiving of the exact profile shape.

Why wider ranges require richer geometry. As the target range broadens, sustaining linearity becomes harder. The three saturation mechanisms identified in Section 3.6.2—hyperelastic stiffening, gap depletion, and simultaneous engagement—compound over a wider pressure window, and the optimizer needs more freedom to reshape the deformation sequence. A curved sidewall can delay the onset of full contact compared with a straight taper; a convex profile can produce a more gradual force progression; a flared base can redistribute stress to avoid premature stiffening. These adjustments are impossible within the frustum sub-family but natural within a B-spline parameterization. This range-dependent need for different contact-evolution strategies is consistent with prior capacitive

studies in which textured dielectrics, wave electrodes, gradient domes, and gradient cones each deliver different usable linear windows even though the underlying sensing mechanism remains the same [21, 107, 22, 108]. Figure 3.14 confirms this: for narrow target ranges both families achieve comparable linearity, but as the range widens the B-spline family maintains high linearity where the frustum family begins to fall short. The model labels above the bars identify the best-performing representative within each family at each target range, making clear that the preferred geometry is itself range-dependent rather than fixed across all operating windows.

The B-spline/superellipse parameterization. The geometry family used here is a simplified variant of free-form deformation (FFD). In classical FFD, a lattice of control points deforms an embedded volume, enabling arbitrary shape changes at the cost of a high-dimensional control space. The B-spline/superellipse parameterization used in this thesis retains the core idea—smooth, controllable shape variation governed by a small set of parameters—but restricts the deformation to a 2D cross-sectional profile that is then revolved or lofted into a 3D cell. This restriction is deliberate: it keeps the parameterization low enough in dimension (8 shape parameters plus height) to be tractable for surrogate-based optimization, while still spanning a substantially richer shape space than frustums alone.

Each candidate profile is defined by 8 B-spline/superellipse coefficients that control the sidewall curvature and taper, together with the cell height. The bottom footprint is constrained by the printable base pattern, and the top contact surface is constrained to remain smooth and convex for stable platen engagement. Between these two ends, the sidewall can curve inward, outward, or follow a compound path, producing profiles that range from near-frustum to rounded, flattened, or re-entrant shapes.

Manufacturing feasibility screening. Not all points in this 9D space correspond to printable geometries. Before any FEM evaluation, candidates are screened for manufacturing feasibility: minimum wall thickness compatible with the SLA printer resolution, maximum aspect ratio to avoid print failure or collapse during demolding, smooth profiles without sharp re-entrant features that would trap uncured resin, and a minimum contact-surface area to ensure stable platen engagement. This differs from much of the prior capacitive literature, where manufacturability is usually handled by choosing a convenient process—such as replica molding, texture transfer, or laser ablation—after the geometry concept has already been selected, rather than by embedding printability constraints directly inside the search itself [21, 29, 108]. These constraints are encoded as hard bounds

in the parameterization and as a feasibility filter in the sampling pipeline, so that simulation budget is not spent on unprintable designs. Figure 3.15 shows representative feasible designs that survived this screening, illustrating the range of accessible profiles from near-frustum to more strongly reshaped cells while preserving printable footprints and smooth contact evolution.

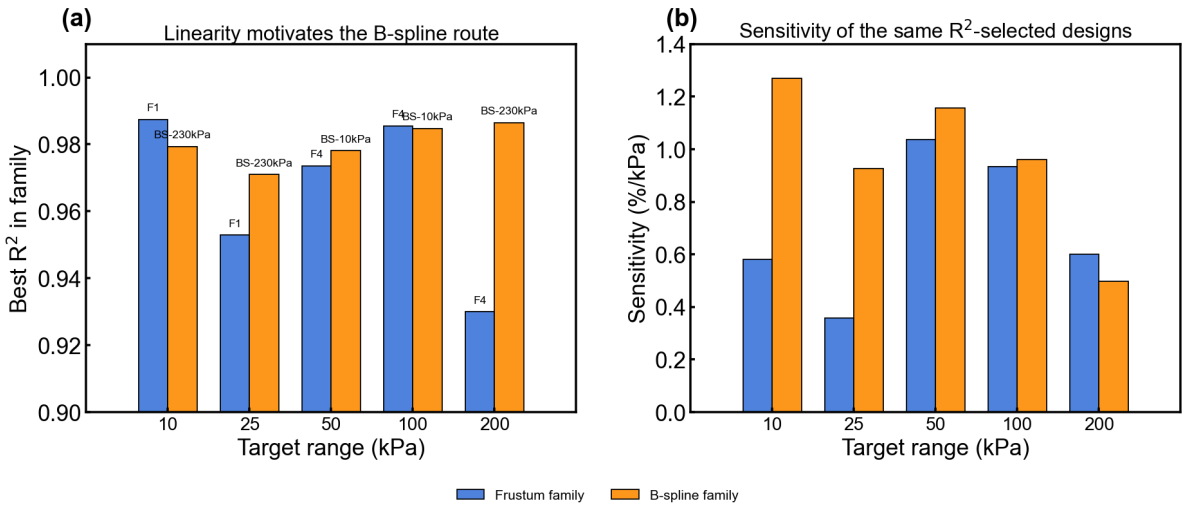


Figure 3.14: Geometry family versus target range. (a) Best linearity within frustum and B-spline families across several pressure ranges. For narrow ranges, frustums achieve high linearity; for wider ranges, B-spline freedom sustains linearity by reshaping deformation and delaying saturation. (b) Sensitivity of best-linearity designs.

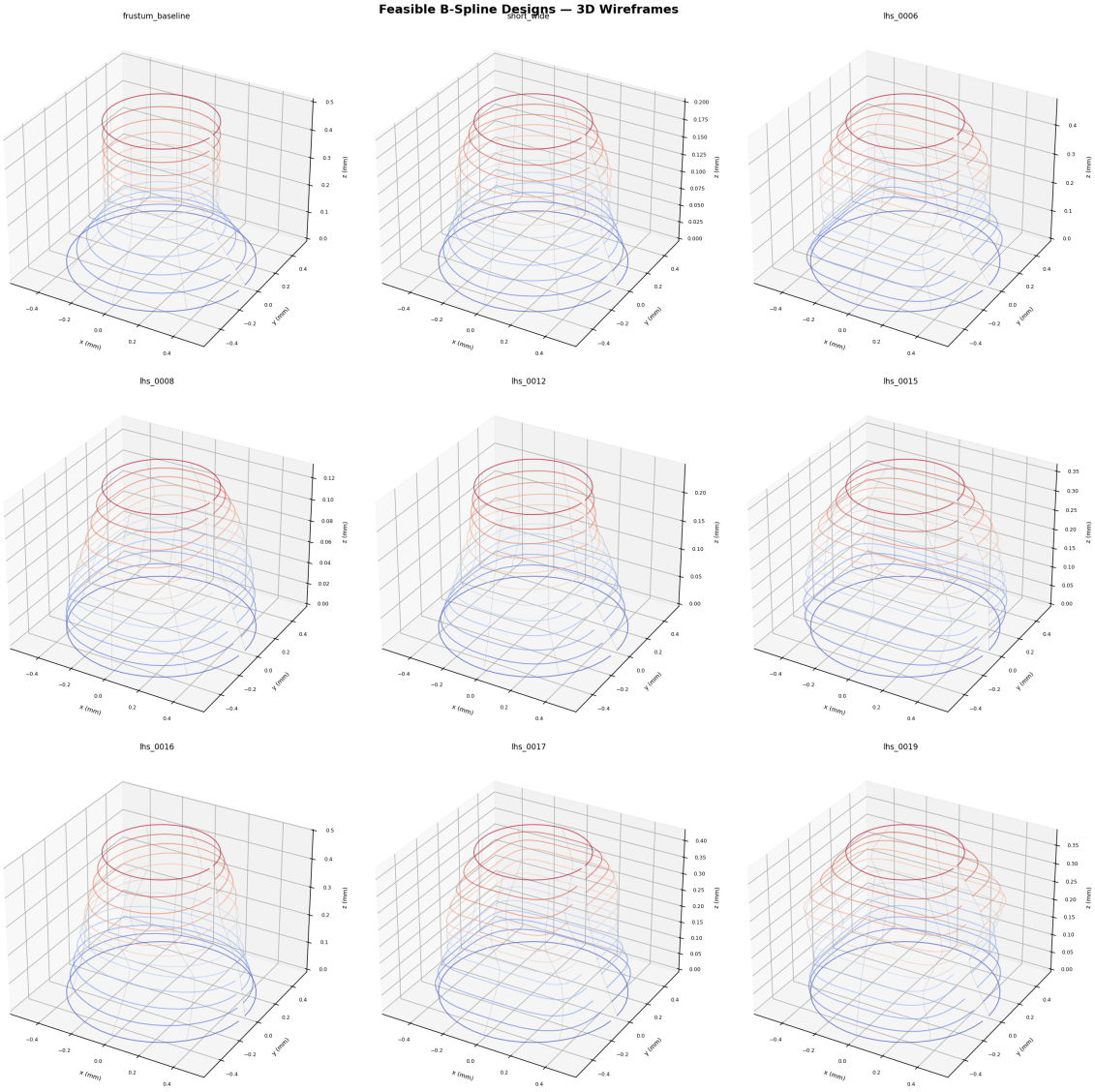


Figure 3.15: Representative feasible 3D wireframes from the B-spline geometry family, spanning near-frustum to strongly reshaped profiles while preserving manufacturable footprints and smooth transitions.

3.6.4 Active Learning and Surrogate Modeling

The 9-dimensional B-spline design space cannot be explored by the structured grid sweep used for the frustum family in Section 3.5. A grid with even 5 levels per dimension would require $5^9 \approx 2 \times 10^6$ FEM evaluations, each taking minutes—a computational budget that is neither practical nor necessary, since large regions of the space are either infeasible or produce similar mechanical responses. A smarter sampling strategy is needed: one that concentrates FEM evaluations where they are most informative and avoids redundant runs in well-characterized regions.

Latin hypercube seeding. The surrogate training begins with a space-filling Latin hypercube sample (LHS) that provides initial coverage of the feasible design space. LHS ensures that each dimension is sampled uniformly without the combinatorial explosion of a full grid, producing an initial dataset that is diverse enough to train a preliminary surrogate but small enough to be computationally tractable. Infeasible candidates (those failing the manufacturing screening of Section 3.6.3) are filtered before FEM evaluation, so the initial dataset contains only printable, mechanically evaluable designs.

Not all candidate geometries generated by the sampling strategy are physically realizable. Before FEM evaluation, each candidate is screened against manufacturing constraints derived from the Formlabs SLA printing specifications for the Silicone 40A resin: minimum feature size, maximum unsupported overhang angle, base-area containment, cross-sectional continuity (no self-intersections), and smoothness of area transitions along the build height. Figure 3.16 shows the distribution of rejection reasons within a representative active-learning iteration, where 16 of 35 generated candidates were rejected before simulation, leaving 19 feasible designs. The dominant failure modes—overhang violations and base-area exceedances—reflect the inherent tension between shape richness and printability in the B-spline family. This rejection rate confirms that the parameterization spans a broad shape space and that the feasibility filter excludes non-manufacturable candidates. Of the 19 feasible designs, 9 were selected for FEM evaluation in this representative iteration, so the active-learning selection concentrates FEM budget on the most informative candidates.

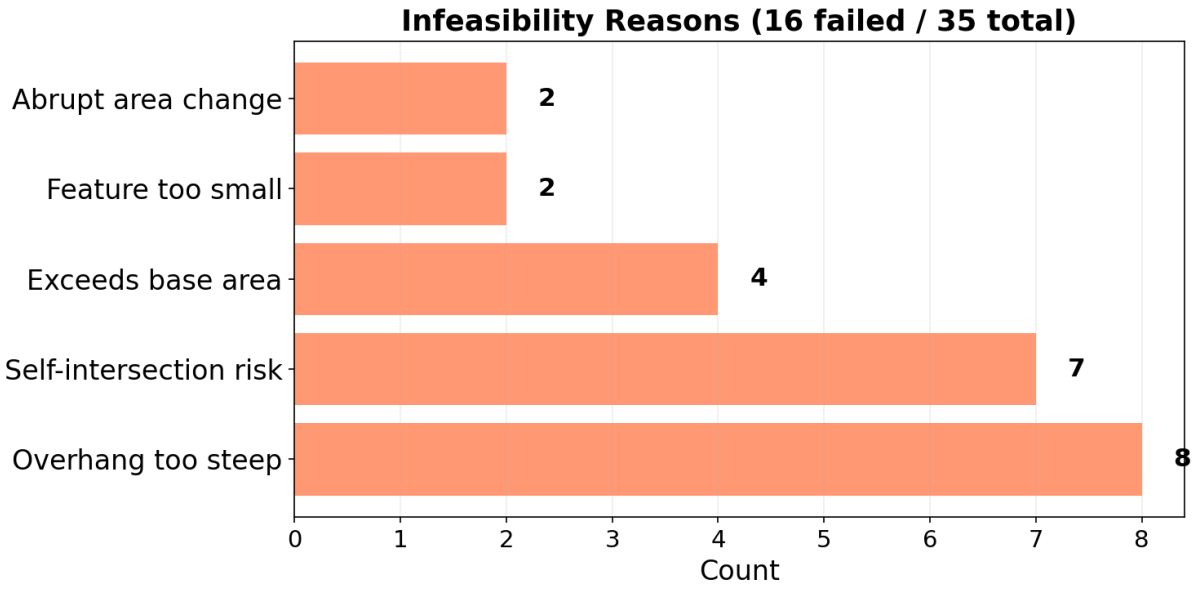


Figure 3.16: Representative infeasibility screening results during B-spline active learning. Candidates are rejected before FEM if they violate printable bounds: minimum feature size, overhang limits, base-area containment, continuity, or smoothness. Here, 16 of 35 candidates were filtered, with overhang and self-intersection violations dominant. Screening preserves FEM budget for manufacturable designs.

Active learning for targeted refinement. After the LHS seed, subsequent FEM evaluations are selected by an active-learning loop rather than by random or grid-based sampling. At each iteration, the current surrogate model is used to predict the mechanical response across a large pool of unevaluated candidate geometries. The candidates where the surrogate is most uncertain—or where the predicted response is most promising for the downstream optimization—are prioritized for the next batch of FEM runs. The surrogate is then retrained on the expanded dataset, and the cycle repeats.

This strategy is efficient because it allocates simulation budget adaptively. Regions of the design space that are already well-predicted receive no additional runs, while regions near the feasibility boundary, near performance transitions, or in under-sampled corners of the 9D space receive targeted evaluation. In practice, the active-learning loop produced a dataset of approximately 76 feasible designs at the exploratory mesh resolution (mesh $= 0.3$) and 41 designs at the production mesh resolution (mesh $= 0.1$), which was sufficient to train surrogates with high predictive accuracy across the feasible B-spline space.

Surrogate models. The surrogate architecture follows the same pattern as the frustum surrogates in Section 3.5: regression models trained on the mapping from (geometry descriptors, normalized strain $\varepsilon = \delta/h$) to (contact area, force). Three model types were evaluated: gradient-boosted regression (GBR), random forest (RF), and a small artificial neural network (ANN). GBR was adopted as the production surrogate based on consistently high cross-validated performance, while the ANN served as a sanity check. For the production mesh = 0.1 dataset, typical surrogate accuracy was $R^2 > 0.95$ for contact area and $R^2 > 0.92$ for force, consistent with the frustum-family results and sufficient for reliable array-level optimization.

Sliced capacitance model. Unlike the iontronic transduction model, which maps contact area directly to capacitance, the conventional capacitive transduction requires tracking how the dielectric gap evolves along the full height of the microstructure under compression. A simple volume-fraction approximation—treating the entire cell as a single effective dielectric thickness—was found to overestimate the initial capacitance by roughly 25% because it does not account for how the polymer fill varies spatially between the electrodes.

To correct this, a sliced capacitance model was implemented. The model discretizes the deformed microstructure into thin horizontal slices, computes the local polymer-to-air ratio in each slice from the FEM-predicted deformation field, and integrates the resulting series capacitance over the full stack height. This correction reduced the initial-capacitance prediction error from approximately 25% to approximately 5% in representative comparisons, making the model accurate enough to distinguish between candidate designs during optimization. The sliced model operates on the same FEM outputs (deformed geometry and contact state at each displacement step) that the surrogate already predicts, so it adds negligible computational cost once the surrogate is trained.

3.6.5 Range-Tunable Optimization Results

With the surrogates and sliced capacitance model in place, the final step of the framework is to search over multi-tier array configurations for a given set of user requirements. The optimizer uses differential evolution to explore the combinatorial space of tier assignments—which B-spline geometry to place in each tier position, and how many cells of each tier to include—subject to the sensor footprint constraint and manufacturing bounds. The objective function is a weighted combination of linearity (R^2 of the predicted $C(P)$ curve over the target range) and sensitivity ($\Delta C/C_0$ at the maximum target pressure), with a designer-specified linearity–sensitivity weighting. The optimizer uses differential evolution

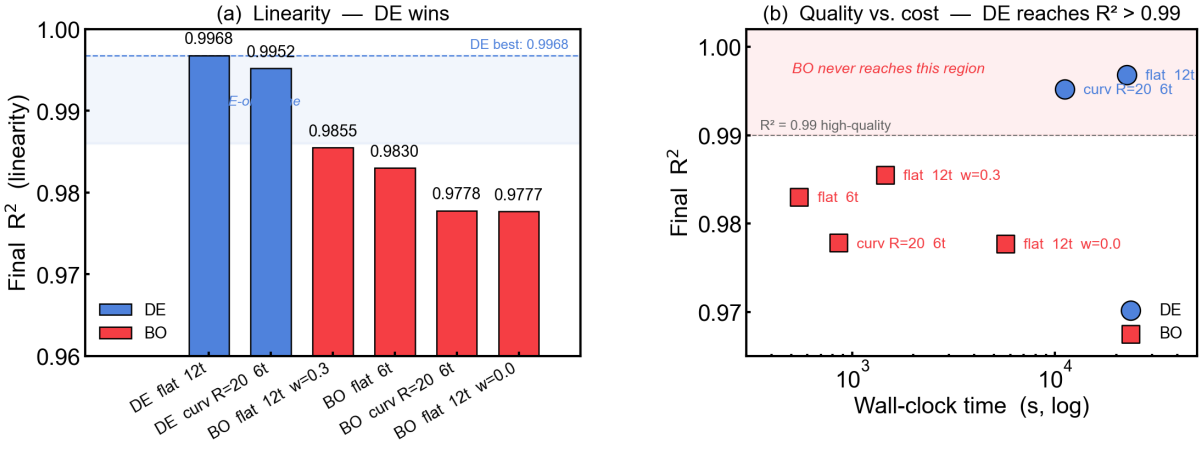


Figure 3.17: Representative optimizer comparison for range-tunable design. (a) Final linearity achieved by differential evolution (DE) and Bayesian optimization (BO). (b) Final solution quality versus wall-clock time. DE consistently reached better solutions and exceeded $R^2 = 0.99$ threshold, motivating its use as the default optimizer.

(DE), a population-based derivative-free search, because the decoded array objective is piecewise, non-smooth, and interrupted by infeasibility penalties that violate the smooth response-surface assumptions underlying standard Bayesian optimization (BO) acquisition functions. Figure 3.17 confirms this on the thesis-specific frustum studies: DE consistently returned higher final linearity than BO and was the only method to enter the $R^2 > 0.99$ regime within comparable wall-clock budgets. The point is not that DE is universally superior, but that the penalized, mixed discrete–continuous objective used here behaves more like a rugged engineering search landscape than the smooth surfaces where BO is typically strongest. DE population size was set to $15 \times d$ where d is the number of continuous design variables, with mutation factor $F = 0.8$ and crossover probability $C_r = 0.9$; convergence was declared when the relative change in the population's best objective fell below 10^{-5} over 100 consecutive generations.

Figure 3.18 summarizes this optimization loop in its thesis-specific B-spline form. At the array level, the design variables are no longer just the single-cell B-spline descriptors; they include one geometry block per tier together with fractional tier assignments that are later decoded into integer cell counts. Those decoded tiers are then passed through three stages: surrogate-based forward simulation of $C(P)$, hard feasibility screening on the predicted response, and scalar objective evaluation with a separate structural penalty. The important point is that the optimizer never searches directly in terms of one fixed geom-

etry recipe. It searches over a high-dimensional array description, converts that description into a printable tier layout, evaluates the predicted response over the target pressure range, rejects degenerate solutions immediately, and then updates the design population until convergence. This separation between hard infeasibility and soft penalty keeps the search efficient: physically invalid or numerically degenerate designs are discarded outright, while mechanically awkward but still printable designs remain searchable and are simply discouraged by the objective rather than removed from the design space entirely.

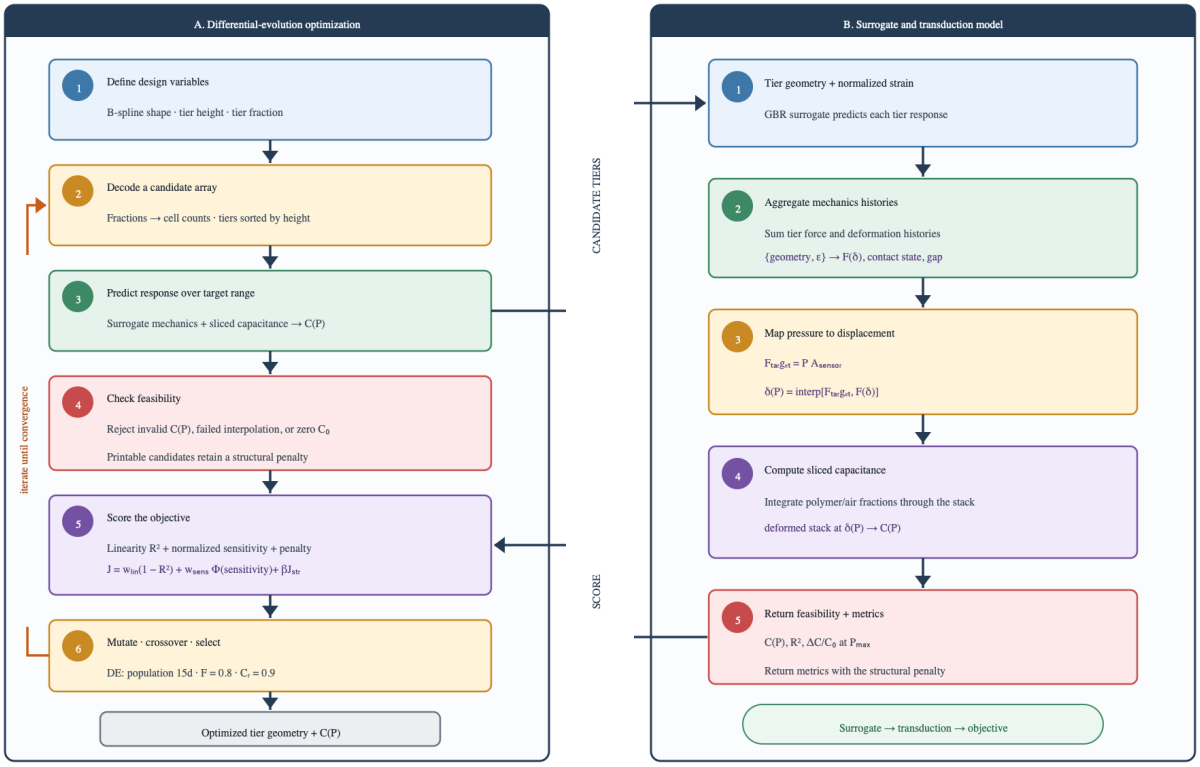


Figure 3.18: B-spline array optimization pipeline. Differential-evolution search operates on B-spline shape parameters, tier heights, and fractional assignments. Variables are decoded into a discrete array, evaluated by surrogate-plus-sliced-capacitance model, checked against infeasibility criteria, and scored with a weighted objective and structural penalty.

Range tunability is demonstrated by the different optimal arrays obtained from the same trained surrogates when the target pressure window is changed. Figure 3.19 compares three such solutions from the same B-spline search space: a 0–10 kPa design optimized for

linearity, a 0–10 kPa *retargeting-comparison design* optimized with a weighted linearity–sensitivity objective, and a broader 0–230 kPa design. The low-range designs preserve $R^2 \approx 0.998$ over 0–10 kPa, but the retargeting-comparison design increases low-pressure gain from 3.9% to 6.6% $\Delta C/C_0$ at 10 kPa relative to the linearity-only design, by accepting a different tier architecture. By contrast, the 0–230 kPa design redistributes both tier heights and tier populations toward later engagement, sacrificing low-range gain in order to maintain a usable monotonic response across the broader range.

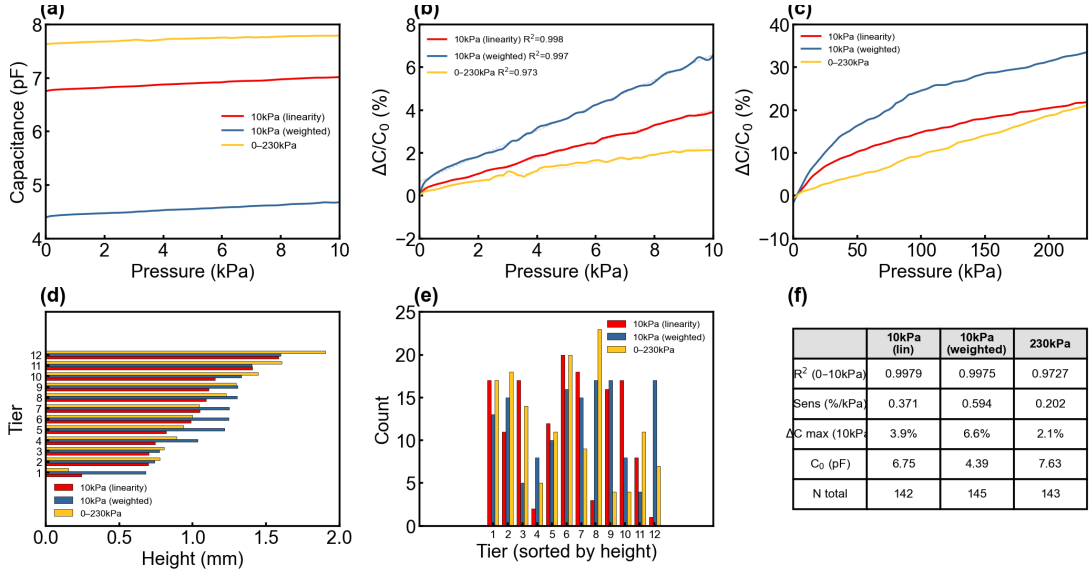


Figure 3.19: Range-specific optimized B-spline arrays from the same surrogate and framework. (a) Baseline capacitance for three designs: 0–10 kPa (linearity-optimized), 0–10 kPa (weighted linearity–sensitivity), and 0–230 kPa. (b) Low-range response (0–10 kPa). (c) Full-range response (0–230 kPa). (d–f) Optimized tier heights, cell counts, and summary metrics showing how target range and weighting lead to different arrays.

Figure 3.20 then shifts from *retargeting* to *mechanism*. It traces one representative high-range study targeting 0–200 kPa on a 20×20 mm pad, starting from a single repeating tier and ending with an optimized 12-tier array. Linearity improves from $R^2 = 0.876$ for the single-tier baseline to $R^2 = 0.977$ for 12 uniform tiers, and then to $R^2 = 0.999$ after optimization, showing that tier count alone is not sufficient; the height distribution also matters.

The later panels explain why. Shorter, more compliant tiers engage first and contribute

most of the low-pressure response, while taller tiers are introduced more selectively to delay saturation at higher loads. The baseline single-tier response deviates from a linear fit by up to 20%, whereas the optimized array remains within approximately ±1% across the full range. In other words, Figure 3.19 shows that different pressure windows require different arrays, while Figure 3.20 shows how progressive engagement makes one such optimized array nearly linear.

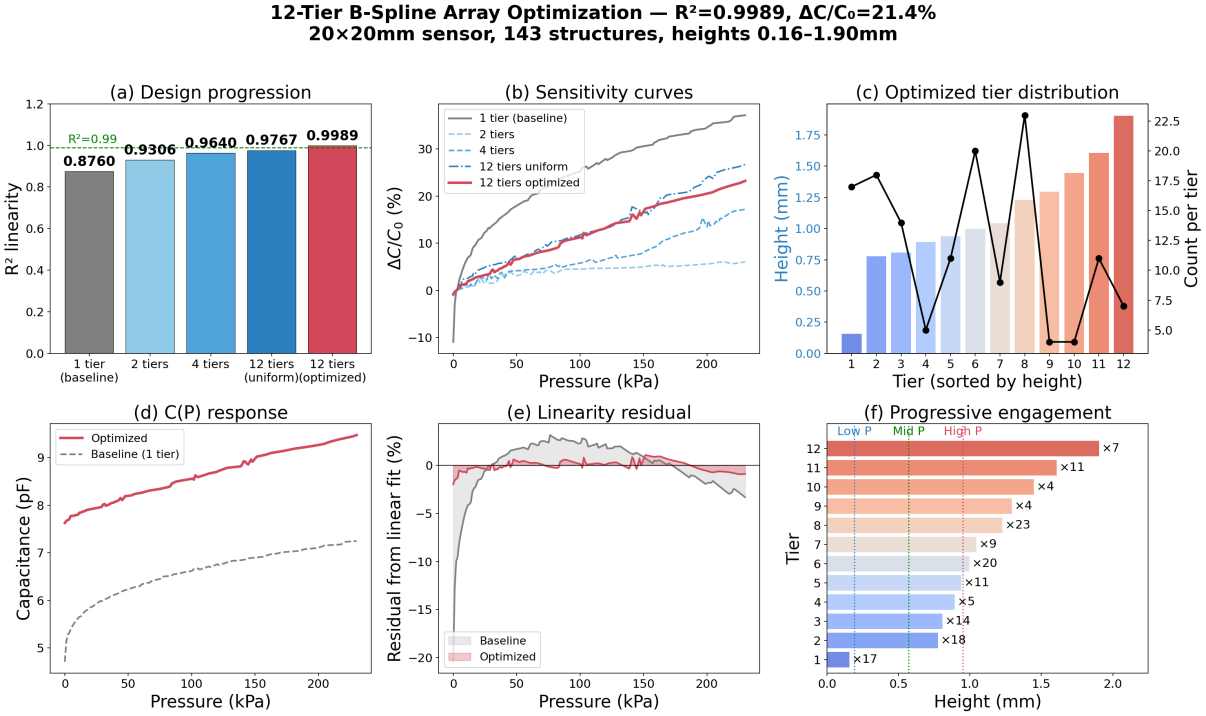


Figure 3.20: Design progression from single-cell baseline to optimized 12-tier array targeting 0–200 kPa. (a) Linearity improves from $R^2 = 0.876$ to 0.999. (b) Sensitivity curves: single-tier saturates below 50 kPa; optimized array remains linear across full range. (c) Non-uniform tier heights with cell counts. (d) Absolute capacitance: optimized design nearly linear. (e) Residual from linear fit: baseline deviates up to 20%, optimized design within ±1%. (f) Progressive-engagement map showing tier engagement sequence.

For the final optimized design targeting 0–10 kPa with equal linearity/sensitivity weighting on a 20×20 mm pad—distinct from the retargeting-comparison design discussed above—the optimizer converged to a 9-tier array with tier heights ranging from approximately 0.4

to 1.5 mm. The predicted response achieved a linearity of $R^2 = 0.9958$ with a maximum normalized response of $\Delta C/C_0 = 21.4\%$. The optimized design remained physically interpretable and manufacturable—the tier profiles were smooth, the aspect ratios were within printable bounds, and the progressive engagement sequence was evident in the predicted contact-area histories.

3.6.6 Fabrication and Experimental Validation Protocol

The optimized capacitive designs were fabricated as solid-state silicone dielectric stacks so that the computational predictions could be compared against physical pressure–capacitance measurements. The printed dielectric layer used Formlabs Silicone 40A resin and the optimized multi-tier array geometry exported from the framework pipeline. After printing and post-processing according to the material workflow described in Chapter 2, the dielectric layer was assembled between flexible conductive-fabric electrodes. The same electrode material was used on both sides of the dielectric to avoid introducing an additional coating or composite-processing variable into this validation step.

Physical validation focused on whether the model-guided designs preserved the intended monotonic response shape and relative ordering between variants. Each fabricated sensor was loaded under normal compression using the pressure-characterization fixture described in Chapter 2. Unless otherwise stated, capacitance was measured with the Keysight E4980AL/032 LCR meter at 1 kHz with 1 V AC excitation in Cp/Rp mode. The applied force was converted to nominal pressure using the flat-ended indenter area used for the corresponding experiment. The same acquisition script recorded the LCR output and the force-stand reading for each loading step so that capacitance could be plotted directly against nominal pressure.

Table 3.6 summarizes the computational and physical validation settings for the solid capacitive route.

Table 3.6: Solid capacitive route: design, fabrication, and validation settings.

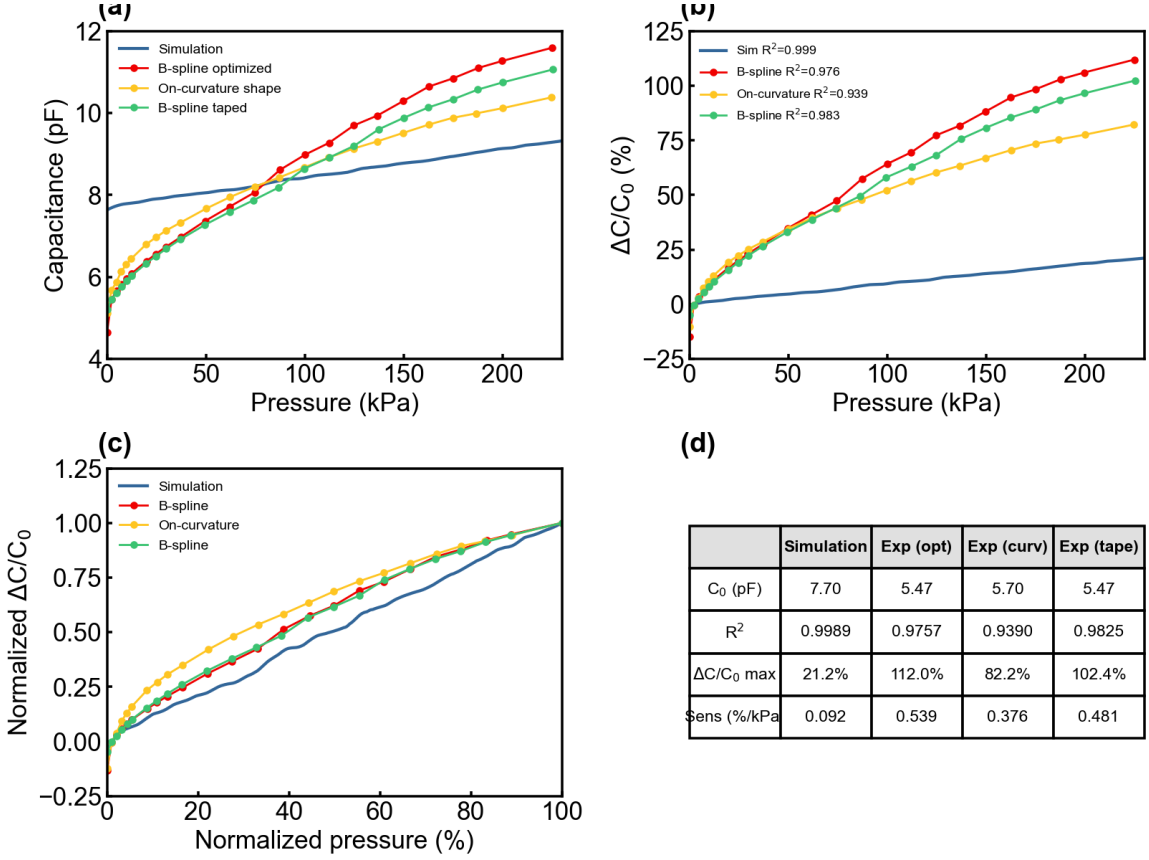
Parameter	Setting used in this thesis
Dielectric material	Formlabs Silicone 40A resin, using the hyperelastic material model calibrated in Chapter 2
Electrode material	Flexible conductive fabric electrodes on the top and bottom sides of the dielectric stack

Table 3.6: Solid capacitive route: design, fabrication, and validation settings (continued).

Parameter	Setting used in this thesis
Geometry family	B-spline/superellipse profile with 8 shape coefficients plus height, decoded into multi-tier arrays
Target footprint	20 mm × 20 mm for the primary optimized designs
Main target pressure ranges	0–10 kPa and broader-range designs up to 0–230 kPa, depending on the optimization study
FEM dataset	Active-learning dataset with exploratory mesh resolution (mesh = 0.3) and production mesh resolution (mesh = 0.1)
Dataset size	Approximately 76 feasible exploratory designs and 41 production-resolution designs
Surrogate model	Gradient-boosted regression used as the production surrogate, with RF and ANN models used as comparison or sanity checks
Electrical model	Sliced capacitance model using FEM-predicted deformed geometry, contact state, and local polymer/air fraction
Optimizer	Differential evolution with population size $15d$, mutation factor $F = 0.8$, crossover probability $C_r = 0.9$, and stopping criterion based on relative best-objective change below 10^{-5} over 100 generations
Readout	Keysight E4980AL/032 LCR meter, 1 kHz, 1 V AC excitation, Cp/Rp mode
Mechanical loading	Mark-10 F305 force stand with 100 N load cell and a 1.5 cm-diameter flat-ended indenter
Fabricated validation cases	Primary optimized array plus curvature and taped-electrode variants shown in Fig. 3.21; fabricated validation count $n = 3$. Curvature and taped-electrode cases were treated as different test conditions on the same sensor-design family rather than as separate geometry families
Loading schedule and repeats	Two loading modes were used: preset-point loading, where the Mark-10 stage stopped at individual target pressure points until the force and capacitance readings stabilized, and continuous loading–unloading sweeps. Each condition was repeated three times. No fixed dwell duration beyond stabilization at the preset pressure points was recorded

The experimental comparison in Fig. 3.21 should therefore be interpreted as a validation of design ranking and response shape rather than as an exact field-solver prediction of absolute capacitance. Fringing fields, electrode conformality, local fabric compression, and compression-dependent dielectric properties are not fully represented in the reduced sliced-capacitance model. The validation criterion for this route was consequently that the fabricated devices remained monotonic, approximately linear over the intended range, and ordered consistently with the model-guided design selection.

Figure 3.21 compares the predicted and measured responses for several B-spline-derived designs, including the primary optimized array and variants tested under curvature and taped-electrode conditions. The experiments consistently show larger normalized gains than the simplified model prediction. This discrepancy is expected: the sliced capacitance model captures the dominant geometric effects but does not account for fringing fields, electrode conformality, or compression-induced permittivity changes. The model nonetheless preserves the monotonic response shape and the relative ordering between design variants, which is sufficient for its role in guiding design selection. The model is intended to rank candidates correctly and identify the right region of the design space, not to predict absolute capacitance values to within a few percent.



	Simulation	Exp (opt)	Exp (curv)	Exp (tape)
C_0 (pF)	7.70	5.47	5.70	5.47
R^2	0.9989	0.9757	0.9390	0.9825
$\Delta C/C_0$ max	21.2%	112.0%	82.2%	102.4%
Sens (%/kPa	0.092	0.539	0.376	0.481

Figure 3.21: Simulation and experiment for selected B-spline-derived designs. (a) Absolute capacitance–pressure curves. (b) Normalized $\Delta C/C_0$ responses with linearity values. (c) Normalized responses. Experiments show larger gains than model but preserve monotonic response and variant ordering.

3.6.7 Interactive Web-Based Design Tool

To make the framework accessible beyond the immediate thesis experiments, it was implemented in an interactive design tool (Figure 3.22). The tool accepts a target pressure window, sensor footprint, tier count, and linearity–sensitivity weighting, then returns an optimized array configuration, its predicted C–P response, and a tier-level geometry summary.

The requirements interface is decoupled from the mechanics, surrogate, and transduc-

tion layers, allowing additional geometry families or sensing mechanisms to be incorporated without changing the design workflow.

The larger signal gain of the iontronic route makes it the primary glove-facing design; the capacitive sensor's contribution is the evidence that the same framework and optimizer generalise to a fundamentally different transduction mechanism and material set without modification. The boundary of this claim is important. The microwave resonator in Section 3.3 was an early down-selection prototype and was not designed with the optimization framework developed in this chapter. The framework is experimentally demonstrated here only for the two local-readout routes: the PVA/H_3PO_4/PVP hydrogel iontronic sensor and the solid silicone capacitive sensor. Its broader transferability rests on replacing the mechanism-specific transduction model while retaining the shared geometry parameterization, nonlinear mechanics, surrogate modeling, and range-aware optimization layers; mechanisms outside these two demonstrated routes would require new transduction calibration and experimental validation before equivalent performance claims could be made.

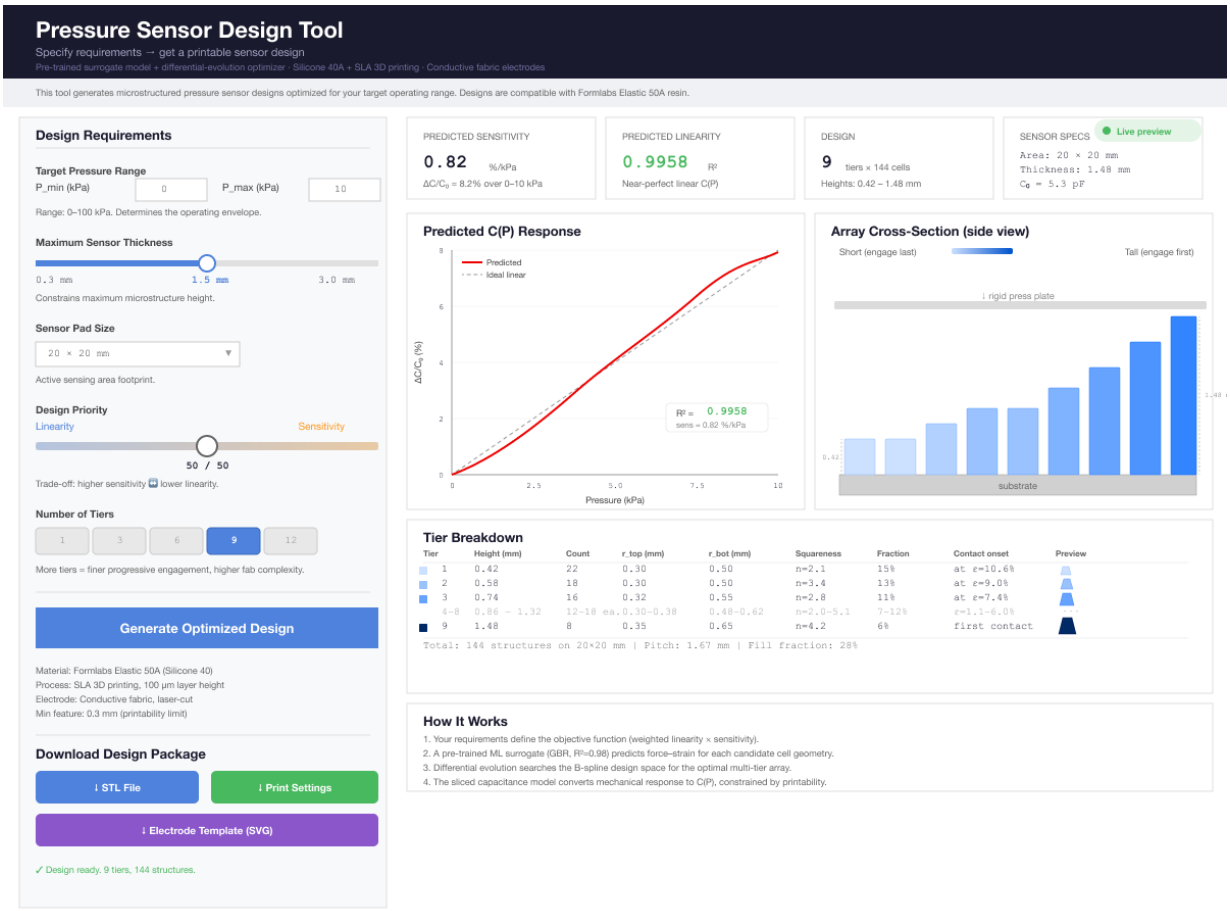


Figure 3.22: Interactive pressure-sensor design tool. The interface accepts a target pressure range, pad size, linearity–sensitivity weighting, and tier count; it returns an optimized array, predicted $C(P)$ response, and tier-level geometry summary. Example: 0–10 kPa on a 20×20 mm pad with 9 tiers, $R^2 = 0.9958$.

Chapter 4

Pillar-Structured Capacitive Bending Sensor for Wide-Range Joint-Angle Sensing

4.1 Background and Motivation

Chapter 1 identified glove-based joint kinematic sensing as a core gap in current OTG platforms: most existing approaches transduce local strain rather than anatomical joint rotation, making their outputs sensitive to mounting tension, placement variability, and donning repeatability. This chapter addresses that gap directly by developing a bending sensor whose transduction mechanism is intrinsically linked to joint curvature rather than surface strain.

The specific sensing challenge is that joint angle must be estimated reliably across users with different hand anatomy, under repeated donning, and without per-user mechanical refitting. Lab-based solutions such as optical motion capture provide accurate reference measurements but are not wearable. Among wearable modalities, resistive strain sensors and conventional capacitive flex sensors are the most widely deployed, yet both couple strongly to placement-dependent strain states rather than to the joint rotation itself — the core limitation identified in Chapter 1.

4.1.1 Bending and joint-angle sensing technologies

Wearable hand kinematic monitoring requires estimating joint angles, or functionally equivalent kinematic descriptors, under OTG conditions. The central difficulty is that most reported "bending sensors" do not directly measure joint angle; instead, they transduce local strain or curvature. In a wearable glove, however, local deformation is influenced not only by joint rotation, but also by soft-tissue motion, glove stretch, pretension, and sensor placement relative to the joint axis. As a result, the mapping from sensor signal to joint angle is often neither unique nor stable across users or across repeated donning [5, 7].

Resistive strain and bending sensors are widely used because they require relatively simple electronics and can be integrated into textiles or elastomers using conductive composites, thin films, or crack-based conductive networks. Their main strength is high strain sensitivity, as illustrated by engineered microstructures such as overlapping carbon nanotube networks that produce ultrahigh gauge factors under deformation [119]. Early glove systems based on resistive bend sensors demonstrated that sensor output is sensitive to the longitudinal position of the sensor relative to the joint centre, because the local curvature field is non-uniform across the finger segment and changes with joint geometry and soft-tissue distribution [120]. This placement dependence is compounded by skin stretch: the measured resistance reflects a combination of joint rotation, local skin sliding, substrate stretch, and fit-dependent pretension, so the same joint angle can produce different strain states across users or even across repeated donning. Researchers have explicitly tried to decouple bending from stretching in sensor design precisely because skin-stretch contamination is a dominant source of error in glove-based angle estimation [30]. Even with sensor-level improvements, the full signal-to-angle mapping remains unstable across users, and recent glove systems based on stretch-sensitive transduction still require comprehensive motion-data calibration or model correction to reconstruct hand pose robustly across anatomies [31]. Consequently, resistive sensors often require substantial per-user calibration and may exhibit drift or reduced repeatability in OTG deployment [6, 27, 32].

Capacitive bending sensors offer an alternative to conductive-network strain sensing, but they still do not automatically measure joint angle directly. Reported capacitive strategies include continuous curvature sensors that use beam-model compensation for installation error and double-layer differential architectures that suppress common stretch effects between paired capacitors [95, 121]. These approaches improve interpretability, yet the measured capacitance still depends on how the structure deforms on the body; electrode layout and internal architecture therefore remain central to converting local deformation into a stable kinematic observable [122].

Liquid-metal embedded-channel and fiber-based sensors provide additional routes to

soft kinematic sensing. Liquid-metal conductors such as EGaIn embedded in elastomers can survive repeated bending without fatigue failure, and their geometry can be designed to encode multiple deformation modes into distinct electrical responses [123]. Optical, ionic, and inertial approaches have also been explored when electromagnetic immunity, multiplexing, or robustness are prioritized. However, for dense finger-joint sensing, these approaches typically introduce additional challenges in packaging, routing, environmental sensitivity, placement dependence, or signal interpretation [5, 3].

Across these mechanisms, the recurring problem is placement sensitivity. Because the measured response depends on the local deformation field, small offsets in sensor position relative to the joint axis can shift the sensor from a high-curvature region to a lower-curvature region, altering both sensitivity and the functional mapping between signal and joint angle. This is a major reason why strong benchtop bending performance often does not translate directly to wearable joint-angle estimation [6, 27]. Quantitatively, placement-induced signal variability of 15–30% has been reported in glove-based evaluations even when subjects are retrained on the same sensor, and cross-session repeatability often requires complete re-calibration [6, 7]. Instrumented gloves have been evaluated for hand-movement acquisition since the early 2000s, and mapping glove output to joint kinematics has remained a persistent systems challenge throughout [7]: even carefully calibrated systems struggle to maintain accuracy when the glove is re-donned or used by a different individual, and algorithmic correction has been proposed as a compensating measure [32]. For distal interphalangeal (DIP) and proximal interphalangeal (PIP) joints in particular, fit-dependent sensor placement errors are severe enough to question whether strain-gauge gloves can provide reliable kinematics without multi-size hardware [27]. Taken together, the evidence across resistive, capacitive, and other mechanism families points to a common root cause: when the transduction mechanism is sensitive to the local deformation field, any variation in sensor placement, glove fit, or skin mechanics introduces a systematic, anatomy-dependent error that calibration alone cannot eliminate.

The remaining distinction is therefore architectural rather than only modal: different bending sensors use different internal strategies to turn deformation into angle information. Prior designs have reduced stretch interference through segmented sensitive/insensitive resistive regions, analytical compensation in continuous capacitive curvature sensors, differential cancellation between stacked capacitors, or multi-channel strain decoupling [30, 95, 121, 124]. Table 4.1 positions the proposed pillar/air dielectric against these representative routes. The comparison highlights the intended distinction of this work: its dominant signal is generated by curvature-driven redistribution of air volume and electrode intrusion across a distributed cavity field, rather than by local tensile strain alone or by post hoc cancellation of stretch contamination.

A further modelling gap in existing capacitive bending sensors is the treatment of electrode deformation prior to any applied bending. Thin compliant electrodes spanning millimetre-scale air cavities can sag under gravity or residual lamination stress, reducing the available air gap and shifting the baseline capacitance before the sensor is ever loaded. This effect is cavity-geometry-dependent and grows rapidly with cavity span — ideally as the fourth power of span width for a simple beam — yet it is rarely accounted for in published sensitivity models. Ignoring sag can distort geometry comparisons and mislead the optimisation of cavity dimensions. Addressing this modelling gap is one of the contributions of this chapter (Section 4.3.2).

4.1.2 Design requirements for bending sensing

For bending and joint-angle sensing, the central requirement is not merely detection of deformation, but the generation of outputs that map meaningfully to joint angle over the range of motion of interest. Placement tolerance is a first-order requirement: the measured response depends on the sensor position relative to the joint axis and the local deformation field, so small offsets introduced by donning variability or anatomical differences can alter the effective mapping between signal and joint angle [6, 27].

A complementary requirement is an interpretable and monotonic response that remains calibratable over relevant joint motion. The bending sensor must also remain mechanically compatible with the wearable form factor: thin, compliant, and durable under repeated flexion cycles.

Among flexible sensing approaches, resistive strain sensors and glove-integrated capacitive sensors are prominent candidates, but both still face limitations for anatomy-robust angle estimation. Resistive sensors respond directly to surface strain, making their output sensitive to skin mechanics, glove tension, and mounting location [120, 30]; even recent designs that attempt to decouple bending from stretching rely on post-hoc calibration or modelling correction to recover consistent joint-angle estimates across users [31, 32]. These limitations motivate a different design philosophy: rather than attempting to correct for placement and stretch contamination after the fact, the sensor architecture itself should be designed so that its output is governed by the global bending angle rather than by local surface strain. In this work, we propose a capacitive bending sensor that uses microstructured pillars and air cavities to produce a response driven by the redistribution of air-cavity volume under bending — an intrinsically angle-centric transduction mechanism that reduces sensitivity to placement variability and skin-stretch contamination from the outset.

Table 4.1: Representative bending-sensor architectures and their relation to the pillar/air capacitive design proposed in this work.

Representative architecture	Dominant measured quantity	Strategy against stretch / placement error	Main residual limitation	Relation to this work
Resistive bend strip / Oess et al. [120]	Local resistance change from local strain	No intrinsic suppression; placement optimized empirically	Output varies with longitudinal sensor position relative to the joint	Establishes the placement-sensitive baseline problem
Stretch-insensitive resistive sensor / Shen et al. [30]	Strain in patterned sensitive regions	Sensitive / insensitive segmentation reduces stretch interference	Signal remains path-strain based	Reduces stretch contamination, but does not use an angle-centric cavity mechanism
Continuous capacitive curvature sensor / Li et al. [95]	Curvature-induced capacitance change in a continuous capacitor	Euler-beam compensation for installation error and one-time calibration	Depends on the assumed installation model	Closest continuous capacitive comparator
Differential double-layer capacitive sensor / Goto et al. [121]	Difference between upper and lower capacitances	Common-mode stretch cancellation between paired capacitors	Requires stacked channels and differential readout	Direct capacitive comparator for stretch suppression
Multi-channel strain-decoupling sensor / Song et al. [124]	Multiple directional strain channels	Mathematical decoupling of bending and tensile components	Added channels and inference complexity	Alternative route to size and strain compensation
This work: pillar/air cavity capacitive sensor	Distributed cavity-volume redistribution under bending	Internal geometry biases the response toward curvature-driven electrode intrusion	Controlled cross-user placement validation remains outstanding	Structural route studied in this chapter

4.2 Sensor Architecture and Fabrication

4.2.1 Multilayer structure and design concept

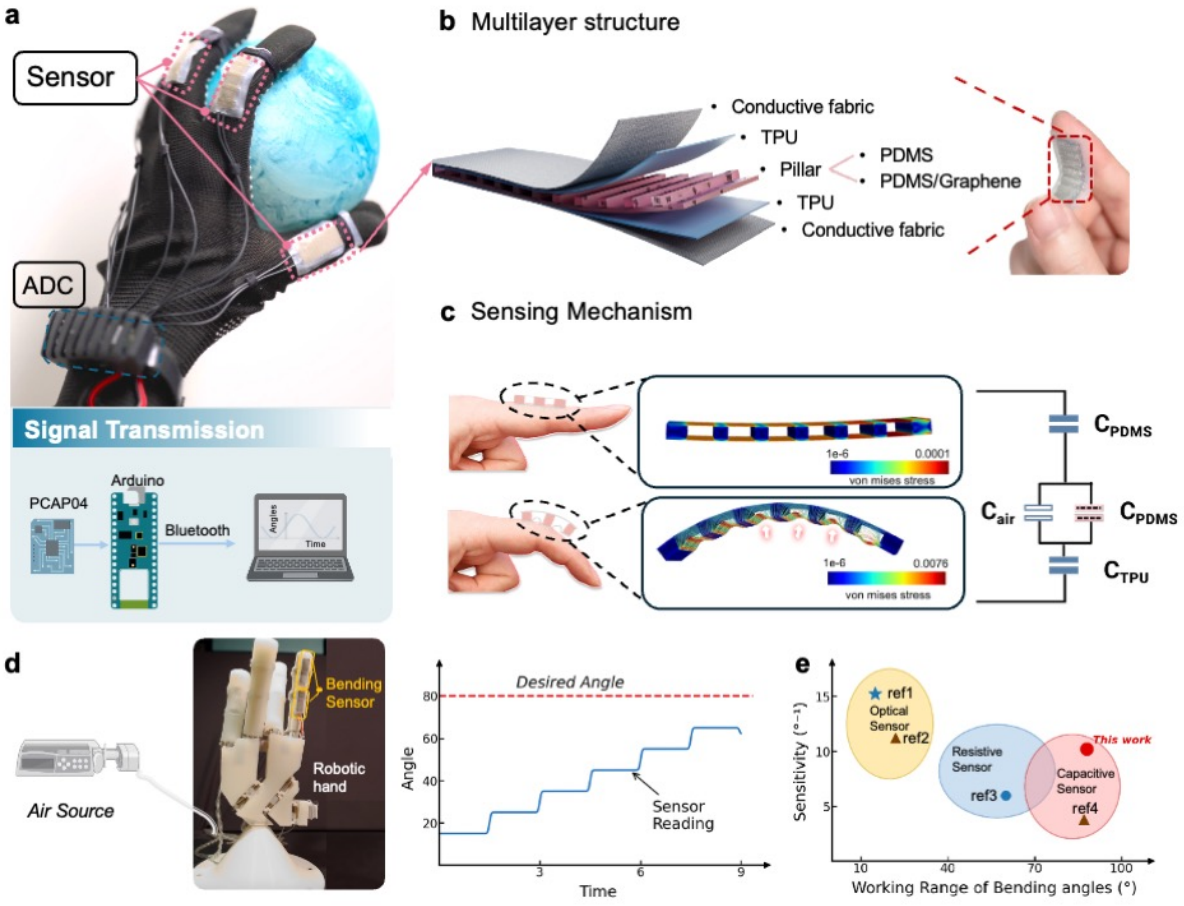


Figure 4.1: Sensor concept and system overview. (a) Fabricated sensor and readout board. (b) Exploded schematic of multilayer stack: conductive fabric electrodes, PDMS pillar/cavity dielectric, TPU bonding layer. (c) Sensing mechanism: bending drives upper electrode into cavities, increasing effective permittivity. (d–f) Angle-centric response comparison, system signal path, and robotic-finger application.

As shown in Fig. 4.1(a–b), the sensor comprises a multilayer stack including conductive fabric electrodes and a microstructured dielectric layer formed by pillar arrays with engi-

neered air cavities. During bending, the upper electrode preferentially deflects into the air gaps (Fig. 4.1c), reducing the effective electrode separation in regions that were previously air-filled. Because air and the dielectric pillars have different permittivities, this produces a measurable capacitance change that correlates with bending angle.

A key design objective is for the transduction to be governed by geometric rearrangement of the air fraction, thereby reducing the influence of uncontrolled tensile strain in the electrode stack. The proposed structure makes the macroscopic, predictable rearrangement of air cavities under bending the dominant response, reducing coupling between joint kinematics and parasitic surface strains. This supports robustness to placement and anatomical location (e.g., finger, knee), provided the sensor experiences bending curvature over the pillar region.

This architecture differs from the representative designs summarized in Table 4.1 through its distributed internal dielectric field: bending progressively redistributes the air fraction and permits electrode intrusion over many cavities. The analytical model developed in Sections 4.3.1 and 4.3.2 therefore treats cavity geometry, dielectric contrast, and pre-bending sag as architectural variables that shape the signal before any calibration model is applied.

4.2.2 Fabrication

Graphene/PDMS dielectric. PDMS (Sylgard 184, Dow Corning, USA) was used as the nanocomposite matrix, and graphene nanoplatelets (CheapTubes, USA) were used as the filler. To prepare the graphene/PDMS dielectric, graphene was first dispersed in acetone and then added to the PDMS base agent. The mixture underwent 2 h of stirring followed by 2 h of sonication before the curing agent was added. The final mixture was poured into the mold and cured in an oven at 80°C for 2 h.

Structural mold and assembly. The pillar mold was designed in Blender and fabricated using a Formlabs Form 3 printer with clear resin. A TPU adhesive film (Bemis) was used to bond the conductive fabric electrodes to the PDMS pillar layer. The multilayer stack was assembled and bonded under a heat press for 2 min at 150°C. Unless otherwise specified, the sensor footprint was 10 mm × 30 mm.

4.3 Sensing Mechanism and Analytical Model

4.3.1 Effective-medium capacitance model

We model the multilayer stack as a series combination of a structured sensing layer and comparatively constant parasitic layers from the base and adhesive films. Because the latter vary only weakly during bending, the bending-induced signal is dominated by the pillar/air dielectric layer. Using an effective-medium approximation for that structured region,

$$C_s = \frac{\varepsilon_0 A}{d}\varepsilon_{\text{eff}}, \qquad \varepsilon_{\text{eff}} = \varepsilon_d - (\varepsilon_d - \varepsilon_{\text{air}})\phi_{\text{air}}, \tag{4.1}$$

where $A = LH$ is the projected sensing area, d is the mean electrode separation within the structured layer, ε_d and ε_{air} are the dielectric constants of the pillar material and air, and ϕ_{air} is the air-volume fraction retained between the electrodes.

During bending, the upper electrode progressively intrudes into the cavities, reducing both the mean separation d and the air-volume fraction ϕ_{air}. To first order, the corresponding normalized capacitance change can therefore be expressed as

$$\frac{\Delta C_s}{C_{s,0}} \approx -\frac{\Delta d}{d_0} - \frac{\varepsilon_d - \varepsilon_{\text{air}}}{\varepsilon_{\text{eff},0}}\Delta\phi_{\text{air}}, \tag{4.2}$$

where subscript 0 denotes the undeformed state. Because bending produces both $\Delta d < 0$ and $\Delta\phi_{\text{air}} < 0$, each term contributes positively to the capacitance increase.

Design implication. This form makes explicit that increasing dielectric contrast and manipulating the retained air fraction through pillar spacing and geometry can significantly increase sensitivity. It also clarifies why this sensing mechanism is more angle-dominant than conventional surface-strain-dominated flex sensors: the principal signal is produced by geometry-driven redistribution of the internal dielectric structure, rather than by strain at the mounting interface alone.

4.3.2 Electrode sag correction

A practical complication in cavity-based capacitive bending sensors is that the upper electrode can deform into the cavity volume even in the absence of externally applied bending. In thin, compliant electrodes, gravity and residual stresses from lamination can produce an

initial "sag" of the electrode membrane between adjacent pillars. This reduces the available air gap and increases the baseline capacitance C_0, thereby lowering the apparent normalized sensitivity C/C_0 under bending. Importantly, the sag effect is geometry-dependent: larger cavity spans (greater pillar spacing) generally increase membrane deflection for a given electrode stiffness, and therefore can mask or distort the intended differentiation between designs with different cavity widths.

To interpret simulation sweeps and to separate geometric transduction from electrode mechanics, we account for electrode sag using a simple beam model for a strip spanning one cavity of width d and thickness t_e. For a simply supported membrane, the maximum deflection under a uniform distributed load $q = \rho g t_e$ is approximated as

$$\delta_{\max} \approx \frac{5qd^4}{384D}, \qquad D = \frac{E_{\text{eff}} t_e^3}{12(1-\nu^2)}, \tag{4.3}$$

where E_{eff} is the effective bending modulus of the electrode and ν is Poisson's ratio. The deflection is capped by the cavity height h. The corresponding "lost" cavity cross-sectional area per cavity is approximated by integrating the beam shape; for simply supported conditions,

$$A_{\text{sag}} \approx 0.64\, d\, \delta_{\max}. \tag{4.4}$$

For an array with N_{cav} cavities, the total sag area is $N_{\text{cav}} A_{\text{sag}}$. In the capacitance model, sag is incorporated by subtracting this baseline loss from the reference cavity air volume before computing C_0 and subsequent $C(\theta)$. This correction is particularly important when comparing cases with different pillar spacings d, since the sag deflection grows as $\delta_{\max} \propto d^4$, penalizing large cavities much more heavily than the ideal sensitivity gain would suggest. The sag-corrected optimum in the geometry studies therefore occurs at a moderate cavity width rather than monotonically at the largest span.

Figure 4.2 summarizes this comparison visually: relative to the ideal flat-electrode assumption, including sag lowers the effective initial air volume and suppresses the apparent advantage of the widest cavity spans, shifting the preferred design region toward moderate spacing.

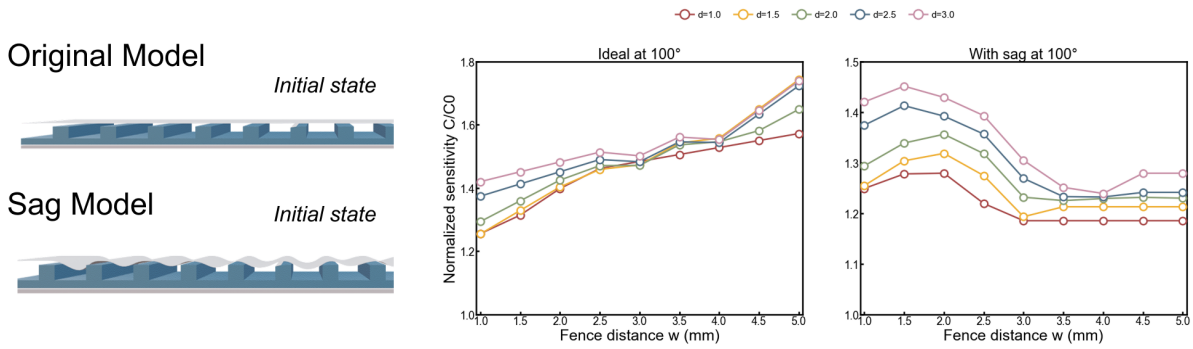


Figure 4.2: Comparison of ideal and sag-corrected bending models. Left: flat versus pre-deformed initial state. Center: predicted sensitivity at 100° without sag correction. Right: sensitivity with sag included. Sag correction reduces benefit of widest spans and shifts preferred design toward moderate spacing.

4.4 FEM-Guided Geometry Optimization

4.4.1 Geometry parameter space

To systematically explore how pillar spacing and dielectric core height affect bending transduction, we performed a parameter sweep over a simplified pillar unit-cell model. Table 4.2 summarizes the geometric and simulation parameters. Pillar width was held constant while cavity width (pillar spacing d) and core height h were varied over a non-factorial 31-point grid, concentrated toward the mechanically stable region of the design space; the structure was bent incrementally up to 100°.

4.4.2 DolfinX parameter sweep

The general DolfinX framework — parametric meshing in Gmsh, Yeoh hyperelastic constitutive law, and Newton-iteration nonlinear solves — is described in Section 2.4.2. Here we summarize the sensor-specific implementation and results for the bending branch.

A 2D plane-strain model of the pillar cross-section was used with spatially varying material coefficients to represent the structural silicone and a softer electrode layer. The rotating edge was driven using a rigid-connector kinematic relation

$$u(X) = c + \big(R(\theta) - I\big)(X - X_c), \tag{4.5}$$

Table 4.2: Geometry and simulation parameters used in the pillar-based bending sensor sweep. Units: mm unless otherwise stated.

Parameter	**Symbol**	**Values tested**
Fixed geometry		
Electrode thickness	t_e	0.05
Pillar width	p_w	1.0
Sweep variables		
Cavity width (pillar spacing)	d	1.0, 1.5, 2.0, 2.5, 3.0, 3.5, 4.0, 4.5, 5.0
Core height (electrode gap)	h	1.0, 1.5, 2.0, 2.5, 3.0
Number of cavities	N_{cav}	Set by design table; varies with d
Combinations evaluated	—	31 of 45 possible (d, h) pairs (non-factorial)
Simulation controls		
Maximum bending angle	$\theta_{\max}$	100°
Bending increments	N_{steps}	50

where X_c is the centroid of the driven edge, $R(\theta)$ is the prescribed rotation, and c is a set of global translation degrees of freedom introduced through a `Real` element. This construction reproduces a prescribed rotation while allowing the boundary to translate consistently under large deformation. A 31-case parametric grid over cavity width d (1.0–5.0 mm) and core height h (1.0–3.0 mm) was evaluated, of which 18 cases converged to the full 100° target and 13 stopped early (52°–90°) due to solver divergence at large rotation; each simulation produced a per-angle cavity area history, which was converted to an effective air-volume fraction and then to capacitance using the series-capacitor model of Section 4.3 with the sag correction applied at $\theta = 0°$.

Representative simulation trends from this sweep are shown in Fig. 4.3(c–f), where the predicted C/C_0–angle response is compared across selected geometric and material variations and then matched against experiment in Fig. 4.3(g–j). The cases that did not converge to the full 100° rotation were concentrated at large core height h (every $h = 3.0$ mm case stopped early, regardless of d), while the widest cavity widths tested largely converged; this is consistent with tall, slender pillars being the more buckling-prone geometry, rather than wide spacing itself being destabilizing.

4.4.3 Stability criteria and design window

FEM structural analysis was used to map stable and unstable pillar geometries across the design space. As shown in Fig. 4.3(a), the von Mises stress distribution on the pillar structure and the resulting stability map, plotted as pillar height versus inter-pillar distance, identify three regions: an unstable range where pillars buckle or produce non-repeatable contact, a desirable range where electrode deflection into the cavities is controlled and repeatable, and a stable but low-sensitivity range where pillars are too stiff to deflect meaningfully. The selected geometry targets the desirable region, consistent with the $d \approx 2$–$2.5\,\mathrm{mm}$ window identified by the sag-corrected DolfinX sweep.

4.5 Experimental Characterization

4.5.1 Angle–capacitance calibration

We built a dedicated rotation fixture to characterize sensor response under controlled bending. Starting from $\theta = 0°$, a motorized stepper-driven fixture incremented the joint angle in $10°$ steps up to $100°$. After each commanded displacement, the system held the target angle for approximately 3 s before data capture, then returned to $0°$ and waited an additional 2 s before the next step, consistent with the quasi-static evaluation conventions defined in Section 2.3. Capacitance was measured using a Keysight E4980AL LCR meter at 1 kHz with 1 V AC excitation in Cp/Rp mode. Three specimens were tested over approximately 500 sweep cycles each; the representative results are reported in Sections 4.5.2–4.6.2.

4.5.2 Geometric and material parameter validation

Figure 4.3 compares the model predictions against the corresponding experimental sweeps before the interpretation is separated into geometry, material, and angle-centricity effects in Sections 4.5.2–4.5.4.

Both simulation and experiment confirm a monotonic increase in normalized capacitance with bending angle, with sensitivity tunable via cavity width, pillar spacing, and dielectric constant. Higher graphene loading in the dielectric layer amplifies the capacitance response, consistent with the analytical model's prediction that increased dielectric contrast enhances sensitivity. Compared with the capacitive curvature sensor of Li *et al.* [95], which reports among the highest normalized sensitivity values in the flexible bending sensor

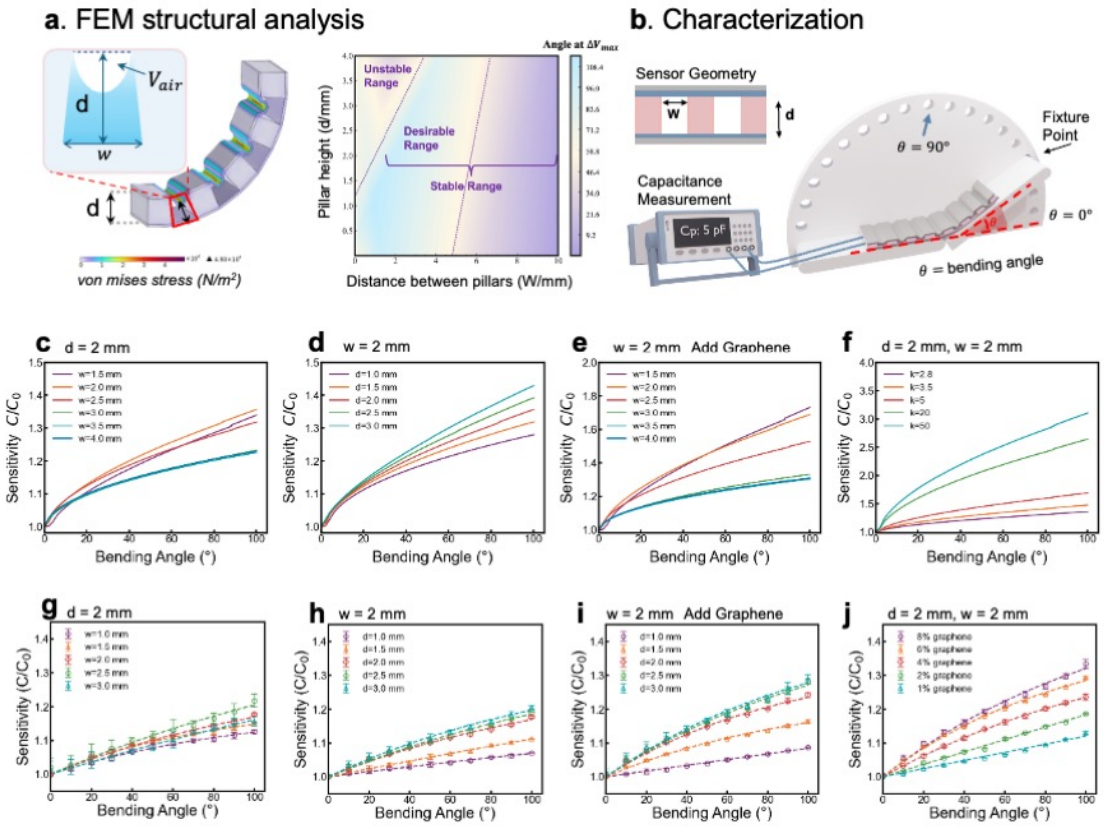


Figure 4.3: Model-experiment comparison across geometric and material variations. (a) Custom 3D-printed rotary characterization fixture. (b) Sensing mechanism: cavity collapse increases effective permittivity. (c–f) DolfinX predictions of C/C_0 versus bending angle. (g–j) Experimental measurements under matched conditions. (c,g) Pillar spacing fixed at 2 mm, cavity width varied. (d,h) Cavity width fixed at 2 mm, pillar spacing varied. (e,i) Cavity width varied with graphene-loaded dielectric. (f,j) Dielectric constant and graphene loading showing material-driven amplification.

literature, the present model-guided material and geometry tuning yields approximately a two-fold improvement in $\Delta C/C_0$ per unit angle, with simulations predicting up to an eight-fold further enhancement if substantially higher-permittivity dielectrics can be fabricated reliably.

4.5.3 High-permittivity dielectric strategy

Figures 4.3(e,i) and (f,j) directly demonstrate the effect of increasing dielectric permittivity. Increasing graphene loading from 0% to 8% in the PDMS matrix progressively amplifies the C/C_0 response at every tested bending angle, consistent with the analytical model's prediction that higher dielectric contrast increases sensitivity. The simulation counterpart sweeps k from 2.8 to 50 and shows the same monotonic trend, confirming that the graphene/PDMS experiments sample the lower portion of a broader material design space. The most aggressive simulated permittivities were not physically realized in fabrication, so the upper simulation bound represents a design target rather than a demonstrated result.

4.5.4 Angle-centricity of the pillar/air architecture

Taken together, the analytical model and the experimental parameter sweeps clarify why the pillar/air architecture outperforms conventional strain-dominant designs for joint-angle estimation. The dominant signal arises from macroscopic, geometry-driven redistribution of air volume as the upper electrode deflects into the cavities under bending. This mechanism is governed by the global curvature at the sensing site rather than by local surface strain at the electrode–substrate interface. As a consequence, moderate shifts in mounting position along the finger body — which alter the local strain state but leave the bending curvature largely intact — produce comparatively small changes in the sensor output. The experimental data in Sections 4.5.2 and 4.6 support this interpretation: across different pivot-point placements on the robotic finger and across the knee and finger anatomical sites, the $C(\theta)$ curves remain closely grouped. A six-participant gesture-recognition study using the same sensor on hands of different sizes (Chapter 5) provides further indirect evidence, though a controlled cross-user placement-variability study remains for future work.

4.6 Experimental Validation Across Anatomical Sites

4.6.1 Anatomical generalisability: large-joint validation at the knee

A key thesis claim is that the pillar/air transduction mechanism is governed by curvature at the sensing site rather than by geometry specific to the finger scale. To test this, the sensor was evaluated at the knee joint during repeated squat cycles — a site with a substantially larger anatomical radius, a wider range of motion, and different soft-tissue mechanics than the finger. As shown in Fig. 4.4(a), the device was placed over the anterior knee with

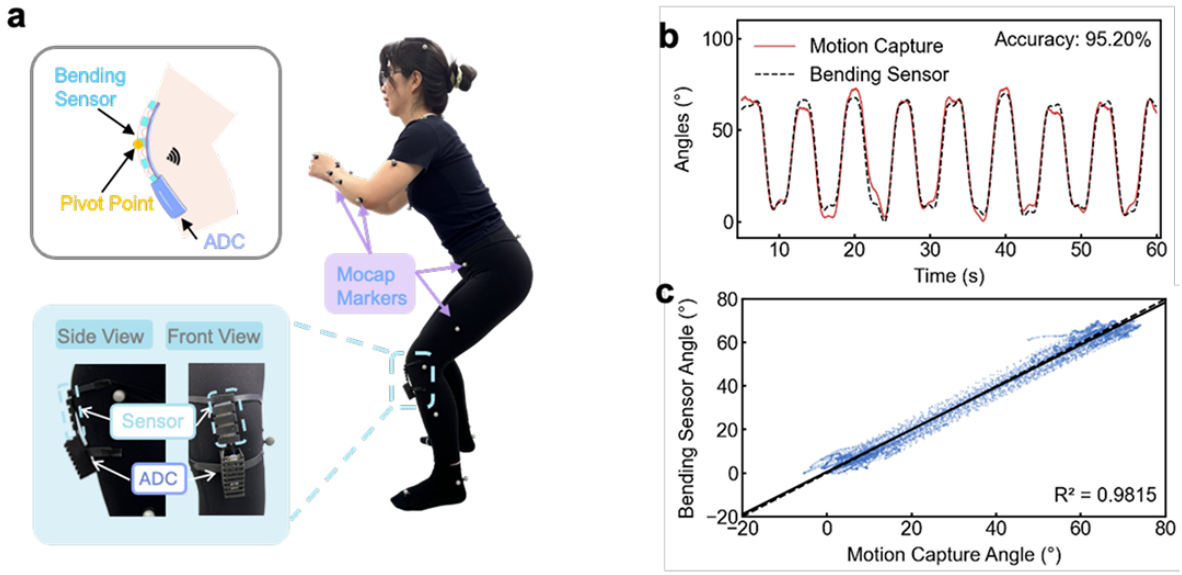


Figure 4.4: Knee joint angle tracking. (a) Mounting configuration with sensor spanning joint axis. (b) Time-series comparison of sensor output and motion-capture reference during squat cycles, showing 95.20% accuracy. (c) Scatter plot showing linear correlation of $R^2 = 0.9815$ over 0°–90° range.

the pillar region spanning the joint axis, using a low-profile attachment that conforms to the limb in both the front and side profiles. A co-located optical motion-capture system provided the reference angle throughout the trial.

Fig. 4.4(b) shows the time-series comparison over repeated squat cycles. The bending-sensor trace tracks the motion-capture waveform closely in both phase and amplitude, with a reported agreement accuracy of 95.20%. The scatter plot in Fig. 4.4(c) confirms a linear correlation of $R^2 = 0.9815$ across the full 0°–90° working range, with no systematic offset or saturation visible at the extremes.

This knee demonstration is important because the anatomical geometry, operating range, and curvature radius at the knee are all substantially different from those at the finger joints used in the calibration and robotic-finger experiments. The strong agreement across this different site indicates that the transduction remains governed primarily by geometry-driven cavity redistribution under bending curvature, rather than by conditions specific to finger-scale mounting.

4.6.2 Placement tolerance and cyclic stability under controlled actuation

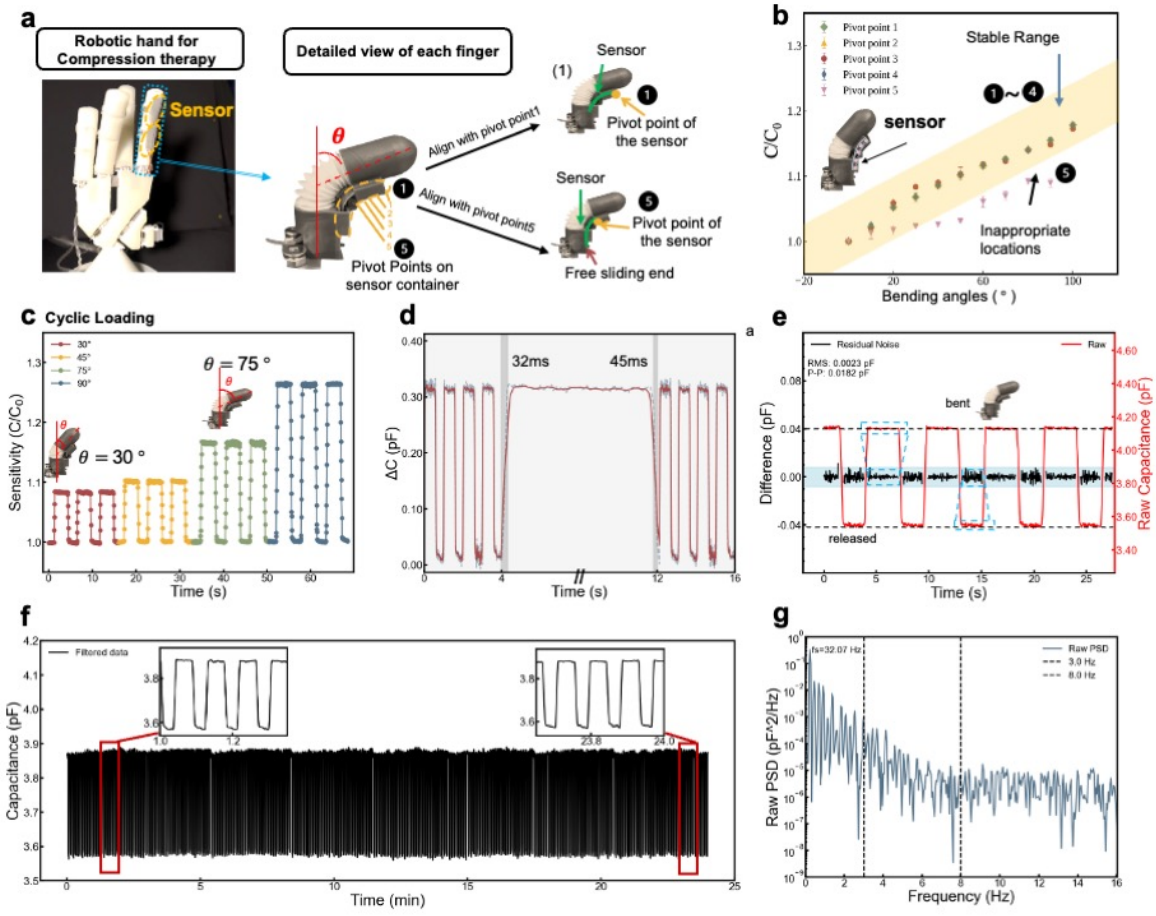


Figure 4.5: Validation of placement tolerance and cyclic stability under robotic-finger actuation. (a) Pneumatic soft–rigid hybrid finger with sliding sensor mount. (b) Normalized C/C_0–angle curves at five pivot locations showing closely grouped traces, confirming moderate shifts do not dominate output. (c) Cyclic loading at discrete angles, producing distinct plateaus. (d) Transient response (32 ms) and recovery (45 ms). (e) Power spectral density showing 99.0% below 3 Hz; RMS noise 0.0019 pF. (f–g) Twenty-five-minute continuous recording with no drift; frequency spectrum showing dominant content below 3 Hz.

The design requirement of placement tolerance, established in Section 4.1.2, predicts that moderate shifts in sensor mounting position should produce negligible changes in the $C(\theta)$ response because the transduction is governed by global curvature rather than local strain. A controlled robotic-finger platform was used to test this directly: a pneumatically actuated soft–rigid hybrid finger with a sliding sensor mount fixes the pivot point while leaving the distal end free, preventing tensile strain build-up and allowing the pivot position to be varied systematically between trials.

As shown in Fig. 4.5(b), the normalized capacitance–angle curves remain closely grouped across the tested pivot-point locations: the maximum inter-position spread in $\Delta C/C_0$ at any given angle is less than 20 % of the full-scale response, confirming that the output is governed primarily by bending geometry rather than exact mounting position. Repeated actuation at 30°, 45°, 75°, and 90° produces distinct and reproducible signal plateaus, demonstrating multi-state angle resolution under cyclic loading. Noise analysis gives an RMS noise of 0.0019 pF and peak-to-peak variation of 0.0198 pF, with 99.0% of signal power concentrated below 3 Hz. The 25-minute recording window shows stable output throughout the test.

The sensor is integrated into the personalized glove platform and applied to gesture recognition in Chapter 5.

4.7 Summary

This chapter presented a pillar-structured capacitive bending sensor with an air-cavity dielectric architecture for wide-range, angle-centric bending detection. The analytical model and FEM studies show why dielectric contrast, cavity span, and pillar height jointly determine sensitivity and stability, while the sag correction identifies a practical design window at moderate cavity widths. Experimental validation confirms that the transduction remains governed primarily by geometry-driven cavity redistribution, making the sensor comparatively tolerant to the tested mounting-position shifts and transferable across the finger- and knee-scale demonstrations reported here. The best-supported results from the current chapter are: 95.20% knee-tracking accuracy with $R^2 = 0.9815$, 32 ms response and 45 ms recovery times, and low-noise robotic operation with 99.0% of signal power below 3 Hz. Controlled cross-user placement validation remains future work, while glove integration and gesture-recognition performance are reported in Chapter 5.

Future work includes validating higher-permittivity composites to approach the eight-fold sensitivity gain predicted by the analytical model, refining the constitutive model for

the bonding and electrode layers, and integrating the bending sensor into the personalized glove design pipeline developed in Chapter 5.

Chapter 5

Personalized Data Glove Design

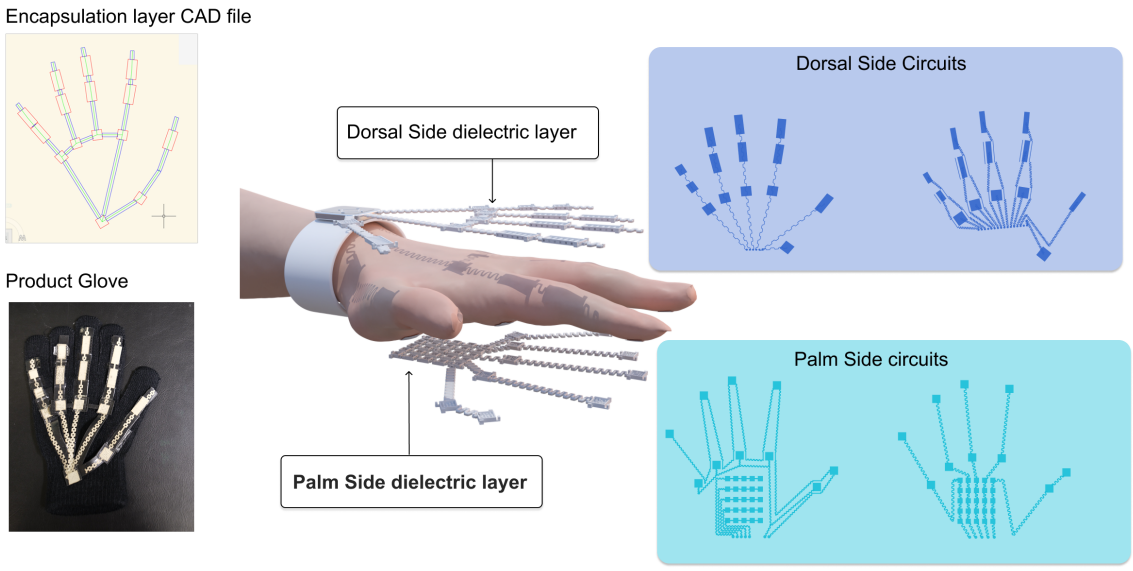


Figure 5.1: System-level architecture of the personalized data glove. *Centre:* 3D render with dorsal bending modules and palmar pressure modules, plus wrist electronics. *Left:* CAD output and fabric prototype. *Right:* dorsal and palmar circuit layers with routing.

5.1 Existing gloves: focused landscape

Chapters 3 and 4 develop the pressure and bending sensor elements that the glove must host; the present chapter addresses the remaining integration problem: *how to embed, route, and personalize these sensors* so that they align with each user's anatomy and remain reliable under OTG constraints. As the mechanical platform and primary OTG form factor, the glove must simultaneously survive repeated bending, shear, and daily wear while enabling continuous, anatomy-aligned capture of contact pressure and joint kinematics.

This section surveys existing glove systems only to the extent needed to derive glove-level design constraints. Across the assistive, sensing, and clinical glove categories reviewed in Sections 5.1.1–5.1.3, the recurring failure mode is *misalignment due to generalized sizing*: a glove sized for the average hand places sensors at locations that are systematically offset from the anatomy of most individuals who wear it.

5.1.1 Assistive soft robotic gloves for grasp support

One family of glove systems targets *assistance* via soft actuation (pneumatic networks, tendon/cable systems, or textile actuators). These devices emphasize functional grasp support, usability, and clinical feasibility, often validated through user studies and task-based metrics [125, 126]. Representative systems include fully wearable soft exoskeleton gloves for daily grasp assistance [127] and textile-based assistive gloves that quantify assistance via grasp-force and EMG analyses [128]. Across this family, sensing is often limited to low-channel-count measurements (e.g., on/off states, a few flex sensors, or global force proxies), reflecting the difficulty of integrating dense, comfortable, and robust sensor arrays without compromising wearability.

The dominant trade-off is comfort against sensing density. Actuation hardware—air bladders, tendon sheaths, fabric actuators—already occupies most of the dorsal and lateral finger real estate. Dense sensor arrays exacerbate material stacking, stiffen joints, and create pressure points that shorten tolerable wear time. Most assistive designs therefore settle for sparse sensing or confine sensors to regions free of actuators, leaving gaps in contact-pressure and joint-angle coverage that are acceptable for grasp augmentation but problematic for continuous biomechanical monitoring.

This trade-off scales with hand size. On a small hand, the dorsal area per phalanx may be only marginally wider than a single actuation channel, leaving no room for an adjacent bending sensor without encroaching on inter-phalangeal creases. Even on larger hands,

stacking a sensor layer over an actuator raises the profile beyond the point where the glove flexes naturally; users report stiffness and fatigue limiting wear to tens of minutes [127, 126]. Thinner substrates and lower-modulus elastomers help at the margins but do not eliminate the geometric conflict, and the layout problem grows combinatorially with the number of instrumented joints.

Placement variability compounds the stacking problem. Adjustable straps and elastic panels let a single glove accommodate a range of hand sizes, but the same adjustability allows the glove to sit differently each time it is worn, shifting sensor alignment relative to joints and contact pads [129, 130]. The clinical consequences are developed in Section 5.1.3.

Alignment sensitivity is compounded by *actuation–sensor coupling*. In a glove that both assists and measures motion, actuators introduce parasitic loads—normal pressure from inflated bladders, shear from sliding tendons—that the sensor cannot distinguish from the physiological signal. Residual coupling after mechanical isolation makes the effective noise floor actuation-state-dependent, creating a context-dependent calibration problem. These effects reinforce the case for separating sensing from actuation and, within the sensing domain, for anchoring sensor locations to anatomy rather than to garment coordinates.

These constraints—low-profile integration, fast donning, long-wear comfort, and bending durability—directly motivate anatomy-tailored sensor placement to reduce fit-driven alignment error.

5.1.2 Smart data gloves for sensing and gesture recognition

A second family focuses on *sensing* for gesture recognition and hand posture tracking using flex/bend sensors, strain sensors, IMUs, or capacitive sensor arrays [131, 132, 133]. Recent work shows that textile-integrated sensors and near-sensor processing can enable high-accuracy gesture classification with modest channel counts, but these systems are often optimized for discrete gesture sets rather than continuous biomechanical monitoring. Further, many reported gloves assume a one-size or limited-size fit and rely on calibration procedures that are sensitive to sensor placement, which becomes problematic when seeking anatomy-aligned pressure and joint-angle measurements in assistive/rehabilitation contexts.

Routing and connectorization present a persistent integration challenge. Gesture-recognition gloves often treat wiring as an implementation detail because a small number of flex sensors or IMUs can be bundled into a single dorsal harness. Multi-modal sensing multiplies channel count and requires longer traces along highly mobile surfaces, introducing failure points—trace fatigue at knuckles, delamination under shear, snagging during donning—and

forcing uncomfortable strap placement to keep cables from shifting [134]. These practical constraints shape how many sensing sites can be deployed and where they can be placed.

Placement sensitivity also creates an *implicit calibration burden*. High classification accuracy achieved after per-user fitting may not transfer when the glove is re-donned with small offsets or when the fabric relaxes over time [6, 27]. For biomechanics-oriented monitoring, such drift changes the physical meaning of the measurements rather than merely adding noise. An anatomy-parameterized layout anchored to landmarks is intended to reduce calibration to a light-touch check rather than a full re-derivation; the geometric component of that claim is quantified in Section 5.4.4, while its effect on sensing performance remains to be established.

Together, these issues motivate clear routing strategies, detachable electronics for washability, and explicit handling of fit-driven alignment error through anatomy-parameterized placement.

5.1.3 Clinical assessment and rehabilitation monitoring gloves

Clinical-oriented gloves target quantitative assessment (e.g., post-stroke hand function, arthritis monitoring) and therefore value repeatability, interpretability, and robustness across users [135, 4, 120]. However, practical barriers persist: rigid components reduce comfort, sensor placement varies across sessions, and many designs depend on older sensing technologies or calibration-heavy pipelines. Two failure modes are particularly consequential for clinical deployment.

Placement variability and calibration stability. Longitudinal hand-function monitoring requires measurements to remain comparable across sessions, which places demands on the glove's ability to maintain consistent sensor-to-anatomy alignment. For rehabilitation applications, clinicians track recovery through metrics such as active range of motion (ROM), movement speed, and grasp force [4]; if sensor placement shifts between sessions by amounts comparable to the physiological change of interest, genuine improvement becomes indistinguishable from measurement artefact. Placement-dependent variability is therefore a clinical validity concern, not merely a convenience issue.

Prior work identifies fit variability as the primary driver of this problem: small differences in how a glove is donned—finger insertion depth, strap tension, wrist cuff position—translate directly into shifts in sensor location relative to underlying anatomy [129, 130]. For strain-based bending sensors, even millimetre-scale offsets from the intended joint axis

alter the effective lever arm and shift the calibration curve, and placement-induced signal variability of 15–30% has been quantified in glove evaluations even when subjects are retrained on the same sensor [6, 27]. Physiological changes (post-stroke oedema, soft-tissue volume fluctuation) and material relaxation over repeated use further contribute to between-session drift [135]. These effects motivate an architecture that anchors sensor placement to anatomical landmarks rather than to a generic garment coordinate system, with the intent of reducing placement-dependent calibration error; whether this is sufficient to support longitudinal clinical monitoring without per-session recalibration is identified as future work.

Interpretability and standardization. Clinical workflows demand measurements that map onto recognizable, standardized constructs [5]. Therapists and physicians reason in terms of joint ROM (measured in degrees), grasp strength (measured in Newtons or kilograms-force), movement timing (onset, duration, inter-event intervals), and contact distribution (which regions of the hand engage an object and with what relative pressure). These constructs are embedded in assessment protocols, reimbursement codes, and inter-disciplinary communication; a measurement system that cannot express its outputs in these terms is difficult to integrate into routine care, regardless of its technical sophistication.

Many data-glove systems optimize for classification accuracy rather than interpretable biomechanical outputs. A classifier that distinguishes grasp types by exploiting distributed array features may not expose which anatomical variable changed. Such systems can detect *whether* a patient performed a prescribed exercise, but longitudinal monitoring requires tracking *how* the movement is performed: a clinician needs to know that PIP flexion ROM increased from 60° to 75° over four weeks, not simply that a classifier's confidence score shifted.

Standardization also facilitates comparison across patients, sites, and studies [7]. Incompatible output representations between glove systems make data pooling difficult, and even replacing a worn-out glove within a single center should not require re-establishing patient-specific calibration from scratch. These considerations favor outputs grounded in physical units (degrees, Newtons) with lightweight, reproducible calibration.

The *calibration burden* compounds the problem. Complex user-specific models may achieve excellent accuracy after an initial training phase, but that phase can require 75–90 minutes per user [32], specialized reference equipment, and expert supervision. If retraining is needed after every donning event, the system becomes impractical for routine clinical use. Calibration protocols demanding lengthy reference-posture sequences or maximal-force exertions may also be infeasible for populations with limited motor control or fatigue

tolerance [136, 120]. A clinically deployable glove should reduce calibration to a brief, self-administered check at the start of each session.

Architectural implications. Taken together, the clinical requirements impose four architectural constraints on the present design: anatomy-referenced sensor alignment resilient to small fit changes; electronics isolated from the textile for cleaning and re-use; protocol-compatible outputs in physical units (degrees, kPa) consistent with the evaluation conventions of Chapter 2; and lightweight calibration that does not require per-session model retraining or specialized reference equipment [120]. These constraints drive the personalization pipeline and prototype architecture developed in the remainder of this chapter.

5.2 Glove design goals and constraints for this thesis

The failure modes surveyed above constrain the design space for the personalized data glove along three axes: functional sensing, OTG wearability, and personalization/alignment.

Table 5.1 aggregates these requirements into literature-informed design targets that bypass the generalized-sizing limitations of prior work. These targets are not direct measurements from the present prototype; rather, they are practical bounds adopted from prior glove, ergonomics, and wearable-device literature to guide the automated layout and integration pipeline described in the remainder of this chapter.

Table 5.1: Literature-informed design targets and constraints for the personalized OTG data glove.

Design target	**Rationale**
Functional sensing	
Pressure range: 0–50 kPa	Covers gentle contact through firm grasp [137, 138].
Angle-centric bend response	Insensitive to parasitic skin strain (§5.1.2).
Dual palmar/dorsal paths	Avoids mechanical interference between sensor families.
OTG wearability	
Stack thickness $\lesssim 0.8$ mm	Sub-mm regime preserves dexterity and tactility [139, 140].
Session wear ≥ 0.5 h	Matches clinically relevant session lengths [141, 127].
Flexion life $\geq 10^4$ cycles	Minimum durability for repeated joint motion [134, 142].
Detachable electronics	Allows textile cleaning independent of PCB (§5.1.3).
Alignment and fit	
Anatomy-referenced layout	Anchors sensors to joint centres; intended to reduce placement-dependent error (geometric validation in Section 5.4.4).
Parametric scaling	Standard modules fit all hand sizes via routing adjustment.

5.3 Anatomy-to-layout mapping pipeline

Limitations in comfort, routing, and clinical repeatability are frequently downstream of a single root cause: *misalignment*. The same sensor module behaves differently when its location shifts relative to an underlying joint or contact pad, whether due to generic sizing, donning variation, or material relaxation. The workflow introduced here abandons the one-size-fits-all starting point: anatomy measurements define a parametric pattern, sensor modules are placed at landmark-referenced coordinates, and manufacturable layouts are generated with routing choices that scale consistently across users. The following subsections develop each stage in turn.

5.3.1 Hand landmark capture

The first stage of the pipeline extracts anatomical landmarks and dimensional measurements from the user's hand. Glove ergonomics research demonstrates that a limited subset of hand dimensions—principally hand length and circumference—can serve as key drivers for practical sizing systems [13], but per-digit lengths are additionally necessary here because finger and palm morphologies vary independently of overall hand size: peripheral digit lengths differ by more than 1 cm across individuals within the same global hand-size bracket [33]. The landmark set must therefore resolve individual phalanx segments, joint-crease axes, and palmar contact zones independently for each finger.

Photo-based landmark extraction. In the implemented workflow, calibrated photographs of the hand in a standardized flat dorsal pose serve as the primary input. MediaPipe [143] hand-keypoint detection automatically localizes 21 landmarks on the hand surface (Fig. 5.2); the operator can override individual points via the annotation interface if the detector fails on a specific finger or the hand boundary is partially occluded.

Scale is established before detection through a manual two-point calibration: the operator clicks two points of known physical separation on the photograph and enters the corresponding distance, yielding a pixel-per-millimetre conversion factor applied to all subsequent geometry. An L-shaped reference ruler placed in the scene provides an alternative calibration path when a rigid reference object is available in the frame. The feasibility of this photo-based approach is supported by studies showing that 2D/3D image analysis produces hand dimensions highly correlated with direct tape and calliper measures [144]. From the confirmed landmarks and the pixel scale, the pipeline computes phalanx segment

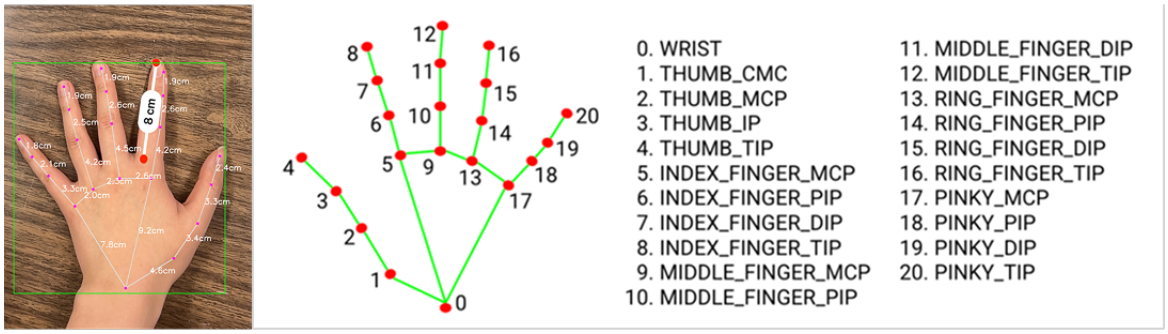


Figure 5.2: MediaPipe hand-keypoint detection applied to a dorsal hand photograph. *Left:* 21-landmark skeleton overlaid on the source image. *Right:* landmark index reference with anatomical labels and derived inter-landmark bone lengths.

lengths (proximal, middle, and distal for each finger), inter-joint spans, and palm width, which together constitute the input to the subsequent pattern-generation stage.

Where photographic capture is impractical—for example, in a clinical setting with limited equipment or restricted patient mobility—a manual protocol using digital callipers and standardized landmark definitions can substitute. The operator records segment lengths between palpated joint centres, palm breadth at the metacarpal heads, and hand length from wrist crease to middle-finger tip following established anthropometric conventions [145]. This fallback is more operator-dependent and time-consuming, but yields the same landmark data structure and can be cross-checked against normative proportions.

Landmark data structure and validation. Both capture paths produce a common landmark data structure containing: (i) 2D coordinates of each landmark in a hand-centred reference frame, (ii) derived segment lengths and widths, and (iii) capture metadata (date, dominant hand, capture method). Before the structure is passed to the layout engine, the pipeline applies ratio-based sanity checks: phalanx length ratios are compared against population norms [146, 147], and any landmark with high detection uncertainty is flagged for re-capture. These checks guard against downstream pattern errors arising from measurement artefacts or atypical postures, since digit lengths can vary by 7–12% between splayed and gripping poses [148], and disproportionate segment layouts can cause glove shifting and sensor misalignment during use.

5.3.2 Parametric pattern and sensor layout

Given a validated landmark set, the second stage generates a 2D glove pattern whose geometry is parameterized by the user's anatomy and whose sensor positions and trace routing are derived automatically from the same landmark coordinates. Prior work establishes that anatomical measurements can be converted into parametric 2D glove patterns suitable for smart wearables [14]. The present implementation extends that idea by coupling the pattern geometry to a constraint-checked routing engine that produces manufacturable trace layouts directly, without manual CAD intervention.

From landmarks to pattern geometry. The pattern is constructed by projecting dorsal and palmar surfaces of the hand onto a flattened 2D template. Finger sleeves are sized according to measured segment lengths and circumferences (the latter inferred from width measurements and an assumed elliptical cross-section). Key reference lines—joint-crease axes, fingertip centroids, and thenar/hypothenar contact zones—are transferred onto the pattern as alignment guides. Seam allowances and ease factors are added parametrically, but in the finger regions these are kept deliberately small and material-dependent so that the finished glove neither restricts motion nor introduces excessive slack that would allow sensor migration [14, 149]. Sensor module coordinates and orientations are encoded on the pattern as landmark-referenced placements, but deciding *which* anatomical zones to target requires first understanding how the hand surface deforms during functional motion. That analysis is developed in Section 5.3.3 before sensor assignments are finalized in Section 5.3.4.

5.3.3 Gesture-aware skin-strain analysis

Before assigning sensor modules to specific pattern locations, we quantified the local surface area change that the hand skin undergoes during representative functional poses. Using the MANO parametric hand model [150], we computed the per-patch area ratio $A_{\text{posed}}/A_{\text{flat}}$ across the hand surface under three poses representative of OTG use: flat (neutral reference), cylindrical grasp, and pinch. Figure 5.3 shows the result as a colour-mapped overlay on the 3D hand mesh.

The analysis informs sensor placement on two counts. It identifies zones where skin surface area changes substantially during functional motion — sites where a strain-based sensor would generate a large but pose-dependent, placement-sensitive signal — and confirms that the proposed sensor locations sit in mechanically appropriate zones for their

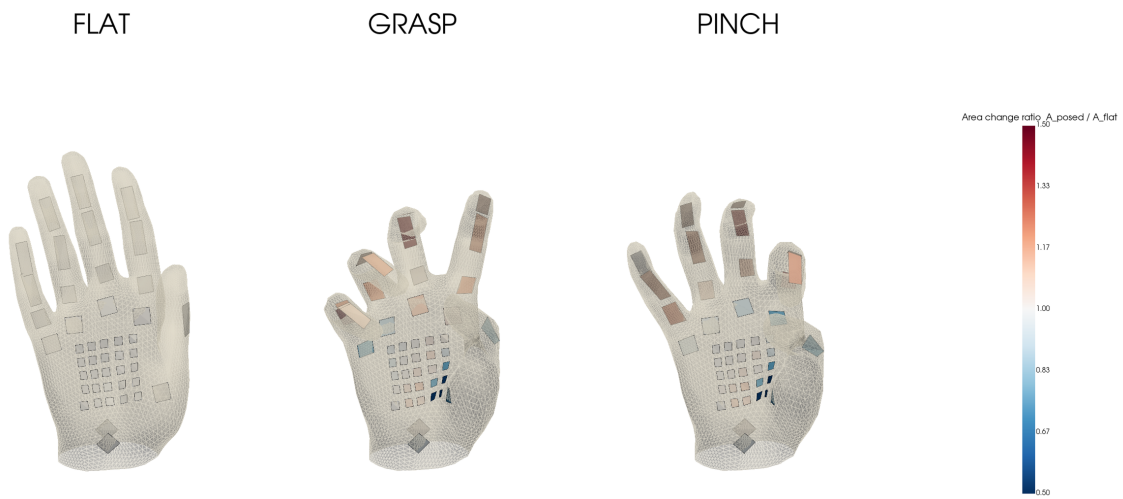


Figure 5.3: Gesture-aware skin-strain analysis using the MANO parametric hand model. Area-change ratios $A_{\text{posed}}/A_{\text{flat}}$ are shown for flat, cylindrical grasp, and pinch poses. Largest changes concentrate in fingertips and palmar regions during grasp, while dorsal regions remain closer to neutral, supporting pressure placement palmarly and bending modules dorsally.

respective transduction mechanisms. As seen in Fig. 5.3, the grasp and pinch poses produce the strongest local area changes in selected fingertip regions, lateral palmar regions, and parts of the web-space boundary, whereas much of the dorsal finger surface remains closer to neutral. This is consistent with placing pressure modules on contact-dominant palmar zones while reserving dorsal proximal and middle phalanges for bending sensors. Because the bending output is intended to depend on global curvature rather than local skin stretch, positioning the dorsal modules in lower-surface-strain regions helps reduce contamination from fit-dependent pretension and placement variability. The relatively mild area change along dorsal-hand routing corridors likewise supports their use for interconnect paths. These observations are used directly in the sensor module mapping of Section 5.3.4.

5.3.4 Sensor placement and trace routing

The parametric pattern geometry (Section 5.3.2) and strain-zone assignments (Section 5.3.3) together determine where sensor modules from Chapters 3 and 4 are placed and how conductive traces are routed between them. The two sensor families occupy complementary surfaces of the glove: pressure modules on the palmar side, bending modules on the dorsal side. This separation simplifies the mechanical design—palmar layers prioritise contact compliance and abrasion resistance, while dorsal layers prioritise low bending stiffness and strain transparency—and means that placement tolerances, alignment references, and failure modes under misalignment differ between the two families.

Pressure module placement (palmar side). Pressure-sensing elements target regions where the hand makes contact with objects during functional grasp and manipulation. Three anatomical zones are prioritised: (i) fingertip pads, centred on the contact centroid identified during landmark capture; (ii) proximal-phalanx palmar surfaces, positioned midway along the segment and offset palmarly to avoid interference during finger adduction; and (iii) thenar and hypothenar eminences, referenced to the palmar crease and hypothenar border. The parametric pattern anchors each module's centroid to the nearest joint-crease reference line, so modules scale and translate with hand size while preserving their relationship to the underlying anatomy.

Bending module placement (dorsal side). Bending sensors target the dorsal surface of each finger, where the sensor's angle-centric response (Chapter 4) can be exploited most directly. Each module is centred on a joint axis—typically MCP and PIP for each finger, with optional DIP coverage where clinical relevance justifies the added channel count. The longitudinal extent spans the expected flexion arc while maintaining a clearance of roughly 2–5 mm from the crease apex on each side to prevent buckling and reduce fatigue loading [130, 27]. Alignment is more sensitive than for pressure modules because the measured signal depends on the sensor's position relative to the joint's instantaneous axis of rotation; the parametric pattern constrains the sensor centroid to a dorsal midline computed from lateral edge landmarks [151].

Palmar layout engine. The palmar routing problem is more constrained than the dorsal case because traces must navigate between densely packed sensor pads on a surface that also bears contact loads. To handle this automatically, the layout engine adopts a dual-layer row–column architecture implemented in Python with Shapely as the computational

geometry backend. Each pressure sensor pad sits at the intersection of two orthogonal trace nets: a *column* bus that runs longitudinally along each finger and across the palm, and a set of *row* nets that connect sensor pads laterally. Separating the two trace directions onto distinct conductive-fabric layers avoids electrical shorts at crossings and allows each layer to be fabricated as a single subtractive cut from a conductive textile sheet.

Within each layer, the routing engine follows a three-stage workflow. First, the sensor layout is defined from the prescribed pad geometries, electrical net assignments, clearance requirements, and geometric constraints of the hand. Second, sensor pads are positioned according to the extracted anatomical landmarks, after which conductive traces are automatically routed between pads belonging to the same net while satisfying spacing and non-intersection constraints. Local detours are introduced where necessary to route traces around sensor regions and other restricted areas. Finally, the glove boundary is constructed from the completed sensor and routing geometry by combining the finger and palm regions with an appropriate design margin. The resulting outline is shared between the two conductive layers to ensure consistent alignment and fabrication geometry.

The engine outputs DXF trace files and Gerber files suitable for laser cutting or PCB fabrication, together with a cutout layer for subtractive manufacturing: each trace is buffered into a corridor polygon, overlapping corridors are merged via `unary_union`, and sensor footprints on the same electrical net are excluded from subtraction so that traces can pass through their own pads. The same pipeline generates mirrored outputs for the opposite hand by reflecting the geometry about the substrate centreline. All coordinates scale with the landmark data, so the same scripts produce anatomy-matched layouts for different hand sizes without per-user scripting changes.

Both palmar and dorsal fabrication outputs are generated by the pipeline and are architecturally complete. A standalone 8×8 pressure sensor array was fabricated and tested to verify single-pixel addressability (Section 5.4.1); full glove-level integration combining both sensor families is reserved for future work.

Dorsal routing. Dorsal traces from bending modules run proximally along the dorsal midline of each finger, converging at the MCP knuckle region before crossing onto the hand dorsum. Where multiple fingers' traces converge, the pattern defines a bundling zone that collects them into a multi-conductor ribbon directed toward the wrist. Transition points where traces cross a joint axis are constrained to maintain a bend radius on the order of a few millimetres, following flexible-interconnect design guidance [134, 152].

Output artefacts. The combined pattern and routing stage aggregates its derived geometry into a common JSON manifest and a set of shared boundaries: the glove outline, per-layer trace corridors, cutout polygons, and sensor-placement metadata. This shared representation links the computational layout engine to the 3D glove model and 2D fabrication outputs, ensuring that every fabrication artefact remains geometrically consistent with the same anatomical input. The manufacturing artefacts themselves are described in Section 5.3.6.

5.3.5 Interactive review of generated glove layouts

The core pipeline operates automatically: a hand photograph is used for landmark extraction, sensor-position and routing generation, and fabrication-output generation. An interactive interface supports review of the generated layout, correction of uncertain landmarks, and inspection of routing alternatives when manual assessment is needed. For straightforward hand geometries, the automated output requires no adjustment.

The interface uses the scale calibration and landmark extraction described in Section 5.3.1. After landmark positions are confirmed or corrected, the pipeline derives sensor positions and rotations using the parametric rules of Sections 5.3.2–5.3.4 and overlays the resulting layout on the source photograph for review.

Endpoint-fit and segment-count measures provide quantitative checks of routing convergence. Following any landmark correction, routing validity is evaluated against geometric boundary and clearance constraints before fabrication outputs are generated.

The reviewed layout is stored in the common manifest described above, which supplies the same routing logic, clearance rules, and geometry to the downstream fabrication procedures (Fig. 5.6). The manifest supports generation of a parametric 3D glove model for visualisation and fabrication-jig preparation, as well as 2D textile-cutting and trace-routing files. Using a shared representation preserves correspondence between the reviewed layout and both fabrication outputs.

5.3.6 Manufacturing outputs and assembly notes

The final pipeline stage translates the parameterized pattern, sensor placement map, and routing corridors into a set of manufacturable artefacts and provides high-level guidance for glove assembly. The goal is to produce outputs that a technician or automated cutting system can use directly, while keeping the assembly process modular enough to support iterative design changes and component-level serviceability.

Output artefacts. The pipeline generates four primary deliverables:

1. **Pattern outlines**—vector-format cut files (DXF or SVG) for each textile layer (dorsal shell, palmar shell, finger sleeves, wrist cuff). These include seam allowances, notch marks for alignment, and annotations indicating material grain direction where relevant.

2. **Sensor placement map**—an overlay that marks the centroid, orientation, and footprint of every pressure and bending module on the flat pattern. Each module is labelled with its channel identifier and keyed to the bill of materials. Alignment features (registration marks, tab outlines) are included where the assembly procedure relies on mechanical indexing.

3. **Routing map**—a separate overlay showing the conductive-trace corridors, including trace widths, transition-point strain-relief features, and clearance envelopes. Where traces must cross (e.g., at the dorsal bundling zone), the map indicates layer assignments or insulation-bridge locations.

4. **Connector placement**—the location and orientation of the wrist-mounted connector interface that mates the glove's flexible traces with the rigid electronics hub printed circuit board (PCB). The connector region is designed to sit on the dorsal wrist, clear of the wrist crease, and is oriented so that the mating action does not stress nearby traces.

Assembly workflow. In the current prototype workflow, glove assembly proceeds in broad stages: (i) cut textile layers from the pattern files, (ii) apply or bond sensor modules at the marked placements, (iii) route and attach conductive traces along the designated corridors, (iv) join textile layers (sewing or bonding), and (v) attach the wrist connector interface. The exact bonding and joining parameters depend on the textile and sensor substrate materials; accordingly, the pipeline fixes *where* each component is placed and how the layers relate geometrically, while allowing the detailed fabrication process to be tuned during prototype builds.

Encapsulation. Sensor modules and traces require encapsulation to protect against moisture, abrasion, and mechanical damage during wear and cleaning. The encapsulation strategy balances protection with flexibility: a thin thermoplastic polyurethane (TPU) film (Bemis), typically in the tens-to-hundreds of micrometres range rather than millimetres, covers traces and module edges, while the active sensing areas of pressure modules are

left exposed or covered with a compliant membrane that does not attenuate the target pressure range [153, 154]. Bending modules, which operate on the dorsal surface and are less exposed to direct contact, receive a continuous TPU encapsulant layer that also serves as a strain-distribution medium.

Detachable electronics and serviceability. A key design decision is the separation of the *sensing textile* (glove body, embedded sensors, and traces) from the *electronics module* (signal conditioning, digitization, wireless communication, and battery). The electronics module attaches to the wrist connector and can be removed for charging, firmware updates, or replacement without disturbing the sensing textile. This separation provides two practical benefits:

- **Component-level replacement:** if a sensor module fails or a trace breaks, the affected textile section can be repaired or replaced independently of the electronics. Conversely, electronics can be upgraded without re-fabricating the glove.
- **Multi-glove sharing:** a single electronics module can serve multiple glove sizes or configurations (e.g., left and right hand), provided the connector pinout is standardized, reducing per-user hardware cost.

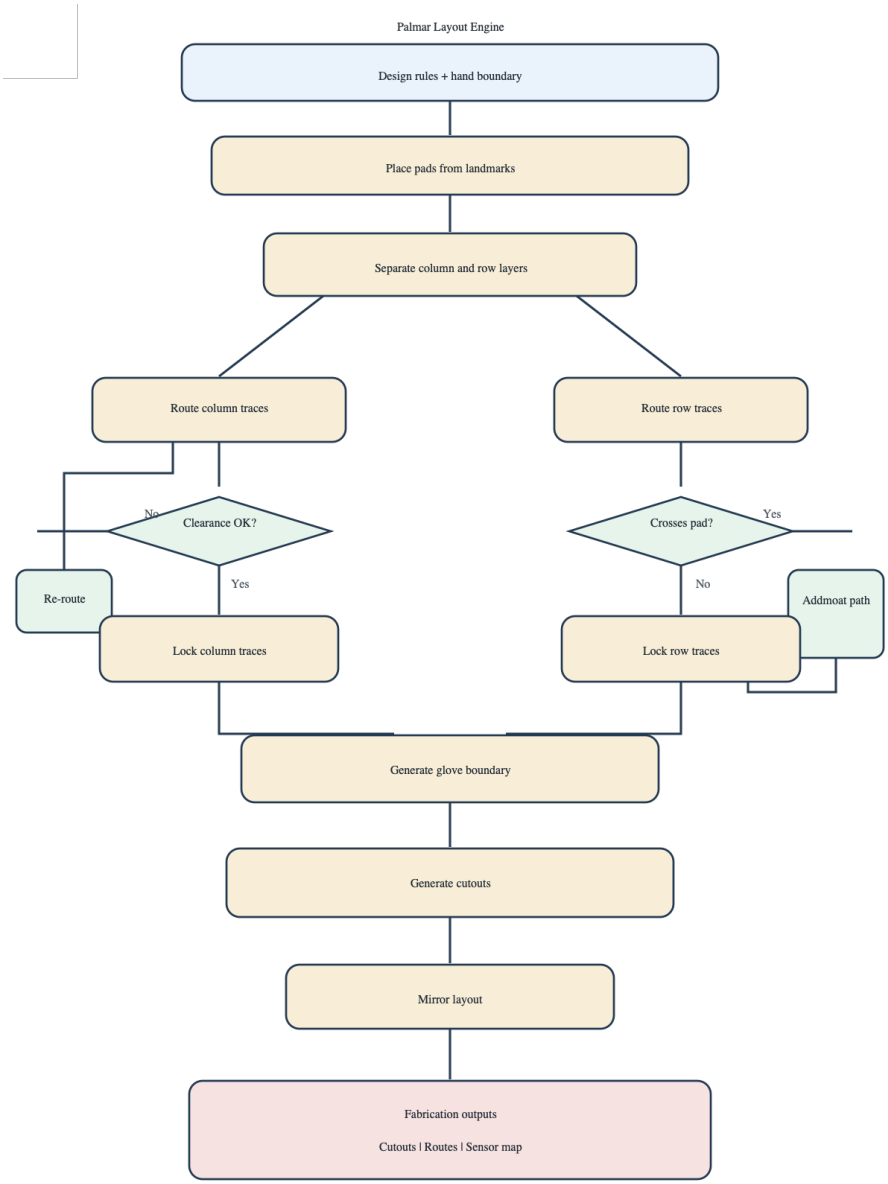


Figure 5.4: Palmar layout engine algorithm. Design-language specification and landmark-derived coordinates enter a dual-layer routing pipeline. Column and row traces are generated with clearance checking and moat routing, producing glove boundary and fabrication outputs.

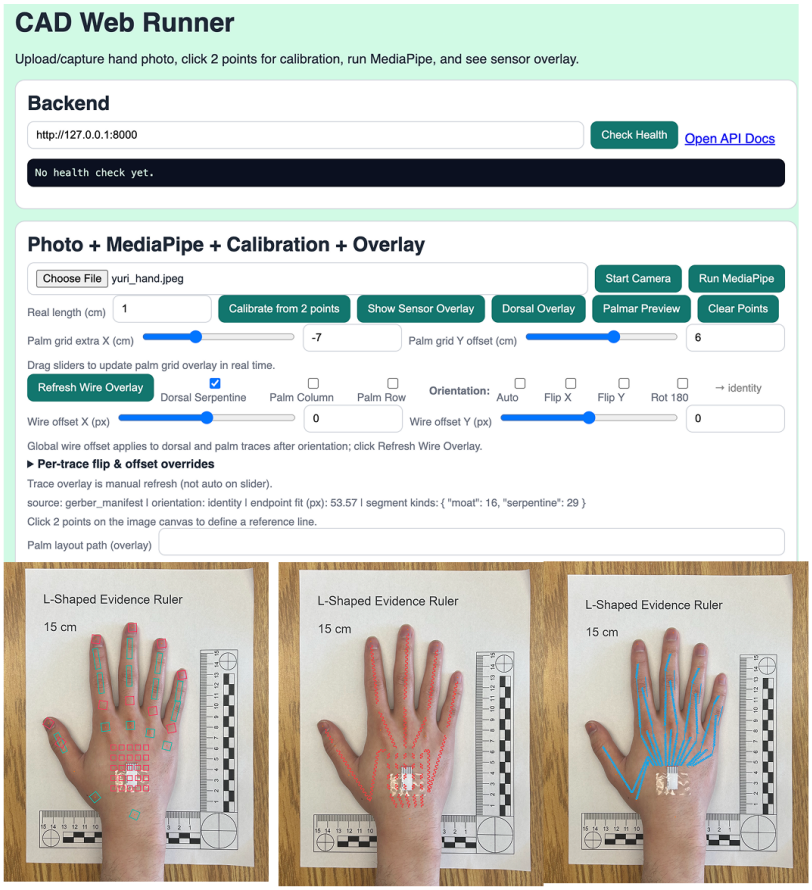


Figure 5.5: Interactive interface for reviewing and adjusting the anatomy-to-layout pipeline. The example shows calibrated landmark extraction together with the generated sensor-placement and routing overlays.

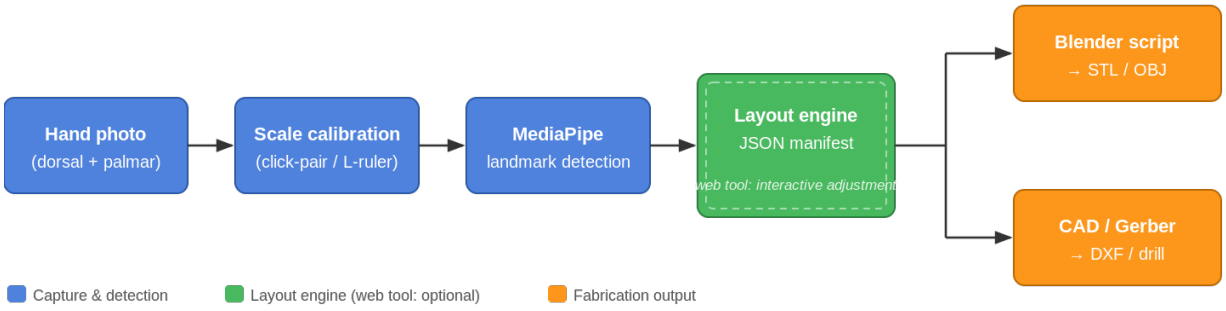


Figure 5.6: End-to-end fabrication pipeline from photograph to manufacturable artefacts. Image capture and landmark extraction feed the layout engine, which produces a JSON manifest. Downstream scripts generate 3D geometry (STL/OBJ) and 2D fabrication files (DXF, Gerber).

5.4 Prototype realization and system integration

The garment-level layout and fabrication workflow of Section 5.3 was realized by embedding the pressure and bending modules into a textile stack, interfacing the sensor network with a detachable wrist electronics module, and defining a lightweight calibration and readout procedure. The sensing textile (glove body, embedded sensors, traces) and the electronics module are treated as separable components so that either can be updated or replaced independently.

5.4.1 Sensor embedding and mechanical stack-up

The embedding strategy preserves the mechanical conditions under which the modules were characterized in Chapters 3 and 4. Palmar pressure modules require the integration stack to transmit normal contact loads without attenuation from stiff encapsulants or interposed textile seams. Dorsal bending modules require sufficient compliance to avoid shifting the joint's neutral axis or introducing parasitic tensile strain. These constraints led to thin, low-modulus encapsulation overcoats, mechanically indexed placement relative to seam lines, and strain-relief features at trace/module transitions.

Pressure sensor array verification. To verify that the row–column readout architecture can isolate individual taxels before full glove integration, a standalone 8×8 capacitive pressure sensor array was fabricated and tested. A single taxel was loaded while the remaining 63 channels were monitored simultaneously. Figure 5.7 shows the resulting spatial response: the pressed taxel (Row 3, Col 3) registers a peak of 12.0 kPa, while the highest response among its neighbours is 1.7 kPa, indicating small crosstalk relative to the on-pixel signal. The baseline capacitance across the unloaded array is approximately 5.20 pF. These results confirm that the array fabrication and readout chain achieve sufficient spatial isolation for palmar contact mapping.

Kirigami interconnect structure. Kirigami was considered as an alternative strain-relief architecture for glove interconnects. Patterned cuts allow extension to be accommodated through cut opening, bridge rotation, and out-of-plane deformation rather than uniform axial strain in the conductor. This mechanism has preserved electrical conductance in patterned nanocomposite sheets over strains far beyond those tolerated by unpatterned sheets [155]. It is therefore attractive for glove wiring, which experiences combined bending, shear, and twisting as the fingers flex and the textile shifts.

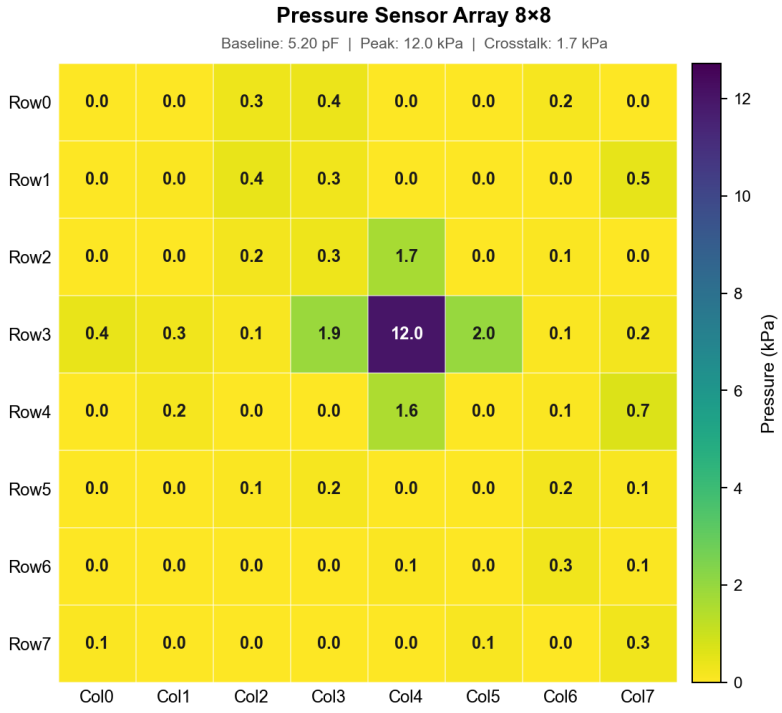


Figure 5.7: Spatial response of the 8×8 capacitive pressure sensor array under single-taxel loading at Row 3, Col 3. The colour map shows the capacitance-derived pressure across all 64 taxels. The pressed pixel reaches 12.0 kPa; the largest neighbouring response is 1.7 kPa (crosstalk). Baseline capacitance: 5.20 pF.

The literature also shows that kirigami geometry alone does not guarantee drift-free resistance. Yamagishi *et al.* demonstrated a copper-coated polyimide kirigami wiring encapsulated in silicone that remained conductive during repeated extension to 150% strain, but its normalized resistance increased over 100 cycles and cracking was observed in the copper layer [156]. By contrast, liquid-metal elastic kirigami electrodes have shown substantially greater strain tolerance and smaller resistance changes, including resistance confined to 18.4–19.2 Ω during 1000 cycles at 0–100% strain and changes below 1.7% during wearable joint motion [157]. These studies support kirigami as a mechanically compliant interconnect strategy while showing that electrical stability depends strongly on the conductor and encapsulation materials. The automated pipeline nevertheless retained serpentine traces because they can be generated directly from spline-based routing rules; incorporating kirigami would require additional unit-cell, slit-spacing, and transition constraints.

5.4.2 Electronics integration, readout, and communication

A wrist-mounted electronics hub aggregates all sensing channels and provides excitation, signal conditioning, and digitization. The hub connects to the sensing textile through a standardized, detachable connector that supports both wired and battery-powered wireless operation. The glove-level data reported in Section 5.5 were acquired in wired mode, providing synchronized multi-channel readout across all bending channels.

5.4.3 System calibration and standardized outputs

Integration inevitably introduces offsets and gains that must be resolved to obtain interpretable outputs. For the current glove prototype, calibration was kept intentionally lightweight: baseline zeroing, channel-connectivity checks, and task-specific reference measurements were performed before data collection. The anatomy-aligned layout of Section 5.3 is designed to reduce the geometric component of calibration: because sensor positions are referenced to anatomical landmarks rather than arbitrary garment coordinates, the placement is intended to remain consistent across wearing sessions, leaving primarily electrical zeroing as the remaining calibration step. The geometric component of this claim is quantified in Section 5.4.4: under a standardised acquisition pose the pipeline reproduces sensor positions to 0.98 mm RMS at the fingertips, against fingertip offsets of 16.1–39.6 mm when a single fixed template is used instead. Whether this geometric consistency translates into reduced electrical recalibration across sessions remains future work. Where appropriate, the final reported quantities can still be expressed in protocol-compatible units such as degrees for joint angles and pressure or force proxies for palmar contact. The primary glove-level evaluation of the assembled prototype — channel behavior during hand motion, signal stability across participants, and gesture-classification performance — is reported in Section 5.5. Those measurements were acquired with wired readout from the integrated glove, with sensors embedded and routed according to the anatomy-to-layout pipeline described in Sections 5.3.1–5.3.6. In this chapter, these results are used as an initial validation of the bending-glove realization rather than as a complete validation of the full multimodal glove system.

Integrated palmar–dorsal measurement. Figure 5.8 presents the reporting layout for test glove measurements, separating seven palmar channels from thirteen dorsal channels and marking the intervals used to compare whole-hand flexion, the unloaded baseline, and selective index-finger contact. The figure establishes the combined-channel presen-

tation used for the integrated glove. Additional repeated measurements across operating conditions are required to characterize signal quality fully.

5.4.4 Validation status of photo-based sensor placement

The photo-based placement method introduced in Section 5.3 has not been subjected to the ideal test of its effectiveness, which would be a controlled comparison between an empirically designed glove and a glove produced by the proposed pipeline, evaluated on the same participants under the same task. That comparison requires two fully fabricated gloves per participant and is beyond the scope of the present work. What can be established here is narrower but well defined: whether the pipeline produces manufacturable layouts across different hand geometries, and how much of the *geometric* mismatch between intended and anatomy-referenced sensor locations it removes relative to a fixed template. This subsection reports that geometric validation and states explicitly what it does and does not demonstrate.

Six participants were photographed under the acquisition protocol of Section 5.3.1 and processed end-to-end into nine-channel palmar layouts. All six layouts routed completely, with every channel connected and all clearance rules satisfied (Table 5.2); the tightest trace-to-trace separation observed across the six was 1.81 mm against a 0.50 mm rule. Although hand length spanned only 10% across the group, the resulting substrate outlines differed by 40% in width, confirming that the layout responds to anatomy rather than merely rescaling. Placement accuracy was then assessed against a fixed template derived from a single reference hand, emulating a conventional one-size design. Under that template the worst-case fingertip offset ranged from 16.1–39.6 mm (mean 29.0 mm), exceeding the 4 mm half-width of the 8×8 mm fingertip electrode for every participant, so that in each case the intended anatomical target fell outside the electrode footprint. The personalized pipeline is not error-free either: its placement reproducibility, measured from repeated acquisitions of the same hand under the standardised pose, was 0.98 mm RMS at the fingertips and 0.21 mm at the palm pads, with a worst-case site-to-site spread of 3.80 mm (Table 5.3). No site exceeded the electrode half-width. The contrast is therefore between a fixed template, for which every participant's worst channel lay outside the electrode footprint, and the personalized pipeline, for which every channel lay inside it (Fig. 5.9). Allowing the fixed template to be uniformly rescaled to each hand — an idealisation more permissive than discrete garment sizing — removed only 16% of the median mismatch, indicating that the residual arises from differences in hand *shape* rather than hand *size* and is therefore not addressable by sizing alone.

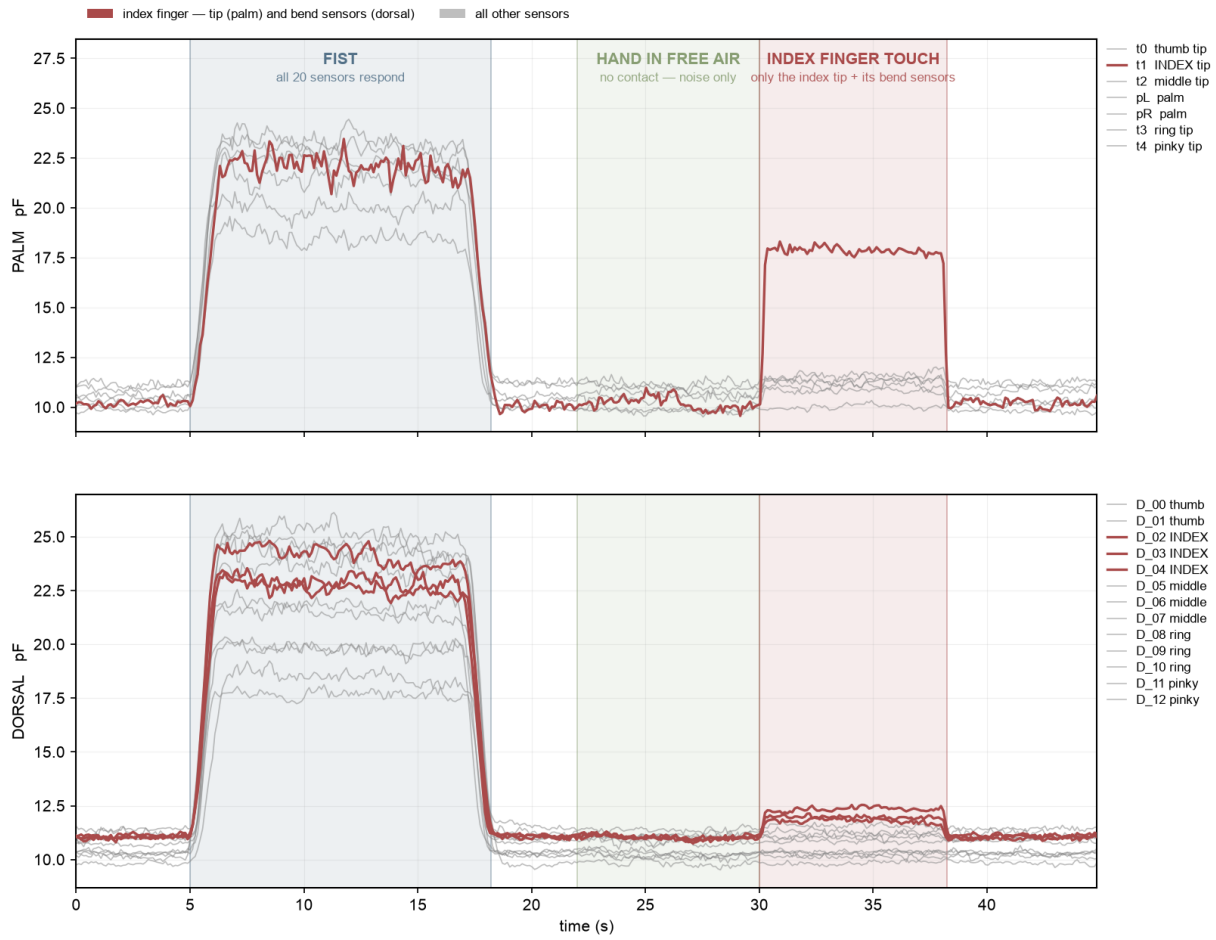


Figure 5.8: Reporting layout for synchronized measurements from the integrated glove. Top: seven palmar channels. Bottom: thirteen dorsal channels. The marked intervals distinguish whole-hand flexion, the unloaded baseline, and selective index-finger contact.

Two conditions limit interpretation of these results. First, placement reproducibility was evaluated only under the standardised acquisition pose; performance under uncontrolled pose variation was not assessed in the present study. Second, the six participants were photographed in a single session using one calibration target. The reported offsets are therefore relative measurements within a shared scale and do not establish the absolute accuracy of the photogrammetric calibration. The geometric validation reported above and the functional validation in Section 5.5 were obtained using two different instantiations of the same pipeline: a nine-channel palmar pressure array and a three-channel dorsal bending glove, respectively. Neither result substitutes for a controlled comparison between an empirically designed glove and a personalized glove. Such a study should fabricate both glove types for each participant, repeat donning between recording blocks, and report cross-validated classification accuracy, per-channel signal-to-noise ratio, and between-session drift.

Table 5.2: Photo-derived layouts for six participants. All nine channels routed for every participant and all clearance rules were satisfied (rule: 0.50 mm). The final column is the worst-case fingertip offset when a single fixed template is used instead of the personalized layout; the fingertip electrode half-width is 4 mm.

Participant	**Hand length** (cm)	**Channels** routed	**Trace–trace** (mm)	**Substrate** W × H (mm)	**Fixed-template** worst tip (mm)
Participant 1	15.52	9/9	1.81	116.1 × 161.6	39.6
Participant 2	16.10	9/9	1.93	130.6 × 164.9	28.3
Participant 3	16.82	9/9	1.85	162.4 × 174.0	16.1
Participant 4	16.73	9/9	1.94	148.5 × 170.4	25.1
Participant 5	15.29	9/9	2.27	128.7 × 162.3	28.3
Participant 6	15.75	9/9	1.92	128.6 × 166.1	36.4
Range	15.29–16.82	6/6	≥ 1.81	116.1–162.4	16.1–39.6

Table 5.3: Placement reproducibility of the photo-based pipeline, from three repeated acquisitions of the same hand under the standardised pose with the hand re-placed between shots. RMS is taken about the mean site position; the worst pairwise column is the largest separation between any two repeats. No site exceeds the 4 mm fingertip electrode half-width.

Sensor site	**RMS (mm)**	**Max deviation (mm)**	**Worst pairwise (mm)**
Thumb tip (t0)	1.80	2.42	3.80
Index tip (t1)	1.17	1.60	2.64
Middle tip (t2)	0.50	0.67	1.19
Ring tip (t3)	0.55	0.65	1.25
Little tip (t4)	0.87	1.14	1.92
Palm pads (pm0–pm3)	0.21	0.29	0.48
Fingertips, mean	0.98	—	3.80 (worst)

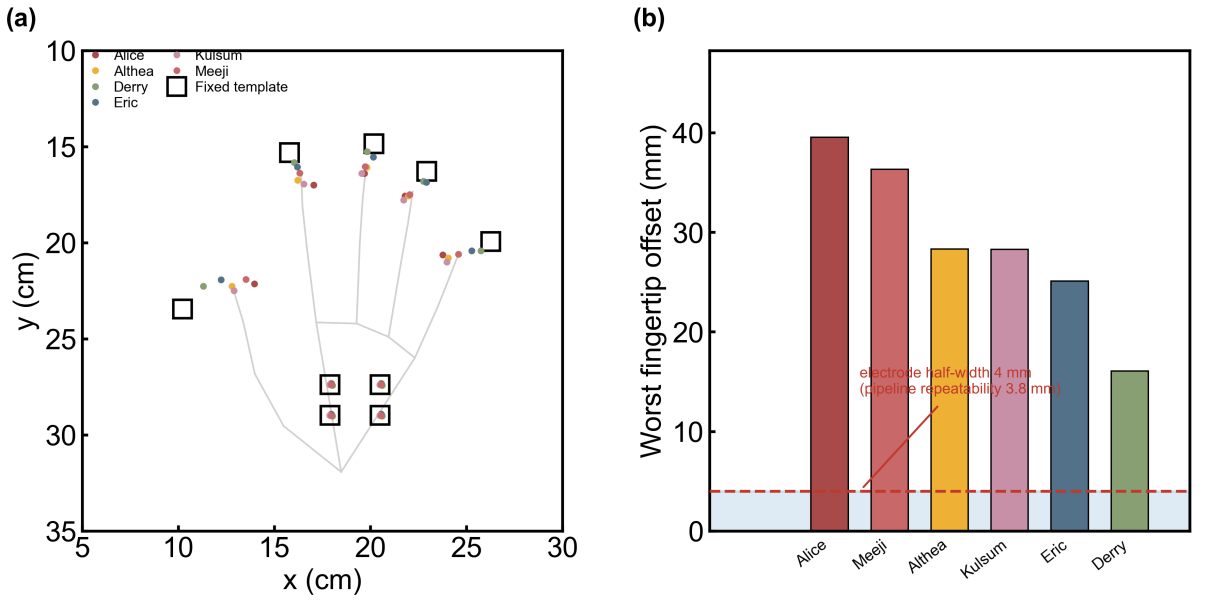


Figure 5.9: Geometric validation of the photo-based placement pipeline. (a) Personalized nine-channel sensor sites for six participants (coloured markers) shown in a common palm-aligned frame against the fixed single-reference template (open squares); the faint outline is the group-mean hand skeleton. Palm pads remain within their template squares, whereas fingertip sites are displaced well outside them. (b) Worst-case fingertip offset per participant under the fixed template. The shaded band marks the 4 mm electrode half-width, within which the pipeline's own placement reproducibility (3.8 mm worst case) also falls; all six participants lie outside it under the fixed template.

5.5 Glove Prototype Validation

5.5.1 Glove configuration and participant study

Bending sensors were embedded into a fabric glove following the placement and routing logic of Section 5.3: modules were positioned on the dorsal finger segments, routed along low-strain interdigital corridors, and connected to the wrist electronics hub via the wired readout described in Section 5.4.2. Sensors were installed using a sliding mounting method: one end of each sensor was fixed to the glove dorsum, while the opposite end was constrained by an elastic band acting as a strain-limiting layer. This mounting scheme reduces sensitivity to tensile strain and encourages the output to depend primarily on bending angle rather than on glove tension or fit variation — consistent with the angle-centric design requirement established in Chapter 4.

Six participants (2 female, 4 male; mean age 27; mean thumb length 6 cm) with different hand sizes donned the same glove without per-user hardware refitting. The study evaluates the integrated prototype and readout scheme. Geometric validation of the personalized-layout workflow, together with the protocol for its controlled comparison, is given in Section 5.4.4.

5.5.2 Machine learning pipeline for gesture classification

ANN, SVM, CNN, and LSTM classifiers were implemented for gesture recognition. The pipeline comprises: (i) signal preprocessing (removing first/last 5% of each recording to improve stability at trial boundaries), (ii) windowing (100 ms windows, 5 samples per window), (iii) feature extraction using five time-domain descriptors — mean absolute value (MAV), root mean square (RMS), waveform length (WL), variance (VAR), and standard deviation (SD) — and (iv) classifier training and evaluation on an 80/20 train–validation split. Classification performance was quantified using accuracy, precision, recall, and F1 score [158]:

$$\begin{aligned} \text{Accuracy} &= \frac{TP+TN}{TP+FP+TN+FN}, & \text{Precision} &= \frac{TP}{TP+FP}, \\ \text{Recall} &= \frac{TP}{TP+FN}, & \text{F1} &= \frac{2\cdot\text{Precision}\cdot\text{Recall}}{\text{Precision}+\text{Recall}}. \end{aligned} \tag{5.1}$$

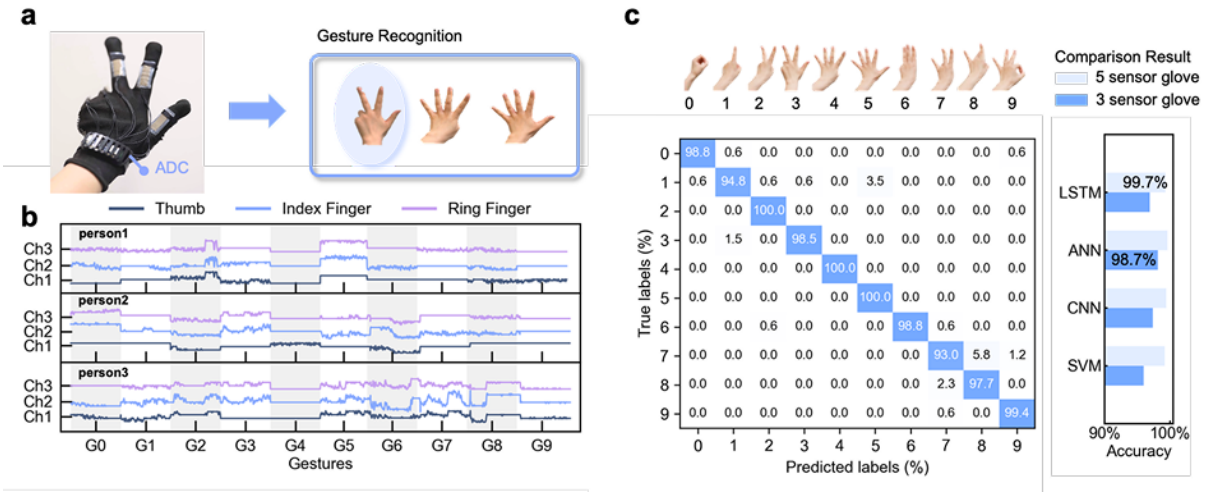


Figure 5.10: Data-glove gesture recognition with the integrated bending-sensor glove. (a) Three-sensor glove during recording. (b) Representative capacitance traces from three channels across repeated gesture trials. (c) Confusion matrix for ten-gesture classification (ANN, three-channel), showing reliable separation across gesture classes.

Table 5.4: Gesture-recognition accuracy for the three-channel and five-channel bending-sensor glove configurations.

Glove configuration	**Best-performing classifier**	**Accuracy**
Three-sensor glove	ANN	98.7%
Five-sensor glove	LSTM	99.7%

5.5.3 Results

Across the 10-gesture dataset, the three-sensor glove achieved 98.7% classification accuracy with an ANN classifier (Table 5.4). The confusion matrix in Fig. 5.10(c) is dominated by the diagonal, indicating reliable separation of ten gestures using only three sensing channels. A five-sensor comparator configuration reached 99.7% with an LSTM model, demonstrating that additional channels can close the remaining error, but the compact three-channel layout already provides strong performance at substantially lower hardware complexity.

The results confirm that the angle-centric transduction mechanism delivers high gesture-classification performance without dense per-finger instrumentation. The comparison with representative data gloves is presented in Section 5.5.4.

Table 5.5: Comparison of the bending-sensor glove against representative gesture-recognition gloves.

Reference	Sensing modality	Gestures	Participants	Channels	Accuracy
[159]	Resistive strain	10	1	10	93.3%
[160]	Capacitive	10	10	5	97.0%
This work	Capacitive	10	6	3	98.7%

5.5.4 Benchmarking against representative data gloves

Table 5.5 compares the bending-sensor glove against representative gesture-recognition gloves from the literature. Prior works based on resistive strain sensors often require more channels to reach comparable accuracy, while the capacitive approach developed here achieves 98.7% with only three channels across six participants with varied hand sizes.

5.6 Summary

The anatomy-to-layout pipeline converts calibrated hand photographs into parametric glove patterns with anatomy-referenced sensor placements. A MANO-based skin-strain analysis justifies the zone assignments—palmar pressure modules in contact-dominant, near-neutral-strain zones; dorsal bending modules in low-surface-strain zones consistent with the angle-centric requirement of Chapter 4; routing corridors along mechanically stable interdigital and dorsal surfaces. A web interface wraps the full pipeline for interactive inspection and CAD export.

At the fabrication level, sensor embedding and a modular wrist-connector architecture were developed and prototyped. A standalone 8×8 pressure sensor array was used to examine row–column readout before full glove integration. Kirigami was evaluated from the literature as a mechanically compliant alternative for joint-crossing interconnects, but the serpentine layout was retained in the automated pipeline because it can be generated directly from spline-based routing rules. Detachable electronics separate the sensing textile from the readout hardware, supporting component-level serviceability.

A six-participant gesture-recognition study demonstrated 98.7 % classification accuracy across ten gestures with three bending-sensor channels and no per-user hardware refitting, confirming that the integrated prototype produces stable signals sufficient for

high-accuracy classification from a compact channel count. The comparison with literature gloves confirms that the angle-centric approach remains competitive with fewer channels than resistive-strain alternatives.

Chapter 6

Conclusions

This thesis treats wearable hand sensing as a system-design problem rather than solely as a sensor-development problem. A useful glove for on-the-go use must coordinate transduction physics, soft mechanics, anatomical placement, calibration, routing, garment fit, and material stability. The pressure and bending sensors developed here are intended to be integrated with these constraints rather than evaluated only as separate device demonstrations.

This perspective also clarifies the boundary of the thesis. The work does not claim to have produced a clinically complete glove platform or to have eliminated calibration and fit problems. Instead, it develops design choices intended to reduce several sources of variability that are otherwise handled through ad hoc calibration. Pressure response is shaped through range-aware microstructure design; bending response is biased toward joint-angle-driven dielectric deformation rather than local surface strain; and glove layout is generated from anatomical measurements rather than fixed-size placement rules.

6.1 What the Thesis Establishes

The work supports three conclusions. First, soft pressure sensors for wearable use benefit from being designed around a target operating range rather than characterized only after fabrication. Treating linearity and sensitivity as design objectives makes the microstructure a tunable element of the sensing system rather than a passive material feature.

Second, the results suggest that reducing placement-dependent artifacts at the sensor-architecture level can reduce the calibration burden before the signal reaches the readout

circuit. A sensor that is sensitive mainly to local skin strain remains vulnerable to donning, fit, and placement variation, even when calibration improves its output. An architecture that makes the dominant capacitance change arise from joint-scale bending is intended to reduce this sensitivity at the device level.

Third, personalization extends beyond sizing to a fabrication workflow. A glove that is nominally stretchable can still place sensors inconsistently across users. The anatomy-to-layout pipeline developed in this thesis reframes personalization as a sequence of measurable transformations: hand landmarks are converted into pattern geometry, sensor zones, routing paths, and manufacturing outputs. This does not by itself prove clinical effectiveness, but it defines the practical pathway by which personalized sensing layouts can be made repeatable.

6.2 Reflective Assessment

Overall, this thesis provides a useful design framework and prototype study, but remains incomplete as a clinically validated glove system. Its central system-level claim remains to be tested: whether a fully personalized glove consistently outperforms an empirically designed or fixed-size glove across users, donning events, and clinical tasks.

The proposed approach is designed to reduce fit, misalignment, and calibration sensitivity by shifting variability into controllable design parameters: microstructure geometry for pressure response, dielectric architecture for bending response, and landmark-based layout for sensor placement. Its effect on full-system repeatability remains to be quantified. Important remaining sources of variability include material aging, hydration state, repeated donning, cable or module motion, inter-user skin mechanics, and task-dependent contact patterns.

With hindsight, an earlier controlled comparison of personalized and generic gloves may have produced stronger translational evidence and a more experimentally complete glove chapter. The broader scope nevertheless developed reusable sensor-level design principles. The trade-off was reduced depth of final full-system validation.

The pressure and bending sensors also have merit beyond the specific glove application. Range-aware pressure microstructures are relevant to other soft robotic skins, wearable interfaces, and compliant contact sensors. The angle-centric bending architecture is relevant to body-joint monitoring wherever placement variability and local skin strain contaminate the measurement. Their strongest role in this thesis, however, is as enabling components for a personalized hand-sensing platform.

6.3 Remaining Open Questions

Long-term material stability is one of the most important remaining open questions. This is especially true for iontronic sensing, where hydration, encapsulation, sweat exposure, humidity, and repeated compression can affect both the material state and the electrical interface. A sensitive sensor that cannot maintain calibration over realistic use conditions is not yet a deployable wearable sensor.

Material stability is not the only unresolved limitation. The personalized placement method still requires a controlled comparison against a non-personalized or empirically designed glove. The pressure and bending sensors still need to be integrated and evaluated together in a multimodal glove. The readout electronics must be miniaturized and made robust to daily movement. Multi-session calibration stability must be measured across repeated donning and doffing. These questions define the next stage of the work more clearly than additional isolated sensor optimization would.

The most important future experiment is therefore not simply to improve one sensor metric. It is to fabricate personalized and non-personalized gloves for the same participants, compare their alignment and calibration stability across repeated wear, and evaluate whether the personalized design improves clinically meaningful hand-motion and contact measurements. That experiment would directly test the central claim of the thesis: that wearable hand sensing improves when sensor design, soft mechanics, and anatomy-aware integration are treated as one design problem.

References

[1] Valery L. Feigin, Benjamin A. Stark, Catherine O. Johnson, et al. Global, regional, and national burden of stroke and its risk factors, 1990–2019: a systematic analysis for the Global Burden of Disease Study 2019. *The Lancet Neurology*, 20(10):795–820, 2021.

[2] Peter Langhorne, Julie Bernhardt, and Gert Kwakkel. Stroke rehabilitation. *The Lancet*, 377(9778):1693–1702, 2011.

[3] Madison Bates and Sridhar Sunderam. Hand-worn devices for assessment and rehabilitation of motor function and their potential use in BCI protocols: A review. *Frontiers in Human Neuroscience*, 17:1121481, July 2023.

[4] Debeshi Dutta, Srinivasan Aruchamy, Soumen Mandal, and Soumen Sen. Poststroke Grasp Ability Assessment Using an Intelligent Data Glove Based on Action Research Arm Test: Development, Algorithms, and Experiments. *IEEE Transactions on Biomedical Engineering*, 69(2):945–954, February 2022.

[5] Francisco R. Avila, Rickey E. Carter, Christopher J. McLeod, Charles J. Bruce, Davide Giardi, Gunel Guliyeva, and Antonio J. Forte. Accuracy of Wearable Sensor Technology in Hand Goniometry: A Systematic Review. *Hand (New York, N.Y.)*, 18(2):340–348, March 2023.

[6] Verónica Gracia-Ibáñez, Margarita Vergara, James H. Buffi, Wendy M. Murray, and Joaquín L. Sancho-Bru. Across-subject calibration of an instrumented glove to measure hand movement for clinical purposes. *Computer Methods in Biomechanics and Biomedical Engineering*, 20(6):587–597, April 2017.

[7] Laura Dipietro, Angelo M. Sabatini, and Paolo Dario. Evaluation of an instrumented glove for hand-movement acquisition. *The Journal of Rehabilitation Research and Development*, 40(2):181, 2003.

[8] Jonathan Howard, Zoe Fisher, Andrew H. Kemp, Stephen Lindsay, Lorna H. Tasker, and Jeremy J. Tree. Exploring the barriers to using assistive technology for individuals with chronic conditions: A meta-synthesis review. *Disability and Rehabilitation: Assistive Technology*, 17(4):390–408, May 2022.

[9] L. N. Gitlin, M. R. Luborsky, and R. L. Schemm. Emerging Concerns of Older Stroke Patients About Assistive Device Use. *The Gerontologist*, 38(2):169–180, April 1998.

[10] Katarzyna Kabacińska, Kim Vu, Mallorie Tam, Olivia Edwards, William C. Miller, and Julie M. Robillard. "Functioning better is doing better": Older adults' priorities for the evaluation of assistive technology. *Assistive Technology*, 35(4):367–373, July 2023.

[11] Aline Darc Piculo Dos Santos, Ana Lya Moya Ferrari, Fausto Orsi Medola, and Frode Eika Sandnes. Aesthetics and the perceived stigma of assistive technology for visual impairment. *Disability and Rehabilitation: Assistive Technology*, 17(2):152–158, February 2022.

[12] Elsa M. Orellano-Colón, Marta Rivero-Méndez, Blanca N. Ralat-Fonseca, Nelson Varas-Díaz, Mauricio Lizama-Troncoso, Ivonne Z. Jiménez-Velázquez, and Jeffrey W. Jutai. Multilevel barriers to using assistive technology devices among older hispanics from poor and disadvantaged communities: The relevance of a gender analysis. *Disability and Rehabilitation: Assistive Technology*, 19(3):682–698, April 2024.

[13] Ochae Kwon, Kihyo Jung, Heecheon You, and Hee-Eun Kim. Determination of key dimensions for a glove sizing system by analyzing the relationships between hand dimensions. *Applied Ergonomics*, 40(4):762–766, July 2009.

[14] Hye Suk Kim, Yujin Hong, and Hee Eun Choi. Corresponding measurement-based patternmaking method for customized gloves to support smart wearables. *Journal of Industrial Textiles*, 53:15280837231188966, September 2023.

[15] Abdelsalam Ahmed, Islam Hassan, and Jean Zu. Design Guidelines of Stretchable Pressure Sensors-Based Triboelectrification. *Advanced Engineering Materials*, 20(8):1700997, 2018. _eprint: https://onlinelibrary.wiley.com/doi/pdf/10.1002/adem.201700997.

[16] Subin Kang, Jaehong Lee, Sanggeun Lee, SeulGee Kim, Jae-Kang Kim, Hassan Algadi, Saleh Al-Sayari, Dae-Eun Kim, DaeEun Kim, and Taeyoon Lee. Highly Sensitive Pressure Sensor Based on Bioinspired Porous Structure for Real-Time Tactile Sensing. *Advanced Electronic Materials*, 2(12):1600356, 2016.

[17] Sara Rachel Arussy Ruth, Levent Beker, Helen Tran, Vivian Rachel Feig, Naoji Matsuhisa, and Zhenan Bao. Rational Design of Capacitive Pressure Sensors Based on Pyramidal Microstructures for Specialized Monitoring of Biosignals. *Advanced Functional Materials*, 30(29):1903100, 2020.

[18] Sara Rachel Arussy Ruth and Zhenan Bao. Designing Tunable Capacitive Pressure Sensors Based on Material Properties and Microstructure Geometry. *ACS applied materials & interfaces*, 12(52):58301–58316, December 2020.

[19] Wei Zhang, Weihao Sun, Wenling Xiao, Xuyan Zhong, Chengwei Wu, and Weihong Guo. Numerical Simulation Analysis of Microstructure of Dielectric Layers in Capacitive Pressure Sensors. *IEEE Sensors Journal*, 19(9):3260–3266, 2019.

[20] Chao Ma, Gang Li, Longhui Qin, Weicheng Huang, Hongrui Zhang, Wenfeng Liu, Tianyu Dong, and Sheng-Tao Li. Analytical Model of Micropyramidal Capacitive Pressure Sensors and Machine-Learning-Assisted Design. *Advanced Materials Technologies*, 6(12):2100634, 2021.

[21] Jianing Wu, Yagang Yao, Yuhan Zhang, Tianyu Shao, Hao Wu, Shaoyu Liu, Zhuo Li, and Limin Wu. Rational design of flexible capacitive sensors with highly linear response over a broad pressure sensing range. *Nanoscale*, 12(41):21198–21206, 2020.

[22] Bing Ji, Qian Zhou, Ming Lei, Sen Ding, Qi Song, Yibo Gao, Shunbo Li, Yi Xu, Yinning Zhou, and Bingpu Zhou. Gradient architecture-enabled capacitive tactile sensor with high sensitivity and ultrabroad linearity range. *Small*, 17(43):e2103312, 2021.

[23] Sara Rachel Arussy Ruth, Vivian Rachel Feig, Helen Tran, and Zhenan Bao. Microengineering Pressure Sensor Active Layers for Improved Performance. *Advanced Functional Materials*, 30(39):2003491, September 2020.

[24] Xin Li, Qisheng Yang, Zetian Zhao, Mingyuan Li, Yuhan Zhao, Jiarong Fan, Qi Mao, Xudong Fang, Daixuan Wu, Jingbo Liu, Hao Guo, and He Tian. Bibliometric review on flexible pressure sensor design strategies. *Nanoscale*, 17(25):14999–15028, 2025.

[25] Stefan C. B. Mannsfeld, Benjamin C.-K. Tee, Randall M. Stoltenberg, Christopher V. H.-H. Chen, Soumendra Barman, Beinn V. O. Muir, Anatoliy N. Sokolov, Colin Reese, and Zhenan Bao. Highly sensitive flexible pressure sensors with microstructured rubber dielectric layers. *Nature Materials*, 9(10):859–864, October 2010.

[26] Tian Hua, Ziyin Xiang, Xiangling Xia, Zhangling Li, Dandan Sun, Yuanzhao Wu, Yiwei Liu, Jie Shang, Jun Chen, and Runwei Li. A sensitivity-optimized flexible capacitive pressure sensor with cylindrical ladder microstructural dielectric layers. *Sensors*, 23(9):4323, April 2023.

[27] Alba Roda-Sales, Joaquín L. Sancho-Bru, and Margarita Vergara. Problems Using Data Gloves with Strain Gauges to Measure Distal Interphalangeal Joints' Kinematics. *Sensors*, 22(10):3757, January 2022.

[28] Zhaoyang Li, Bo Zhang, Kun Li, Tong Zhang, and Xiaoniu Yang. A wide linearity range and high sensitivity flexible pressure sensor with hierarchical microstructures via laser marking. *Journal of Materials Chemistry C*, 8(9):3088–3096, 2020.

[29] Yaoguang Shi, Xiaozhou Lu, Jihao Zhao, Wenran Wang, Xiangyu Meng, Pengfei Wang, and Fan Li. Flexible capacitive pressure sensor based on microstructured composite dielectric layer for broad linear range pressure sensing applications. *Micromachines*, 13(2):223, 2022.

[30] Zhong Shen, Juan Yi, Xiaodong Li, Mark Hin Pei Lo, Michael Z. Q. Chen, Yong Hu, and Zheng Wang. A soft stretchable bending sensor and data glove applications. *Robotics and Biomimetics*, 3(1):22, December 2016.

[31] Myungsun Park, Taejun Park, Soah Park, Sohee John Yoon, Sumin Helen Koo, and Yong-Lae Park. Stretchable glove for accurate and robust hand pose reconstruction based on comprehensive motion data. *Nature Communications*, 15(1):5821, July 2024.

[32] James Connolly, Joan Condell, Kevin Curran, and Philip Gardiner. Improving Data Glove Accuracy and Usability Using a Neural Network When Measuring Finger Joint Range of Motion. *Sensors*, 22(6):2228, 2022.

[33] Margarita Vergara, María Jesús Agost, and Vicente Bayarri. Anthropometric characterisation of palm and finger shapes to complement current glove-sizing systems. *International Journal of Industrial Ergonomics*, 74:102836, 2019.

[34] Yan Huang, Xiangyu Fan, Shih-Chi Chen, and Ni Zhao. Emerging technologies of flexible pressure sensors: materials, modeling, devices, and manufacturing. *Advanced functional materials*, 29(12):1808509, 2019.

[35] Yanru Li, Dawei Jiang, Yulong An, Wenshuai Chen, Zhanhua Huang, and Bo Jiang. Wearable flexible pressure sensors: an intriguing design towards microstructural functionalization. *Journal of Materials Chemistry A*, 12(12):6826–6874, 2024.

[36] Hao Yuan, Qiran Zhang, Tong Zhou, Wenbo Wu, Haoran Li, Zhuopeng Yin, Jinming Ma, and Tifeng Jiao. Progress and challenges in flexible capacitive pressure sensors: Microstructure designs and applications. *Chemical Engineering Journal*, 485:149926, April 2024.

[37] Guojun Tai, Dapeng Wei, Min Su, Pei Li, Lei Xie, and Jun Yang. Force-sensitive interface engineering in flexible pressure sensors: A review. *Sensors*, 22(7):2652, March 2022.

[38] Jonas Hilário, Haihang Wang, Peng Wang, Wei Yu, and Chuizhou Meng. Modeling and simulation of microstructure geometry and material type on flexible capacitive pressure sensors by finite element analysis. *IEEE Sensors Journal*, 25(3):4811–4819, February 2025.

[39] Huangping Yan, Zijun Wang, Rui Zhou, Jingbo Yin, Yuanzhe Li, and Yuchao Zhu. Distribution optimization of micro-cone structures in the dielectric layer of a capacitive flexible pressure sensor. *Measurement*, 201:111773, September 2022.

[40] Zhenjin Xu, Dezhi Wu, Zhiwen Chen, Zhongbao Wang, Cong Cao, Xiangyu Shao, Gang Zhou, Shaohua Zhang, Lingyun Wang, and Daoheng Sun. A flexible pressure sensor with highly customizable sensitivity and linearity via positive design of microhierarchical structures with a hyperelastic model. *Microsystems & Nanoengineering*, 9(1):5, January 2023.

[41] Hüsnü Dal, Kemal Açıkgöz, and Yashar Badienia. On the performance of isotropic hyperelastic constitutive models for rubber-like materials: A state of the art review. *Applied Mechanics Reviews*, 73(2), March 2021.

[42] Yuhai Xiang, Danming Zhong, Peng Wang, Guoyong Mao, Honghui Yu, and Shaoxing Qu. A general constitutive model of soft elastomers. *Journal of the Mechanics and Physics of Solids*, 117:110–122, August 2018.

[43] Yuhai Xiang, Danming Zhong, Peng Wang, Tenghao Yin, Haofei Zhou, Honghui Yu, Chinmay Baliga, Shaoxing Qu, and Wei Yang. A physically based visco-hyperelastic constitutive model for soft materials. *Journal of the Mechanics and Physics of Solids*, 128:208–218, July 2019.

[44] L. Angela Mihai and Alain Goriely. How to characterize a nonlinear elastic material? a review on nonlinear constitutive parameters in isotropic finite elasticity. *Proceedings of the Royal Society A: Mathematical, Physical and Engineering Sciences*, 473(2207):20170607, November 2017.

[45] Ehsan Haghighat, Maziar Raissi, Adrian Moure, Hector Gomez, and Ruben Juanes. A physics-informed deep learning framework for inversion and surrogate modeling in solid mechanics. *Computer Methods in Applied Mechanics and Engineering*, 379:113741, June 2021.

[46] Beichen Li, Bolei Deng, Wan Shou, Tae-Hyun Oh, Yuanming Hu, Yiyue Luo, Liang Shi, and Wojciech Matusik. Computational discovery of microstructured composites with optimal stiffness-toughness trade-offs. *Science Advances*, 10(5):eadk4284, February 2024.

[47] Jakub Kudela and Radomil Matousek. Recent advances and applications of surrogate models for finite element method computations: a review. *Soft Computing*, 2022.

[48] Bowen Lei, Tanner Quinn Kirk, Anirban Bhattacharya, Debdeep Pati, Xiaoning Qian, Raymundo Arroyave, Dane Morgan, and Bani K. Mallick. Bayesian optimization with adaptive surrogate models for automated experimental design. *npj Computational Materials*, 7(1):194, December 2021.

[49] Yulin Guo, Paromita Nath, Sankaran Mahadevan, and Paul Witherell. Active learning for adaptive surrogate model improvement in high-dimensional problems. *Structural and Multidisciplinary Optimization*, 67:122, July 2024.

[50] Srija Vennam, Vijayasankar KN, and Falguni Pati. 3d printed personalized assistive devices: A material, technique, and medical condition perspective. *Applied Materials Today*, 40:102403, October 2024.

[51] Yan Wang, Qitao Tan, Fang Pu, David Boone, and Ming Zhang. A review of the application of additive manufacturing in prosthetic and orthotic clinics from a biomechanical perspective. *Engineering*, 6(11):1258–1266, November 2020.

[52] Rui Silva, Bruna Silva, Cristiana Fernandes, Pedro Morouço, Nuno Alves, and António Veloso. A review on 3d scanners studies for producing customized orthoses. *Sensors*, 24(5):1373, February 2024.

[53] M. Keller, A. Guebeli, Florian Thieringer, and Philipp Honigmann. In-hospital professional production of patient-specific 3d-printed devices for hand and wrist rehabilitation. *Hand Surgery and Rehabilitation*, 40(2):126–133, April 2021.

[54] Amr Osman and Jian Lu. 3d printing of polymer composites to fabricate wearable sensors: A comprehensive review. *Materials Science and Engineering: R: Reports*, 154:100734, July 2023.

[55] Luis Paredes, Sai Swarup Reddy, Subramanian Chidambaram, Devashri Vagholkar, Yunbo Zhang, Bedrich Benes, and Karthik Ramani. Fabhandwear: An end-to-end pipeline from design to fabrication of customized functional hand wearables. *Proceedings of the ACM on Interactive, Mobile, Wearable and Ubiquitous Technologies*, 5(2):1–22, June 2021.

[56] Devin Murphy, Yichen Li, Crystal Elaine Owens, Layla Stanton, Paul Pu Liang, Yiyue Luo, Antonio Torralba, and Wojciech Matusik. Fits like a flex-glove: Automatic design of personalized fpcb-based tactile sensing gloves. In *Proceedings of the Extended Abstracts of the CHI Conference on Human Factors in Computing Systems*, CHI EA '25, page 1–8. ACM, April 2025.

[57] Chiara Micheli. *Design, Development, and Validation of a Soft Electronic Skin Based on Piezoelectric Polymers*. PhD thesis, Università degli Studi di Genova, 2025.

[58] Florence Elizabeth Godkin. *Advancing the Measurement and Use of Daily Life Heart Rate Using Wearable Technology: Applications to Parkinson's Disease*. PhD thesis, University of Waterloo, 2026.

[59] Chengyang Qian. *Soft Wearable Sensors for Continuous Cardiovascular Diseases Monitoring*. PhD thesis, University of California, Irvine, 2024.

[60] Yu Chang, Liu Wang, Ruya Li, Zhichao Zhang, Qi Wang, Junlong Yang, Chuan Fei Guo, and Tingrui Pan. First Decade of Interfacial Iontronic Sensing: From Droplet Sensors to Artificial Skins. *Advanced Materials*, 33(7):2003464, 2021.

[61] Sung-Geun Choi, Se-Hun Kang, Ju-Yong Lee, Joo-Hyeon Park, and Seung-Kyun Kang. Recent advances in wearable iontronic sensors for healthcare applications. *Frontiers in Bioengineering and Biotechnology*, 11, December 2023.

[62] Omar Faruk Emon, Hao Sun, Ahadur Rahim, and Jae-Won Choi. An Ionic Liquid-Based Stretchable Sensor for Measuring Normal and Shear Force. *Soft Robotics*, May 2023.

[63] Junli Shi, Sai Xie, Zhiguang Liu, Minkun Cai, and Chuan Fei Guo. Non-hygroscopic ionogel-based humidity-insensitive iontronic sensor arrays for intra-articular pressure sensing. *National Science Review*, 11(11):nwae351, October 2024.

[64] Caicong Li, Jianxiang Cheng, Yunfeng He, Xiangnan He, Ziyi Xu, Qi Ge, and Canhui Yang. Polyelectrolyte elastomer-based ionotronic sensors with multi-mode sensing capabilities via multi-material 3d printing. *Nature Communications*, 14:4853, 2023.

[65] Ningning Bai, Liu Wang, Qi Wang, Jue Deng, Yan Wang, Peng Lu, Jun Huang, Gang Li, Yuan Zhang, Junlong Yang, Kewei Xie, Xuanhe Zhao, and Chuan Fei Guo. Graded intrafillable architecture-based iontronic pressure sensor with ultra-broad-range high sensitivity. *Nature Communications*, 11(1):209, January 2020.

[66] Yuxiang Qin, Xueshuo Zhang, Anbo Zheng, and Qing Xia. Bioinspired design of hill-ridge architecture-based iontronic sensor with high sensibility and piecewise linearity. *Advanced Materials Technologies*, 7(1):2100510, 2022.

[67] Shengping Yao, Junhao Shen, Yixin Guo, Shaohua Zuo, Fuwen Shi, Jinchun Jiang, and Junhao Chu. Poly(vinyl alcohol)/phosphoric acid gel electrolyte@polydimethylsiloxane sponge for piezoresistive pressure sensors. *Journal of Materials Chemistry B*, 9(41):8676–8685, 2021.

[68] Ruoxi Yang, Ankan Dutta, Bowen Li, Naveen Tiwari, Wanqing Zhang, Zhenyuan Niu, Yuyan Gao, Daniel Erdely, Xin Xin, Tiejun Li, and Huanyu Cheng. Iontronic pressure sensor with high sensitivity over ultra-broad linear range enabled by laser-induced gradient micro-pyramids. *Nature Communications*, 14(1):2907, June 2023.

[69] Shuyun Zhuo, Cheng Song, Qinfeng Rong, Tianyi Zhao, and Mingjie Liu. Shape and stiffness memory ionogels with programmable pressure-resistance response. *Nature Communications*, 13:1743, 2022.

[70] Cuiping Liu, Jinfan Qi, Bingbing He, Huan Zhang, Jie Ju, and Xi Yao. Ionic conductive gels based on deep eutectic solvents. *International Journal of Smart and Nano Materials*, 12(3):337–350, 2021.

[71] Joachim Nitsche. Über ein Variationsprinzip zur Lösung von Dirichlet-Problemen bei Verwendung von Teilräumen, die keinen Randbedingungen unterworfen sind. *Abhandlungen aus dem Mathematischen Seminar der Universität Hamburg*, 36(1):9–15, 1971.

[72] Jørgen S. Dokken and Sarah Roggendorf. dolfinx_contact: custom contact mechanics library for dolfinx, 2023.

[73] J. F. Salmeron, F. Molina-Lopez, A. Rivadeneyra, A. F. Vasquez Quintero, L. F. Capitan-Vallvey, N. F. de Rooij, J. B. Ozaez, D. Briand, and A. J. Palma. Design and development of sensing RFID tags on flexible foil compatible with EPC Gen 2. *IEEE Sensors Journal*, 14(12):4361–4371, 2014.

[74] Timo Salpavaara, Jarmo Verho, Pekka Kumpulainen, and Jukka Lekkala. Readout methods for an inductively coupled resonance sensor used in pressure garment application. *Sensors and Actuators A: Physical*, 172(1):109–116, 2011.

[75] Ariel Slepyan and Nitish V. Thakor. Towards scalable soft e-skin: Flexible event-based tactile-sensors using wireless sensor elements embedded in soft elastomer. In *2020 8th IEEE RAS/EMBS International Conference for Biomedical Robotics and Biomechatronics (BioRob)*, pages 334–339, 2020.

[76] Md Abu Saleh Tajin, Chelsea E. Amanatides, Genevieve Dion, and Kapil R. Dandekar. Passive UHF RFID-based knitted wearable compression sensor. *IEEE Internet of Things Journal*, 8(17):13763–13773, 2021.

[77] Junli Shi, Yuan Dai, Yu Cheng, Sai Xie, Gang Li, Yuan Liu, Jingxiao Wang, Ruirui Zhang, Ningning Bai, Minkun Cai, Yuan Zhang, Yifei Zhan, Zhengyou Zhang, Cunjiang Yu, and Chuan Fei Guo. Embedment of sensing elements for robust, highly sensitive, and cross-talk–free iontronic skins for robotics applications. *Science Advances*, 9(9):eadf8831, March 2023.

[78] Haicheng Yao, Weidong Yang, Wen Cheng, Yu Jun Tan, Hian Hian See, Si Li, Hashina Parveen Anwar Ali, Brian Z. H. Lim, Zhuangjian Liu, and Benjamin C. K. Tee. Near–hysteresis-free soft tactile electronic skins for wearables and reliable machine learning. *Proceedings of the National Academy of Sciences*, 117(41):25352–25359, October 2020.

[79] Shu Wan, Peng Wan, Shen Li, Junju Wang, Haizhou Huang, Ji Jin, Shunbo Li, Xuefeng He, Shi Su, Hengchang Bi, and Yizhou Ye. A Highly Sensitive Iontronic Pressure Sensor for High-Pressure Range Monitoring. *IEEE Sensors Journal*, 25(7):10766–10774, April 2025.

[80] Yang Gao, Guohui Yu, Jianping Tan, and Fuzhen Xuan. Sandpaper-molded wearable pressure sensor for electronic skins. *Sensors and Actuators A: Physical*, 280:205–209, September 2018.

[81] Tao Jin, Zhongda Sun, Long Li, Quan Zhang, Minglu Zhu, Zixuan Zhang, Guangjie Yuan, Tao Chen, Yingzhong Tian, Xuyan Hou, and Chengkuo Lee. Triboelectric nanogenerator sensors for soft robotics aiming at digital twin applications. *Nature Communications*, 11(1):5381, October 2020.

[82] Cheng Xie, Jia Li, and Weibing Wang. A package for piezoresistive pressure sensors with embedded built-in self-test function based on bimetallic actuator. *Sensors and Actuators A: Physical*, 346:113817, October 2022.

[83] Bijender and Ashok Kumar. Recent progress in the fabrication and applications of flexible capacitive and resistive pressure sensors. *Sensors and Actuators A: Physical*, 344:113770, September 2022.

[84] Pu Nie, Ranran Wang, Xiaojuan Xu, Yin Cheng, Xiao Wang, Liangjing Shi, and Jing Sun. High-Performance Piezoresistive Electronic Skin with Bionic Hierarchical Microstructure and Microcracks. *ACS Applied Materials & Interfaces*, 9(17):14911–14919, May 2017.

[85] Yihao Li, Junyu Long, Yun Chen, Yan Huang, and Ni Zhao. Crosstalk-Free, High-Resolution Pressure Sensor Arrays Enabled by High-Throughput Laser Manufacturing. *Advanced Materials*, 34(21):2200517, May 2022.

[86] Zhibin Li, Jing Yang, Yuxuan Zhang, Peiyan Geng, Jiansong Feng, Bin Chen, Xu Zhang, Guojiang Yuan, Xiaolong Chen, and Taihong Wang. Ultrafast readout, crosstalk suppression iontronic array enabled by frequency-coding architecture. *npj Flexible Electronics*, 8(1):1–12, February 2024.

[87] D. A. van den Ende, W. A. Groen, and S. van der Zwaag. Development of temperature stable charge based piezoelectric composite quasi-static pressure sensors. *Sensors and Actuators A: Physical*, 163(1):25–31, 2010.

[88] Xiaoyang Li and Edwin C. Kan. A wireless low-range pressure sensor based on P(VDF-TrFE) piezoelectric resonance. *Sensors and Actuators A: Physical*, 163(2):457–463, 2010.

[89] R. Otmani, N. Benmoussa, and B. Benyoucef. The thermal drift characteristics of piezoresistive pressure sensor. *Physics Procedia*, 21:47–52, 2011.

[90] Franz Konstantin Fuss, Adin Ming Tan, and Yehuda Weizman. 'Electrical Viscosity' of piezoresistive sensors: Novel signal processing method, assessment of manufacturing quality, and proposal of an industrial standard. *Biosensors and Bioelectronics*, 141:111408, 2019.

[91] A. Hanneborg and P. Ohlckers. A capacitive silicon pressure sensor with low TCO and high long-term stability. *Sensors and Actuators A: Physical*, 21:151–154, 1990.

[92] Jun Chang Yang, Jin-Oh Kim, Jinwon Oh, Se Young Kwon, Joo Yong Sim, Da Won Kim, Han Byul Choi, and Steve Park. Microstructured porous pyramid-based ultrahigh sensitive pressure sensor insensitive to strain and temperature. *ACS Applied Materials & Interfaces*, 11(21):19472–19480, 2019.

[93] Jing Li, Rongrong Bao, Juan Tao, Yiyao Peng, and Caofeng Pan. Recent progress in flexible pressure sensor arrays: From design to applications. *Journal of Materials Chemistry C*, 6(44):11878–11892, November 2018.

[94] J. W. Nicholas, R. J. Corvese, C. Woolley, and T. J. Armstrong. Quantification of hand grasp force using a pressure mapping system. *Work*, 41(Suppl. 1):605–612, 2012.

[95] Xin Li, Jiajie Guo, Xingxing Ma, Luye Yang, Kok-Meng Lee, and Caihua Xiong. Flexible Capacitive Curvature Sensor with One-Time Calibration for Amphibious Gait Monitoring. *Soft Robotics*, 8(2):164–174, April 2021.

[96] Y. Zhang, M. Shafiei, J. Z. Wen, Z. Abbasi, and C. L. Ren. Simultaneous detection of pressure and bending using a microwave sensor with tag and reader structure. *IEEE Transactions on Instrumentation and Measurement*, 72:1–11, 2023.

[97] Ali Asghar Shamabadi, Morteza Rezaee, and Amin Kazemi-Beydokhti. Microwave pressure sensor based on transmission response of a quarter-wavelength single stub microstrip line. *Microwave and Optical Technology Letters*, 62(9):2821–2825, 2020.

[98] Amr Ibrahim and DRS Cumming. Passive single chip wireless microwave pressure sensor. *Sensors and Actuators A: Physical*, 165(2):200–206, 2011.

[99] Masoud Baghelani, Zahra Abbasi, and Mojgan Daneshmand. High-dynamic-range chipless microwave resonator-based strain sensor. *IEEE Transactions on Instrumentation and Measurement*, 70:1–7, 2021.

[100] Mehdi Nosrati, Zahra Abbasi, Masoud Baghelani, Sharmistha Bhadra, and Mojgan Daneshmand. Locally strong-coupled microwave resonator using pemc boundary for distant sensing applications. *IEEE Transactions on Microwave Theory and Techniques*, 67(10):4130–4139, 2019.

[101] Zahra Abbasi, Masoud Baghelani, Mehdi Nosrati, Amir Sanati-Nezhad, and Mojgan Daneshmand. Real-time non-contact integrated chipless rf sensor for disposable microfluidic applications. *IEEE Journal of Electromagnetics, RF and Microwaves in Medicine and Biology*, 4(3):171–178, 2019.

[102] Mehdi Nosrati and Mojgan Daneshmand. Substrate integrated waveguide l-shaped iris for realization of transmission zero and evanescent-mode pole. *IEEE Transactions on Microwave Theory and Techniques*, 65(7):2310–2320, 2017.

[103] Andrea Rinaldi, Alessio Tamburrano, Marco Fortunato, and Maria Sabrina Sarto. A flexible and highly sensitive pressure sensor based on a pdms foam coated with graphene nanoplatelets. *Sensors*, 16(12):2148, 2016.

[104] ID Johnston, DK McCluskey, CKL Tan, and MC Tracey. Mechanical characterization of bulk sylgard 184 for microfluidics and microengineering. *Journal of Micromechanics and Microengineering*, 24(3):035017, 2014.

[105] WS Lee, KS Yeo, A Andriyana, YG Shee, and FR Mahamd Adikan. Effect of cyclic compression and curing agent concentration on the stabilization of mechanical properties of pdms elastomer. *Materials & Design*, 96:470–475, 2016.

[106] Md Rajibur Rahaman Khan, Tae Kyu An, and Hwa Sung Lee. A battery-free, chipless, highly sensitive lc pressure sensor tag using pedot: Pss and melamine foam. *IEEE Sensors Journal*, 21(2):2184–2193, 2020.

[107] Longquan Ma, Xuecheng Yu, Yuanyuan Yang, Yougen Hu, Xinyu Zhang, Huayuan Li, Xing Ouyang, Pengli Zhu, Rong Sun, and Ching-Ping Wong. Highly sensitive flexible capacitive pressure sensor with a broad linear response range and finite element analysis of micro-array electrode. *Journal of Materiomics*, 6(2):321–329, 2020.

[108] Chenkai Jiang and Bin Sheng. Linear capacitive pressure sensor with gradient architecture through laser ablation on MWCNT/Ecoflex film. *Polymers*, 16(7):962, 2024.

[109] Yanxu Chen, Yuxiang Qin, Xueshuo Zhang, Anbo Zheng, and Qing Xia. Hierarchical Arete Architecture-Enabled Iontronic Pressure Sensor with High Linearity and Sensitivity. *Advanced Materials Technologies*, 7(11):2200322, 2022.

[110] Nora Asyikin Zulkifli, Geon Dae Moon, Dong Choon Hyun, and Sungwon Lee. Comprehensive constitutive modeling and analysis of multi-elastic polydimethylsiloxane

(PDMS) for wearable device simulations. *Scientific Reports*, 13(1):18413, October 2023.

[111] Nick Cheney, Josh Bongard, Vytas SunSpiral, and Hod Lipson. Scalable co-optimization of morphology and control in embodied machines. *Journal of The Royal Society Interface*, 15(143):20170937, June 2018.

[112] Gabriel Bravo-Palacios, Gianluigi Grandesso, Andrea Del Prete, and Patrick M. Wensing. Robust co-design: Coupling morphology and feedback design through stochastic programming. *Journal of Dynamic Systems, Measurement, and Control*, 144(2), November 2021.

[113] Heng Yang, Li Yuan, Xue Feng Yao, and Dai Ning Fang. Piezoresistive response of graphene rubber composites considering the tunneling effect. *Journal of the Mechanics and Physics of Solids*, 139:103943, 2020.

[114] Mojtaba Haghgoo, Alireza Alidoust, Reza Ansari, and Mohammad Kazem Hassanzadeh-Aghdam. Percolation mechanism of the graphene nanoplatelets/elastomeric flexible sensing nanocomposite under an applied compressive strain. *Sensors and Actuators A: Physical*, 362:114677, 2023.

[115] Qinwu Gao, Hui Li, Jinjie Zhang, Zhenwen Xie, Jinyong Zhang, and Lei Wang. Microchannel structural design for a room-temperature liquid metal based super-stretchable sensor. *Scientific Reports*, 9:5908, 2019.

[116] Md Saifur Rahman, Julia E. Huddy, Andrew B. Hamlin, and William J. Scheideler. Broadband mechanoresponsive liquid metal sensors. *npj Flexible Electronics*, 6:71, 2022.

[117] Yousef Bahramzadeh and Mohsen Shahinpoor. Dynamic curvature sensing employing ionic-polymer–metal composite sensors. *Smart Materials and Structures*, 20(9):094011, September 2011.

[118] Liting Chen, Bingying Zheng, Jinhua Ye, and Haibin Wu. Cone-shaped electrodes for capacitive tactile sensors with high sensitivity and broad linearity range. *Advanced Materials Technologies*, 8:2300901, 2023.

[119] Jaeyong Lee, Soonjae Pyo, Dae-Sung Kwon, Eunhwan Jo, Wondo Kim, and Jongbaeg Kim. Ultrasensitive Strain Sensor Based on Separation of Overlapped Carbon Nanotubes. *Small*, 15(12):1805120, 2019.

[120] Ninja P. Oess, Johann Wanek, and Hubertus J. A. van Hedel. Enhancement of bend sensor properties as applied in a glove for use in neurorehabilitation settings. In *2010 Annual International Conference of the IEEE Engineering in Medicine and Biology*, pages 5903–5906, August 2010.

[121] Takehiro Goto, Toshiki Ishikawa, Takashi Komuro, and Kenji Suzuki. Bending Angle Sensor Based on Double-Layer Capacitance Suitable for Human Joint. *Scientific Reports*, 13:128, January 2023.

[122] Carl Demolder, Alicia Molina, Frank L. Hammond, and Woon-Hong Yeo. Recent advances in wearable biosensing gloves and sensory feedback biosystems for enhancing rehabilitation, prostheses, healthcare, and virtual reality. *Biosensors and Bioelectronics*, 190:113443, October 2021.

[123] Christopher B. Cooper, Kuralamudhan Arutselvan, Ying Liu, Daniel Armstrong, Yiliang Lin, Mohammad Rashed Khan, Jan Genzer, and Michael D. Dickey. Stretchable Capacitive Sensors of Torsion, Strain, and Touch Using Double Helix Liquid Metal Fibers. *Advanced Functional Materials*, 27(20):1605630, 2017.

[124] Xian Song, Akram Samy, Qiang Yang, Yangqiu Yang, Liang Zhong, Jianxiang Wang, Zijian Zheng, and Yuxin Peng. Omnidirectional and Size-Adaptive Soft Bending Sensor for Accurate Human Joint Motion Monitoring. *IEEE Transactions on Industrial Electronics*, 71(7):8069–8079, July 2024.

[125] Panagiotis Polygerinos, Zheng Wang, Kevin C. Galloway, Robert J. Wood, and Conor J. Walsh. Soft robotic glove for combined assistance and at-home rehabilitation. *Robotics and Autonomous Systems*, 73:135–143, November 2015.

[126] Chia-Ye Chu and Rita M. Patterson. Soft robotic devices for hand rehabilitation and assistance: A narrative review. *Journal of NeuroEngineering and Rehabilitation*, 15(1):9, February 2018.

[127] Tobias Bützer, Olivier Lambercy, Jumpei Arata, and Roger Gassert. Fully Wearable Actuated Soft Exoskeleton for Grasping Assistance in Everyday Activities. *Soft Robotics*, 8(2):128–143, April 2021.

[128] Cem Suulker, Alexander Greenway, Sophie Skach, Ildar Farkhatdinov, Stuart Charles Miller, and Kaspar Althoefer. Let Me Give You a Hand: Enhancing Human Grasp Force With a Soft Robotic Assistive Glove. *IEEE Robotics and Automation Letters*, 9(9):7811–7818, 2024.

[129] Lisa K. Simone and Derek G. Kamper. Design considerations for a wearable monitor to measure finger posture. *Journal of NeuroEngineering and Rehabilitation*, 2(1):5, March 2005.

[130] James H. Buffi, Joaquín Luis Sancho Bru, Joseph J. Crisco, and Wendy M. Murray. Evaluation of hand motion capture protocol using static computed tomography images: Application to an instrumented glove. *Journal of Biomechanical Engineering*, 136(12):124501, December 2014.

[131] Mingzhang Pan, Yingzhe Tang, and Hongqi Li. State-of-the-Art in Data Gloves: A Review of Hardware, Algorithms, and Applications. *IEEE Transactions on Instrumentation and Measurement*, 72:1–15, 2023.

[132] Jieming Pan, Yuxuan Luo, Yida Li, Chen-Khong Tham, Chun-Huat Heng, and Aaron Voon-Yew Thean. A Wireless Multi-Channel Capacitive Sensor System for Efficient Glove-Based Gesture Recognition With AI at the Edge. *IEEE Transactions on Circuits and Systems II: Express Briefs*, 67(9):1624–1628, September 2020.

[133] Shengshun Duan, Yucheng Lin, Qiongfeng Shi, Xiao Wei, Di Zhu, Jianlong Hong, Shengxin Xiang, Wei Yuan, Guozhen Shen, and Jun Wu. Highly Sensitive and Mechanically Stable MXene Textile Sensors for Adaptive Smart Data Glove Embedded with Near-Sensor Edge Intelligence. *Advanced Fiber Materials*, 6(5):1541–1553, October 2024.

[134] Talha Agcayazi, Kony Chatterjee, Alper Bozkurt, and Tushar K. Ghosh. Flexible Interconnects for Electronic Textiles. *Advanced Materials Technologies*, 3(10):1700277, October 2018.

[135] Jeffrey Henderson, Joan Condell, James Connolly, Daniel Kelly, and Kevin Curran. Review of Wearable Sensor-Based Health Monitoring Glove Devices for Rheumatoid Arthritis. *Sensors*, 21(5):1576, January 2021.

[136] Reinhard Gentner and Joseph Classen. Development and evaluation of a low-cost sensor glove for assessment of human finger movements in neurophysiological settings. *Journal of Neuroscience Methods*, 178(1):138–147, March 2009.

[137] Nicholas Hale, Maria Valero, Jinghua Tang, David Moser, and Liudi Jiang. A preliminary study on characterisation of finger interface kinetics using a pressure and shear sensor system. *Prosthetics and Orthotics International*, 42(1):60–65, February 2018.

[138] Ümit Uğurlu and Huri Özdoğan. Development of normative data for cylindrical grasp pressure. *International Journal of Industrial Ergonomics*, 41(5):509–519, September 2011.

[139] Jeffrey B. Nelson and Anil Mital. An ergonomic evaluation of dexterity and tactility with increase in examination/surgical glove thickness. *Ergonomics*, 38(4):723–733, 1995.

[140] Carolyn K. Bensel. The effects of various thicknesses of chemical protective gloves on manual dexterity. *Ergonomics*, 36(6):687–696, June 1993.

[141] Camille E. Proulx, Johanne Higgins, Thomas Vaughan, Mark Hewko, and Dany H. Gagnon. Poststroke neurorehabilitation using a soft robotic glove combined with a virtual environment: Preliminary study on feasibility, safety, effects, and user satisfaction. *JMIR Neurotechnology*, 4:e69750, 2025.

[142] Salman Shafqat, Johan P. M. Hoefnagels, Angel Savov, Shivani Joshi, Ronald Dekker, and Marc G. D. Geers. Ultra-stretchable interconnects for high-density stretchable electronics. *Micromachines*, 8(9):277, September 2017.

[143] Camillo Lugaresi, Jiuqiang Tang, Hadon Nash, Chris McClanahan, Esha Uboweja, Michael Hays, Fan Zhang, Chuo-Ling MacGlashan, Thiago Beker, Jared Cooley, et al. Mediapipe: A framework for building perception pipelines. In *CVPR Workshops*, 2019.

[144] Annie Yu, Kit-Lun Yick, Sau-Po Ng, and Joanna Yip. 2d and 3d anatomical analyses of hand dimensions for custom-made gloves. *Applied Ergonomics*, 44(3):381–392, May 2013.

[145] Iso 7250-1:2017 basic human body measurements for technological design — part 1: Body measurement definitions and landmarks. International Organization for Standardization, 2017.

[146] R. Hamilton and R. A. Dunsmuir. Radiographic assessment of the relative lengths of the bones of the fingers of the human hand. *Journal of Hand Surgery: British and European Volume*, 27(6):546–548, December 2002.

[147] Christina Salchow-Hömmen, Leonie Callies, Daniel Laidig, Markus Valtin, Thomas Schauer, and Thomas Seel. A tangible solution for hand motion tracking in clinical applications. *Sensors*, 19(1):208, January 2019.

[148] Annie Yu, Kit-Lun Yick, and Sin-Tung Wong. Analysis of length of finger segments with different hand postures to enhance glove design. *Applied Ergonomics*, 94:103409, July 2021.

[149] Soo-Min Lee and Juyeon Park. Ergonomic glove pattern drafting method for hand assistive devices: Considering 3d hand dimensions and finger mobility. *Fashion and Textiles*, 11:31, September 2024.

[150] Javier Romero, Dimitrios Tzionas, and Michael J. Black. Embodied hands: Modeling and capturing hands and bodies together. *ACM Transactions on Graphics*, 36(6):1–17, 2017.

[151] Dong Hyun Kim, Sang Wook Lee, and Hyung-Soon Park. Improving kinematic accuracy of soft wearable data gloves by optimizing sensor locations. *Sensors*, 16(6):766, May 2016.

[152] IPC. IPC-2223E: Sectional design standard for flexible/rigid-flexible printed boards. Technical report, IPC International, Inc., 2020.

[153] Yung-Yu Hsu, Mario Gonzalez, Frederick Bossuyt, Fabrice Axisa, Jan Vanfleteren, and Ingrid De Wolf. The effects of encapsulation on deformation behavior and failure mechanisms of stretchable interconnects. *Thin Solid Films*, 519(7):2225–2234, January 2011.

[154] XiuFeng Wang, JieLong Huang, YangChengYi Liu, JinYuan Tan, ShangDa Chen, Raudel Avila, and ZhaoQian Xie. Design of protective and high sensitivity encapsulation layers in wearable devices. *Science China Technological Sciences*, 66(1):223–232, 2023.

[155] Terry C. Shyu, Pablo F. Damasceno, Paul M. Dodd, Aaron Lamoureux, Lizhi Xu, Matthew Shlian, Max Shtein, Sharon C. Glotzer, and Nicholas A. Kotov. A kirigami approach to engineering elasticity in nanocomposites through patterned defects. *Nature Materials*, 14(8):785–789, August 2015.

[156] Kento Yamagishi, Takenori Nakanishi, Sho Mihara, Masaru Azuma, Shinji Takeoka, Kazuyuki Kanosue, Tomoyuki Nagami, and Toshinori Fujie. Elastic kirigami patch for electromyographic analysis of the palm muscle during baseball pitching. *NPG Asia Materials*, 11(1):1–13, December 2019.

[157] Hyesu Choi, Yichi Luo, Gina Olson, Phillip Won, Joo Hwan Shin, Jehyung Ok, Ye Ji Yang, Tae-il Kim, and Carmel Majidi. Highly Stretchable and Strain-Insensitive

Liquid Metal based Elastic Kirigami Electrodes (LM-eKE). *Advanced Functional Materials*, 33(30):2301388, 2023.

[158] Y. Dong, J. Liu, and W. Yan. Dynamic hand gesture recognition based on signals from specialized data glove and deep learning algorithms. *IEEE Transactions on Instrumentation and Measurement*, 70:1–14, 2021.

[159] Yangyang Zhang, Ying Huang, Xuehu Sun, Yunong Zhao, Xiaohui Guo, Ping Liu, Caixia Liu, and Yugang Zhang. Static and Dynamic Human Arm/Hand Gesture Capturing and Recognition via Multiinformation Fusion of Flexible Strain Sensors. *IEEE Sensors Journal*, 20(12):6450–6459, June 2020.

[160] W. K. Wong, F. H. Juwono, and B. T. T. Khoo. Multi-features capacitive hand gesture recognition sensor: A machine learning approach. *IEEE Sensors Journal*, 21:8441–8450, 2021.